Aspects of Computational Homogenization at Finite Deformations: A Unifying Review From Reuss' to Voigt's Bound

Saba Saeb
Chair of Applied Mechanics
University of Erlangen–Nuremberg,
Egerland Str. 5,
Erlangen 91058, Germany
e-mail: saba.saeb@ltm.uni-erlangen.de

Paul Steinmann
Chair of Applied Mechanics
University of Erlangen–Nuremberg,
Egerland Str. 5,
Erlangen 91058, Germany
e-mail: paul.steinmann@ltm.uni-erlangen.de

Ali Javili[1]
Department of Mechanical Engineering,
Bilkent University,
Ankara 06800, Turkey
e-mail: ajavili@bilkent.edu.tr

The objective of this contribution is to present a unifying review on strain-driven computational homogenization at finite strains, thereby elaborating on computational aspects of the finite element method. The underlying assumption of computational homogenization is separation of length scales, and hence, computing the material response at the macroscopic scale from averaging the microscopic behavior. In doing so, the energetic equivalence between the two scales, the Hill–Mandel condition, is guaranteed via imposing proper boundary conditions such as linear displacement, periodic displacement and antiperiodic traction, and constant traction boundary conditions. Focus is given on the finite element implementation of these boundary conditions and their influence on the overall response of the material. Computational frameworks for all canonical boundary conditions are briefly formulated in order to demonstrate similarities and differences among the various boundary conditions. Furthermore, we detail on the computational aspects of the classical Reuss' and Voigt's bounds and their extensions to finite strains. A concise and clear formulation for computing the macroscopic tangent necessary for FE^2 calculations is presented. The performances of the proposed schemes are illustrated via a series of two- and three-dimensional numerical examples. The numerical examples provide enough details to serve as benchmarks. [DOI: 10.1115/1.4034024]

Keywords: computational homogenization, finite strains, random composite, FE^2, multiscale

Dedicated to the memory of Professor Christian Miehe, 1956–2016

1 Introduction

Almost all materials possess heterogeneous structures at a certain scale of observation. Such heterogeneities may be desirable, for instance, in applications of magnetorheological elastomers in artificial muscles. Understanding the behavior of such media is not an easy task as their physical properties depend entirely on their underlying microstructures which may differ in morphology, volume fraction, and properties of the constituents from one to another composite. The complexity of the microstructural behavior is further pronounced by incorporating the interaction between the constituents, debonding along interfaces or damage caused by fracture of the constituents or matrix. Therefore, the prediction of the responses of composite materials requires appropriate and generally sophisticated methods.

Conducting experiments on a large number of material samples with different physical and geometrical properties is nearly impossible from time and cost point of views. Also, performing a direct numerical simulation of the entire body including all the heterogeneities leads to a huge problem whose solution is computationally expensive and demands high memory storage requirements. To overcome this problem, several multiscale techniques have been developed during the past decades. These models are based on the physics of the microstructures and are able to effectively and efficiently predict the macroscopic behavior of heterogeneous materials. Multiscale models are traditionally categorized into the *homogenization method*, where the length scales of micro- and macroproblems are sufficiently separate, and the *concurrent method*, see, e.g., Refs. [1–20], which considers strong coupling between the scales.[2] This contribution details on the former one. In passing, we mention that one of the very popular tools for modeling multiphase materials is asymptotic homogenization. This approach is based on asymptotic expansions of strain and stress fields around their corresponding macroscopic values and utilizing variational principles leading to a set of boundary value problems at the micro- and the macroscale. An extensive body of literature is devoted to study this technique among which we refer to Refs. [23–41]. Reviews of the different multiscale approaches can be found in Refs. [42–44]. The main objective of the homogenization method is to estimate the effective macroscopic properties of a heterogeneous material from the response of its underlying microstructure, thereby allowing to substitute the heterogeneous material with an equivalent homogeneous one. Although most of the ongoing researches in homogenization methods are limited to the spatial homogenization, different temporal scales might also exist in different processes such as chemical reactions. Homogenization in both space and time has been treated in Refs. [45–51].

The first part of this contribution provides a literature review of analytical, semi-analytical, and computational homogenization. Clearly, any attempt to provide a comprehensive review with this scope is a challenging task and a matter of interest to a certain extent. We believe that the following structure forms a continuous and rigorous composition.

1.1 Historical Review of Analytical and Semi-Analytical Homogenization.

Preliminary steps in homogenization date back to the 19th century when Voigt [52] proposed to assume uniform strain within the heterogeneous material. This assumption was later followed by Reuss [53] in a somewhat opposite manner.

[1]Corresponding author.

Manuscript received December 3, 2015; final manuscript received June 23, 2016; published online September 6, 2016. Assoc. Editor: Martin Schanz.

[2]In this contribution, we consider a continuum description of the composite and its microstructure and exclude the atomistic level. However, the classification of multiscale methods given here is commonly accepted in atomistic community too [21,22].

Reuss approximated the stress field within the aggregate of polycrystalline material as uniform. These two approximations, when applied to multiphase composites in pure mechanical problems, yield two bounds for the elastic strain energy [54]. The Voigt's assumption, as the upper bound, violates the equilibrium of the stress field. Also, the Reuss' assumption, as the lower bound, violates the compatibility of the strain field. The bounds are typically quite wide [55] and are justified only for linear material properties. The nonlinear equivalents to Voigt's and Reuss' assumptions are usually referred to as Taylor's and Sachs' bounds [56, 57], respectively, originally derived for polycrystals [58]. While universal and very simple, these bounds do not carry any information of the microstructural morphology and take only the inhomogeneity volume fraction into account. Even though several authors, e.g., Leffers [59], Van Houtte [60], Kocks and Chandra [61], and Van Houtte et al. [62], suggested weakening modifications of these assumptions, they typically provide very rough estimates of the overall material properties and are not reliable for complex nonlinear structures.

Some decades later, Hashin and Shtrikman presented an extension of the method, based on variational formulations, to obtain bounds on bulk and shear moduli [63] and magnetic permeability [64] for isotropic composites consisting of isotropic constituents. Their proposed bounds were later generalized by Walpole [65], Milton and Kohn [66] for anisotropic media, and by Zimmerman [67] to obtain bounds on the Poisson's ratio of the composites. Further improvements were achieved by using three point bounds in the works of Beran and Molyneux [68], Milton and Phan-Thien [69], and Torquato [70]. Employing the same approach, Rosen and Hashin [71]; Gibiansky and Torquato [72] derived bounds for the thermal expansion coefficient in thermoelastic problems and Bisegna and Luciano [73,74]; Hori and Nemat-Nasser [75] obtained bounds for the effective piezoelectric moduli in piezoelectric problems. Note that Hashin–Shtrikman bounds and their improvements yield very wide bounds for the case of considerable mismatch in phase properties [76]. The generalization of the Hashin–Shtrikman variational approach to predict tighter bounds compared to the Voigt's and Reuss' bounds was made in Refs. [77–79] mainly by incorporating the geometrical information of the phases.

A more sophisticated method was established by Eshelby [80] based on *dilute family methods* assuming that the inhomogeneities are so dilutely distributed that their interactions might be neglected. So, the problem is reformed into the analysis of a single inclusion embedded in an infinite matrix [42]. Eshelby's conjecture on validity of his proposed method for only ellipsoidal inclusions has been addressed in Refs. [81–88]. However, neglecting the interaction of particles is an unrealistic assumption of Eshelby for materials with randomly dispersed particulate microstructure, even at a few percent volume fraction [89]. Further proposed models such as Mori–Tanaka [90–92], the self-consistent scheme [93–98], the generalized self-consistent scheme [99–103], and the differential method [104,105] are mainly based on the mean-field approximation [106] and approximate the interaction between the phases. The extension of these models to account for the electroelastic behavior of composite materials was addressed by Dunn and Taya [107]. Further contributions to the self-consistent scheme were made by Nemat-Nasser et al. [108] for periodic porous composites, Herve and Zaoui [109] for multilayered spherical inhomogeneities, and by Huang and Hu [110] for aligned elliptical heterogeneities in two-dimensional problems. Recently, Benveniste and Milton [111,112] made a comprehensive comparison on various derivatives of self-consistent and generalized self-consistent schemes in the context of dielectric two-phase composites and elasticity. In particular, their results indicated that both schemes may violate the Hashin–Shtrikman bounds under certain circumstances, see also Ref. [113] for an overview of self-consistent methods. Also, comparison of Mori–Tanaka estimate and generalized version of Hashin–Shtrikman bounds [65,114] can be found in Ref. [115]. Riccardi and Montheillet [116] compared Mori–Tanaka estimate and the generalized self-consistent scheme and showed that the generalized self-consistent method predicts a stronger dependence on the inclusion aspect ratio. Based on the works introduced in Refs. [100] and [117], Halpin [118] and Halpin and Kardos [119] proposed the Halpin–Tsai equations for the mechanical behavior of continuous aligned fiber composites. Hori and Nemat-Nasser [120] proposed the double-inclusion model which is a unified generalization of the self-consistent and Mori–Tanaka schemes and takes the interaction between the phases into account more appropriately. This model has been developed and studied further in Refs. [121] and [122]. See Ref. [123] for an evaluation of accuracy of various analytical models to predict the stiffness of aligned short-fiber composites.

The extension of the application of the analytical homogenization to nonlinear composites and finite deformation elasticity was studied in the pioneering works of Hill [124] and Ogden [125]. Improved bounds for nonlinear composites were obtained by Willis [126] for nonlinear dielectrics, Ponte Castañeda and Willis [127] for two-phase random composites made of nonlinearly viscous phases, Suquet [128] for power-law composites, Olson [129] for perfectly plastic composites, and Talbot and Willis [130] for general classes of nonlinear composites. A significant development took place with the derivation of a nonlinear variational principle by Ponte Castañeda et al. [131–135] to estimate the effective property of nonlinear incompressible and compressible composites, and in particular, composites made of a ductile and a brittle phase, based on the corresponding linear properties with the same microstructural distribution of phases. Later, exact second-order estimates were established by Ponte Castañeda [136]. Lahellec et al. [137] employed and developed this method to estimate the behavior of hyperelastic periodic composites and compared their results with the experimental and numerical data. Leroy and Ponte Castañeda [138], however, demonstrated that such a methodology may violate Hashin–Shtrikman bounds in some special cases. In order to resolve this shortcoming, Ponte Castañeda [139,140] proposed an improvement of the method which was further extended in Refs. [141] and [142]. Later, deBotton and Hariton [143] and deBotton [144] obtained a general expression for the behavior of incompressible sequentially laminated composites in small deformation and finite elasticity and compared their results with Hashin–Shtrikman bounds and proposed estimates of Ponte Castañeda [136]. In passing, we mention that an important application of homogenization is to predict the behavior of fiber-reinforced materials reported in Refs. [145–148] and references therein.

Analytical methods for modeling reinforced composite materials considering imperfect interface conditions have been developed recently [149–163]. Also, the importance of the interphase zone in modeling composite materials has been discussed in Refs. [164–176], among many. Detailed reviews and comparisons of analytical models of micromechanics can be found in Ref. [177–196]. In particular, see the review by Mura et al. [182].

1.2 Computational Homogenization. In the past two decades, substantial progress has been made in the computational homogenization of complex multiphase materials. Detailed reviews on computational homogenization can be found in Refs. [197] and [198]. One of the widely used approaches in modeling heterogeneous materials is the unit-cell method which leads to a global macroscopic constitutive model for a heterogeneous material based on detailed modeling of the microstructure [199–203]. As a generalization to unit-cell method, direct micro–macro methods have been introduced. These methods evaluate the stress–strain relationship at each point of the macroscale through solving the boundary value problem associated with the microscale. In the literature, the microscale sample is referred to as representative volume element (RVE) for geometrically irregular microstructures and to unit-cell for regular ones. The boundary conditions of the microproblem are defined such that the energy equivalence

between the two scales, known as Hill–Mandel condition [124,204], is preserved. Extension of this formulation to account for inertia and body forces is considered in Refs. [51] and [205–210]. The transition between the two scales is obtained via averaging the internal fields within the RVE. Yue and E [211] discussed alternative averaging methods and reported that weighted or truncated averaging introduced in Refs. [212] and [213] can improve the solution in some cases. Based on Saint-Venant's principle, Wongsto and Li [214] proposed to obtain the effective properties of unidirectional fiber-reinforced composites by only considering the regions sufficiently far from the boundary so as to avoid boundary condition effects.

1.2.1 Choice of the Boundary Condition. The Hill–Mandel condition is satisfied for a variety of boundary conditions among which (i) linear displacement boundary conditions, (ii) periodic displacement and antiperiodic traction boundary conditions, and (iii) constant traction boundary conditions are more common. The first and the last boundary conditions are sometimes referred to as homogeneous boundary conditions. Many authors, e.g., Refs. [215–224], have shown that in pure mechanical linear and nonlinear problems, the effective behavior derived under periodic boundary conditions is bounded by linear displacement boundary conditions from above and constant traction boundary conditions from below for a finite size of the RVE. Kaczmarczyk et al. [225] made similar conclusions in the context of second-order computational homogenization. However, this does not imply that the results obtained under periodic boundary conditions are always the closest ones to the exact solutions as clearly stated by Terada et al. [221] "there is no guarantee that periodic boundary conditions are the best among a class of possible boundary conditions. Nonetheless, the periodic boundary conditions provide the reasonable estimates on the effective moduli in the sense that they are always bounded by the other." Also, it has been claimed in Ref. [226] that "periodic boundary conditions require the continuity of the inclusions on opposite boundaries to ensure the periodicity of the microstructure. Because such unnatural periodicity is seldom observed in real heterogeneous materials, periodic boundary conditions are not appropriate for finite element models developed by cutting out fragments of actual microstructures or by using simulated microstructures based on actual microstructures." Furthermore, Drago and Pindera [227] observed that for the effective value of transverse Poisson's ratio ν_{23}, the estimation based on periodic boundary conditions is not necessarily bounded between the results obtained from linear displacement boundary conditions and constant traction boundary conditions. Recently, inspired by the classical Irving–Kirkwood procedure, Mercer et al. [228] derived a wider set of admissible boundary conditions for the RVE that fill the gap between the homogeneous boundary conditions.

Pecullan et al. [229] investigated the behavior of periodic unidirectional linear composites with different inclusion to matrix stiffness ratio under different boundary conditions. They demonstrated that linear displacement boundary conditions produce a stiffness tensor closer to the effective stiffness tensor for materials with stiff matrix and compliant inclusions. In contrast, constant traction boundary conditions yield better estimates for composites with compliant matrix and stiff inclusions. Similar studies were conducted by Jiang et al. [230], Ostoja-Starzewski [231], Larsson and Runesson [232], and Saroukhani et al. [233]. Pecullan et al. [229] also concluded that the effective bulk moduli obtained under linear DBCs for very high matrix to inclusion stiffness contrast ratio may not satisfy the Hashin–Shtrikman upper bound. Xia et al. [234] reported that the homogeneous boundary conditions, when applied on periodic microstructures, "are not only overconstrained, but may also violate the boundary traction periodicity conditions" under loading types with shear components. Hazanov and Huet [235], Hazanov and Amieur [236], and Pahr and Zysset [237] proposed uniform mixed-type boundary conditions that consider applying constant traction boundary conditions on some parts of the boundary and linear displacement boundary conditions to the other parts such that the apparent elasticity tensor for this boundary condition lies between the apparent tensors obtained with homogeneous boundary conditions. Mesarovic and Padbidri [238] argued that there is no reason to assume that an RVE with random microstructure behaves as a periodic unit cell and suggested the use of *minimal kinematic* boundary conditions. However, minimal kinematic boundary conditions are sensitive to spurious localization in regions close to the RVE boundary [239]. A comprehensive comparison of this type of boundary conditions and periodic boundary conditions was made by Inglis et al. [240]. Recently, Larsson et al. [241] presented a novel variational formulation based on the weak enforcement of periodic boundary conditions. Their proposed idea resolves the restriction of having a periodic RVE mesh to implement periodic boundary conditions, see also Ref. [242]. Glüge [243] introduced a generalized framework of the classical boundary conditions based on partitioning of the boundary of the RVE so that the stiffness of the RVE can be adjusted. Aspects of the numerical solution and computational cost associated with different types of boundary conditions are investigated by Fritzen and Böhlke [244].

1.2.2 The Size and Morphology of the RVE. The choice of the RVE for heterogeneous materials with complex microstructures is a delicate task. Ideally, one would like to reach the maximum accuracy with the least computational effort. The RVE must be large enough to be statistically representative of the composite so that it effectively includes a sampling of all microstructural heterogeneities that occur in the composite [245]. On the other hand, it must remain sufficiently small to be considered as a volume element of continuum mechanics [223]. The first-order computational homogenization scheme critically relies on the principle of separation of scales, which requires that "the microscopic length scale is assumed to be much smaller than the characteristic length over which the macroscopic loading varies in space" [197]. This assumption is particularly valid when macrogradients remain small and material failure does not occur. The second-order computational homogenization partly alleviates the assumption of scale separation by taking the gradient of the macrodeformation gradient tensor into account [246–250]. Furthermore, second-order computational homogenization introduces a physical length to the microscale that is missing in the first-order homogenization. It is also possible to formulate a first-order computational homogenization accounting for size effects by taking surface energies at the microscale into account [251,252].[3] This is justified by the fact that due to the large surface-to-volume ratio at smaller scales, surface contributions to the overall response of the material are no longer negligible at the microscale. This approach shows an excellent agreement with atomistic simulations [255]; see also Ref. [256] where the size effect is introduced in the context of the first-order computational homogenization for transient heat conduction problems.

Strictly speaking, the response of the material must be independent of the choice of boundary conditions imposed on the RVE [257,258]. According to Hill [259], an RVE is well defined when it contains a sufficient number of inclusions and the responses under linear displacement and constant traction boundary conditions coincide. The effective properties obtained from volume elements smaller than the true RVE are referred to as *apparent* properties [260]. Hill's definition on the RVE has been the basis of the work of Ostoja-Starzewski [231] to determine the size of the RVE. He discussed that the size of the RVE is heavily dependent on the type of the problem, and in particular, matrix-to-inclusion stiffness ratio. Temizer and Zohdi [261] carried out similar study and reported that depending on the mesh resolution of the finite element discretization of the microsample, different sizes of the RVE may be obtained. Jiang et al. [230] studied elastic antiplane responses of unidirectional fiber-matrix composites focusing on the effects of the scale of observation and boundary conditions on the overall elastic moduli. They demonstrated that

[3]The link between second-gradient continua and first-order continua with surface energies is interpretable in the seminal work of Mindlin [253], see also Ref. [254].

the results obtained under displacement and traction boundary conditions are more sensitive to the window size compared to those obtained under periodic boundary conditions. Their results were in accordance with the ones reported by El Houdaigui et al. [262] for the case of isotropic polycrystalline copper. Jiang et al. [230] concluded that a relatively small size of the RVE is sufficient to estimate the effective moduli under periodic boundary conditions for a wide range of inclusion to matrix stiffness ratios. A new statistical definition for the RVE based on the mean constitutive response was given by Drugan and Willis [245]. They observed that the minimum size of the RVE is unexpectedly quite small and approximately 4.5 reinforcement diameters to limit the maximum error in the effective modulus estimates to 1% for a variety of matrix and reinforcement materials within the elastic regime. They also found that the apparent property obtained by performing ensemble averaging of stress and strain on a finite microstructure converges very quickly to those achieved from an infinite length. Their findings were numerically verified by Gusev [263]. Gusev studied the overall elastic constant of three-dimensional microstructures subject to periodic boundary conditions based on the finite element method and Monte Carlo simulations and found out that only a few dozen spheres in the unit cell are sufficient to obtain a small scatter in the apparent property. Shan and Gokhale [264] utilized probability density functions of critical microstructural variables such as nearest neighbor distances and also microstress distribution to derive a sufficiently small RVE for a ceramic matrix composite possessing fiber-rich and fiber-poor regions. Kanit et al. [223] proposed a quantitative definition for the RVE through statistical and numerical approaches in the case of linear elasticity and thermal conductivity. Based on their studies, the size of the RVE is a function of five parameters: the physical property, the contrast of properties, the volume fractions of components, the relative precision for the estimation of the effective property, and the number of realizations of the microstructure. Their proposed methodology was evaluated by Dirrenberger et al. [265] to study the size of the RVE for a pathological model of random structures. Harper et al. [266] determined the critical size of the RVE for discontinuous fiber composites with increasing fiber length and volume fraction. They evaluated a number of microsamples and confirmed that it is computationally more efficient to study fewer large microsamples rather than many small ones. Jafari et al. [267] proposed the use of *repeating representative volume element* (RRVE) which could be understood as an RVE in which the particles along the boundaries are periodically distributed. They employed similar criteria as described in Ref. [266] to determine the size of the RRVE for piezoelectric nanocomposites. The influence of the number of realizations of the microstructure on the obtained RVE size has been also studied by Temizer and Zohdi [261]. They showed that microsamples containing more inclusions typically require a smaller number of realization. A comparison between two different approaches, namely, ensemble averaging of multiple realizations and enlarging the size of a single microstructure, to determine the size of the RVE was given in Ref. [268]. They reported that these two methods generally yield equivalent results. Trias et al. [269] reviewed various criteria such as the typical interfiber distance distributions to determine the minimum size for a statistical RVE. While they noted that it strongly depends on the application of interest, they reported the minimum size of the statistical RVE to be 50 fiber radius for carbon fiber-reinforced epoxy. Gitman et al. [270] carried out statistical studies on the existence of an RVE in different regimes of the material behavior such as linear elasticity, hardening, and softening. They showed that the material loses the representative properties in the softening regime and no RVE can be found. In addition, they introduced a new combined numerical-statistical method to determine the size of the RVE. They made use of their proposed approach to study the effect of volume fraction and material periodicity on the size of the RVE. Böhm and Han [271] reported that when inelastic behavior of constituents is considered, larger sizes of the RVE are required compared to the estimates given in the literature for elastic composites. A similar conclusion was made by Pelissou et al. [272] for quasi-brittle composites. The size of the RVE for nonlinear composites containing elastic rigid heterogeneities embedded in an elastoplastic or elastoviscoplastic matrix has been studied recently by Hoang et al. [273]. Stroeven et al. [274] quantified the size of the RVE for nonlinear heterogeneous microstructures by performing statistical analysis based on specific factors such as particle size, applied peak load, dissipated energy, and strain concentration. They clarified that each of these criteria leads to a different size for the RVE [275]. Khisaeva and Ostoja-Starzewski [276], similar to Ref. [231], estimated the size of the RVE by performing quantitative investigation on the convergence trend of the material properties to the effective values with increasing size of the microstructure for nonlinear elastic random composites at finite strains. They demonstrated that the RVE size changes depending on the maximum stretch ratio, the deformation mode, and the mismatch properties of constituents. They also made a brief comparison on the methodology they utilized and the statistical approaches, for instance, the one introduced in Ref. [263], and concluded that the size of the RVE obtained based on the statistical approach generally underestimates the one obtained under their approach. Temizer et al. [277] proposed the use of window method to investigate the convergence behavior of different boundary conditions with increasing the size of the RVE in the case of linear thermal conduction. They demonstrated that, given a sufficiently thick embedding frame, the convergence of different boundary conditions to the effective value exhibits a much faster trend compared to the case that boundary conditions are directly applied to the external boundary of the microsample. Salmi et al. [278] reported that using nonsquare or noncubic microstructures that contain no heterogeneity crossing the boundary leads to a significantly improved rate of convergence of boundary conditions in linear matrix-inclusion random composites. The comparison of spherical and cubical RVE with different boundary conditions in Ref. [279] concludes that the smaller surface-to-volume ratio associated with a spherical RVE yields less influence of the boundary resulting in a better convergence to the effective material behavior as the size of the RVE increases, see also Ref. [280]. The size of the RVE has been also examined in the context of the granular media by Meier et al. [281] where the discrete element method is used to evaluate the size of the RVE. Balzani et al. [282] and Scheunemann et al. [283] proposed the construction of a *statistically similar representative volume element* (SSRVE) to reduce the size and accordingly the computational effort associated with a large complex RVE. They compared the stress–strain curves obtained with their proposed SSRVE including three inclusions with the one obtained from a very large RVE and showed a good agreement of the results along with a significant reduction of computation time of the problem. Methods for determination of the *statistically equivalent representative volume element* have also been discussed by Swaminathan and Ghosh for fiber-reinforced composites for two cases of with and without damage [284,285]. Similarly, Zeman and Šejnoha [286] employed two-point probability functions and second-order intensity functions to characterize the RVE of a graphite–epoxy composite in terms of a periodic unit-cell which possesses similar statistical properties. Furthermore, the minimum size of the RVE for polycrystals has been studied in Refs. [287] and [288]. Recently, Moussaddy et al. [289] argued the validity of existing well-known methodologies to determine the critical size of the RVE for the case of composites reinforced by randomly oriented fibers and presented a new scheme based on statistical variations of average property.

The effects of the shape of heterogeneities and their spatial distribution on the macroscopic response of composite materials have been extensively addressed in the literature through analytical and numerical methods [290–314]. Numerical studies to analyze the effect of shape, distribution, and volume fraction of particles in a metal-matrix composite were performed by Brockenbrough et al. [315]. They reported that the distribution pattern

of the particles has stronger effect on the overall response compared to their shapes. Moreover, the influence of the inclusion arrangement becomes more significant as the inclusion volume fraction increases. Kouznetsova et al. [316] discussed the influence of the randomness of the microstructure on the macroscopic behavior for a constant volume fraction of voids. Their results show that a microstructure with random distribution of the voids leads to more compliant behavior compared to a microstructure with periodically distributed voids for elastic materials. These results shall be compared with the results obtained by Wongsto and Li [214] who carried out numerical analyses of unidirectionally fiber-reinforced composites for both random and regular packed fibers in the context of linear elasticity. Trias et al. [317] provided a detailed comparison on random and periodic models for fiber-reinforced composites and reported that the periodic models could lead to underestimation of matrix failure initiation. Segurado and Llorca [318] conducted finite element analyses to determine the influence of particle clustering in cubic RVE reinforced with stiff spherical elastic particles. They revealed that the particles' spatial distribution has no strong effect on the effective properties of the composite in the elastic and plastic regimes. Kari et al. [319] showed that, for a given volume fraction, the influence of the size of the spherical particles on the effective material properties is not significant in the case of linear elasticity. The effect of interface debonding and particle size on behavior of particulate composite materials was studied by Tan et al. [320]. Based on their observations, small and large particles yield hardening and softening behavior, respectively. Chawla et al. [321] studied the influence of different particle shapes (spherical, ellipsoidal, and angular) on the elastic–plastic behavior of particle-reinforced composites. They reported that the shape of the particles may have a considerable impact on the behavior of the composite even for very small strains. Li et al. [322] studied the influence of size, interphase thickness, and inclusion shape on the enhancement mechanism of composites via a closed-form approach based on the Mori–Tanaka scheme. Mortazavi et al. [323] carried out three-dimensional numerical investigations to evaluate the influence of the interphase thickness, second phase geometry, volume fraction, and properties contrast on the effective elastic modulus of nanocomposite RVEs. They demonstrated that the more the inclusion shape deviates from spherical, the more the contrast between the phases influences the effective property. Kochmann and Venturini [324] studied the behavior of a composite with periodic arrangement of stiff interconnected inclusions within a compliant matrix. They showed that such a microstructure results in a composite which exhibits auxetic behavior with auxeticity increasing with increasing Young's modulus mismatch. The effect of the particle size and its distribution, volume fraction, and particle–matrix interface adhesion strength on the macroscopic failure response of heterogeneous adhesives made of stiff particles has been examined by Kulkarni et al. [325] based on a multiscale cohesive framework described in Ref. [326], see also Ref. [327].

1.2.3 Analysis at the RVE Level. To date, numerous schemes have been introduced to perform various analyses over the RVE. Ghosh and Moorthy [328], Ghosh et al. [329], and Moorthy and Ghosh [330] developed *Voronoi cell finite element* scheme to better capture the arbitrary distribution of heterogeneities so as to study the effects of microstructural morphologies on the effective properties. The other technique recently developed is fast Fourier transform (FFT) proposed originally by Moulinec and Suquet [331] and further studied and improved in Ref. [332–338]. The initial idea of the method was to make direct use of the digital images of the real microstructure in the numerical simulation which reduces the effort to generate compatible microstructural finite element discretizations [331]. Michel et al. [339] compared and reviewed the analysis of RVE using the finite element method and FFT. They concluded that the FFT method is computationally superior for linear composites given that the contrast between the phases is not too large. However, the basic model of FFT fails to produce reasonable results in the presence of voids or rigid heterogeneities as its rate of the convergence is proportional to the contrast between the phases. Recently, Monchiet and Bonnet [340] proposed a polarization-based FFT iterative scheme to determine the overall properties of multiphase composites with arbitrary phase contrast, see also Refs. [341–344]. The use of a discrete element formulation to resolve the RVE problem has been addressed in Refs. [345–347] among others, in particular for granular media. Another approach to solve the boundary value problem at the microscale is the boundary element method, studied, for instance, by Kamiński [348], Okada et al. [349], and Procházka [350].

Renard and Marmonier [351] first introduced the idea of using a finite element discretization at the microstructure. This idea has been further developed in Refs. [222] and [352–363]. Moës et al. [364] presented an extended version of the classical finite element method, referred to as XFEM, to solve microproblems involving complex geometries [365]. Feyel [366] introduced the general method of FE^2 in which a spatially resolved RVE discretized by finite elements corresponds to the macroscale integration points of finite elements at the macroscale, and separate finite element computations are performed at the two scales. Although this method is known to be computationally expensive, it is trivially parallelizable as the computations at the microscale are completely independent of each other [367–370]. Also, a number of methods have been recently developed aiming at reducing the computational cost and increasing the accuracy of multiscale analysis [371–375]. These methods are typically based on decomposing the macroscale problem and selective usage of computational techniques discussed in Refs. [5] and [376–378], employing a database to directly map the effective behavior from macroscopic information addressed in Refs. [379–383], transformation field analysis [384–390], or proper orthogonal/generalized decomposition [391–397].

1.2.4 Beyond Purely Elastic Problems. Extension of the computational homogenization scheme to multiphysics problems can be found in Refs. [398–405] for thermomechanical problems, Refs. [406–409] for magnetomechanical problems, Refs. [410–416] for electromechanical problems, and Refs. [417] and [418] for hydromechanical problems, see also Refs. [419] and [420]. Also, see Refs. [421–446] for more details on multiscale modeling of failure, damage, and crack propagation and Refs. [430] and [447–456] for background on modeling instability phenomena such as buckling in the context of multiscale modeling.

1.3 Key Features and Objectives. Computational homogenization is a very mature field with an extensive body of literature. However, some computational aspects seem to require further details. This contribution elaborates on a unifying overview of the first-order strain-driven computational homogenization framework in the context of finite deformations using the finite element method. Special attention is devoted to the presentation of subtle details regarding the computational aspects and implementation of this problem. The key features and objectives of this paper are as follows:

- to detail on the computational implementation using the finite element method
- to study numerically the overall behavior of random microstructures
- to investigate the converging behavior of different boundary conditions when increasing the number of inclusions within the RVE
- to present a concise and clear formulation for computing the macrotangent necessary for the FE^2 approach
- to provide simple numerical examples with enough details to serve as benchmarks
- to demonstrate the influence of the nonlinearity and robustness of the numerical schemes

The rest of this paper is organized as follows. The finite deformation formulations governing the response of the macro- and microstructure, admissible boundary conditions, and the connection between the scales are discussed in Sec. 2. Section 3 furnishes the finite element formulation of the microproblem and details on the computational algorithms to solve the problem. The applicability of the proposed algorithms is elucidated through numerical results for both two- and three-dimensional problems. This is then followed by presenting the finite element formulation of the macroproblem and the associated computational algorithm. At the end of this section, multiple FE^2 simulations are performed. Section 4 summarizes this work. The notations, operators, and key definitions used throughout the paper are listed in the Nomenclature section.

2 Theory

This section elaborates on theoretical aspects of modeling a heterogeneous material whose microstructures are far smaller than the characteristic length of the macroproblem. This separation of scales allows to view the problem as two coupled subproblems at the macro- and the microscale, see Ref. [231] for more details on scale separation. Due to the heterogeneity, it is not easily possible to assign a specific constitutive law to the material at the macroscale. It is assumed that the constitutive responses of the microstructures are known and in a homogenized sense result in the overall macrobehavior. The central idea of computational homogenization is to solve the associated microproblem at each integration point of the macroproblem. This work is mainly based on the *first-order strain-driven computational homogenization*. That is, the input for the problem at the microscale is the macroscopic deformation gradient and outputs are the macroscopic Piola stress as well as the macroscopic Piola tangent. Another possible approach is *stress-driven homogenization* where the macroscopic stress is given at the microscale, and the macroscopic deformation gradient is obtained [457]. This approach is briefly discussed in Appendix B. Strain-driven homogenization is, however, more common as it captures the softening response of the material similar to a displacement-control algorithm. Some of the contents presented in this section bear certain similarities to those proposed in our recent contribution [252], however, for computational homogenization accounting for surface energies. Admittedly, some relations such as macrodeformation gradient ${}^{\mathrm{M}}\boldsymbol{F}$ assume the same format whether or not surface contributions are considered. This, in general, should not be taken for granted though. For instance, the format of the macro Piola stress ${}^{\mathrm{M}}\boldsymbol{P}$ as well as the Hill–Mandel condition given in Ref. [252] differ from their classical definitions here. In this section, fundamental definitions and concepts of the theory of computational homogenization are briefly addressed in order for this paper to be self-contained. In this contribution, all relations are represented only in Lagrangian description, considering that it is straightforward to formulate the problem in Eulerian description [206,402,408,458]. Furthermore, it is possible to establish the homogenization theory based on Green–Lagrange strain and Piola–Kirchhoff stress as alternatively suitable strain and stress measures [459,460].

2.1 Macroproblem Definition. Consider a continuum body that takes the material configuration at time $t=0$ and the spatial configuration at any time $t>0$, as shown in Fig. 1.[4] At the macroscale, the body occupies the material configuration ${}^{\mathrm{M}}\mathcal{B}_0$ with the boundary $\partial^{\mathrm{M}}\mathcal{B}_0$ at time $t=0$. The outward unit normal vector to $\partial^{\mathrm{M}}\mathcal{B}_0$ is denoted as ${}^{\mathrm{M}}\boldsymbol{N}$. The macroscopic spatial configuration is denoted ${}^{\mathrm{M}}\mathcal{B}_t$, with the boundary $\partial^{\mathrm{M}}\mathcal{B}_t$ and the surface unit normal ${}^{\mathrm{M}}\boldsymbol{n}$. A material point at the macroscale, labeled by the position vector ${}^{\mathrm{M}}\boldsymbol{X}$, is mapped to its spatial counterpart ${}^{\mathrm{M}}\boldsymbol{x}$ via the nonlinear deformation map ${}^{\mathrm{M}}\boldsymbol{\varphi}$ according to ${}^{\mathrm{M}}\boldsymbol{x}={}^{\mathrm{M}}\boldsymbol{\varphi}({}^{\mathrm{M}}\boldsymbol{X})$. The macroscopic deformation gradient ${}^{\mathrm{M}}\boldsymbol{F}$ linearly maps a line element $\mathrm{d}^{\mathrm{M}}\boldsymbol{X}$ in the material configuration to a spatial line element $\mathrm{d}^{\mathrm{M}}\boldsymbol{x}$ according to

$$\mathrm{d}^{\mathrm{M}}\boldsymbol{x}={}^{\mathrm{M}}\boldsymbol{F}\cdot\mathrm{d}^{\mathrm{M}}\boldsymbol{X}\qquad\text{and}\qquad{}^{\mathrm{M}}\boldsymbol{F}={}^{\mathrm{M}}\mathrm{Grad}\,{}^{\mathrm{M}}\boldsymbol{\varphi}\tag{1}$$

The equations governing the macroproblem are the balances of linear momentum and angular momentum. In the absence of inertia effects, the balance of linear momentum reads

$$\begin{aligned}&{}^{\mathrm{M}}\mathrm{Div}\,{}^{\mathrm{M}}\boldsymbol{P}+{}^{\mathrm{M}}\boldsymbol{b}_0^{\mathrm{p}}=0\quad\text{in }{}^{\mathrm{M}}\mathcal{B}_0\quad\text{subject to}\\&{}^{\mathrm{M}}\boldsymbol{P}.{}^{\mathrm{M}}\boldsymbol{N}={}^{\mathrm{M}}\boldsymbol{t}_0\quad\text{on }\partial^{\mathrm{M}}\mathcal{B}_0\quad\text{and}\quad{}^{\mathrm{M}}\boldsymbol{t}_0={}^{\mathrm{M}}\boldsymbol{t}_0^{\mathrm{p}}\quad\text{on }\partial^{\mathrm{M}}\mathcal{B}_{0,\mathrm{N}}\end{aligned}\tag{2}$$

with ${}^{\mathrm{M}}\boldsymbol{b}_0^{\mathrm{p}}$ denoting the macroscopic body force density in the material configuration and ${}^{\mathrm{M}}\boldsymbol{P}$ denoting the macroscopic Piola stress. The traction on $\partial^{\mathrm{M}}\mathcal{B}_0$ is ${}^{\mathrm{M}}\boldsymbol{t}_0$, and ${}^{\mathrm{M}}\boldsymbol{t}_0^{\mathrm{p}}$ denotes the prescribed traction on the Neumann portion of the boundary $\partial^{\mathrm{M}}\mathcal{B}_{0,\mathrm{N}}\subset\partial^{\mathrm{M}}\mathcal{B}_0$. The local form of the balance of angular momentum in the macroscopic material configuration reads

$${}^{\mathrm{M}}\boldsymbol{P}.{}^{\mathrm{M}}\boldsymbol{F}^{\mathrm{t}}={}^{\mathrm{M}}\boldsymbol{F}.{}^{\mathrm{M}}\boldsymbol{P}^{\mathrm{t}}\tag{3}$$

For the sake of simplicity of presentation, the material is assumed to be hyperelastic, and thus nondissipative at the microscale and, as a consequence, at the macroscale. Therefore, the macroscopic free energy density ${}^{\mathrm{M}}\psi$ is only a function of the macrodeformation gradient ${}^{\mathrm{M}}\boldsymbol{F}$ as ${}^{\mathrm{M}}\psi={}^{\mathrm{M}}\psi({}^{\mathrm{M}}\boldsymbol{F})$. The Coleman–Noll procedure dictates that for a hyperelastic material, the macro Piola stress ${}^{\mathrm{M}}\boldsymbol{P}$ derives from ${}^{\mathrm{M}}\psi$ as

$${}^{\mathrm{M}}\boldsymbol{P}:=\frac{\partial^{\mathrm{M}}\psi}{\partial^{\mathrm{M}}\boldsymbol{F}}={}^{\mathrm{M}}\boldsymbol{P}({}^{\mathrm{M}}\boldsymbol{F})\tag{4}$$

Consequently, the macro Piola stress can only be a function of the macrodeformation gradient. In order to solve a nonlinear problem using the Newton–Raphson scheme, not only the stress but also the stress tangent is needed. The macroscopic Piola tangent with respect to the macrodeformation gradient is denoted ${}^{\mathrm{M}}\mathbb{A}$ and is a fourth-order tensor

$${}^{\mathrm{M}}\mathbb{A}:=\frac{\partial^{\mathrm{M}}\boldsymbol{P}}{\partial^{\mathrm{M}}\boldsymbol{F}}=\frac{\partial^{2\mathrm{M}}\psi}{\partial^{\mathrm{M}}\boldsymbol{F}^2}={}^{\mathrm{M}}\mathbb{A}({}^{\mathrm{M}}\boldsymbol{F})\tag{5}$$

In general, the macroscopic free energy and its derivatives cannot be expressed explicitly due to the complex microstructures of the material. This fact motivates the central idea of first-order strain-driven computational homogenization. That is, to prescribe the macroscopic deformation gradient ${}^{\mathrm{M}}\boldsymbol{F}$ to the microscale problem and to compute the overall response of the macroproblem as shown in Fig. 1 (right).

2.2 Microproblem Definition. The material configuration at the microscale is denoted $\mathcal{B}_0$ and is assumed to be representative of the material at the macroscale in the sense that it contains enough details to sufficiently capture the microstructural features of the material. See Refs. [185], [231], [270], [282], and [461] for more details on the definition of the RVE. The boundary of the RVE is denoted $\partial\mathcal{B}_0$ with the outward unit normal $\boldsymbol{N}$ (see Fig. 1). The spatial configuration at the microscale is defined in analogy to the material configuration.

Let $\boldsymbol{X}$ be the position vector of a point in $\mathcal{B}_0$. The nonlinear deformation $\boldsymbol{\varphi}$ maps $\boldsymbol{X}$ to its counterpart $\boldsymbol{x}$ in the spatial configuration $\mathcal{B}_t$. A material line element $\mathrm{d}\boldsymbol{X}$ is mapped to its spatial counterpart $\mathrm{d}\boldsymbol{x}$ via the linear deformation map $\boldsymbol{F}=\mathrm{Grad}\,\boldsymbol{\varphi}$. The

[4] In this contribution, we exclude the effect of inertia forces and treat the problem as a quasi-static problem. Therefore, the time in this paper refers to a load evolution parameter.

determinant of the deformation gradient $\boldsymbol{F}$ is denoted as $J := \mathrm{Det}\boldsymbol{F} > 0$ which is the ratio of the volume element in the spatial configuration dv to the volume element in the material configuration dV.

Similar to the macroproblem, the governing equations of the microproblem are the balances of linear and angular momentum. The balance of linear momentum reads

$$\mathrm{Div}\boldsymbol{P} = 0 \quad \text{in } \mathcal{B}_0 \quad \text{subject to} \quad \boldsymbol{P}\cdot\boldsymbol{N} = \boldsymbol{t}_0 \quad \text{on } \partial\mathcal{B}_0 \quad \text{and} \quad \boldsymbol{t}_0 = \boldsymbol{t}_0^{\mathrm{p}} \quad \text{on } \partial\mathcal{B}_{0,\mathrm{N}} \tag{6}$$

in which $\boldsymbol{t}_0$ denotes the traction on the boundary $\partial\mathcal{B}_0$. The prescribed traction on the Neumann portions of the boundary $\partial\mathcal{B}_{0,\mathrm{N}} \subset \partial\mathcal{B}_0$ is denoted as $\boldsymbol{t}_0^{\mathrm{p}}$. The body forces at the microscale are negligible due to the assumption of scale separation. The local form of the balance of angular momentum in the microscopic material configuration is

$$\boldsymbol{P}\cdot\boldsymbol{F}^{\mathrm{t}} = \boldsymbol{F}\cdot\boldsymbol{P}^{\mathrm{t}} \tag{7}$$

Finally, as pointed out earlier, the material response at the microscale is assumed to be hyperelastic with the microscopic free energy density ψ as a function of the microscopic deformation gradient $\boldsymbol{F}$ as $\psi = \psi(\boldsymbol{F})$. From the Coleman–Noll procedure, the micro Piola stress $\boldsymbol{P}$ derives from ψ as

$$\boldsymbol{P} := \frac{\partial\psi}{\partial\boldsymbol{F}} = \boldsymbol{P}(\boldsymbol{F}) \tag{8}$$

and, consequently, can only be a function of the microdeformation gradient $\boldsymbol{F}$. The micro Piola tangent with respect to the microdeformation gradient is denoted by $\mathbb{A}$ and is a fourth-order tensor

$$\mathbb{A} := \frac{\partial\boldsymbol{P}}{\partial\boldsymbol{F}} = \frac{\partial^2\psi}{\partial\boldsymbol{F}^2} = \mathbb{A}(\boldsymbol{F}) \tag{9}$$

As an example, the free energy density function ψ per unit volume in the material configuration for a compressible neo-Hookean material is chosen as

$$\psi(\boldsymbol{F}) = \frac{1}{2}\mu\,[\boldsymbol{F}:\boldsymbol{F} - 3 - 2\,\log J] + \frac{1}{2}\lambda\,\log^2 J \tag{10}$$

with μ and λ denoting the Lamé parameters. The microscopic free energy density (10) results in the micro Piola stress and micro Piola tangent

$$\boldsymbol{P}(\boldsymbol{F}) = \mu\,[\boldsymbol{F} - \boldsymbol{F}^{-\mathrm{t}}] + \lambda\,\log J\,\boldsymbol{F}^{-\mathrm{t}} \tag{11}$$

$$\mathbb{A}(\boldsymbol{F}) = \mu\left[\boldsymbol{I}\,\bar{\otimes}\,\boldsymbol{I} + \boldsymbol{F}^{-\mathrm{t}}\,\underline{\otimes}\,\boldsymbol{F}^{-1}\right] + \lambda\left[\boldsymbol{F}^{-\mathrm{t}}\otimes\boldsymbol{F}^{-\mathrm{t}} - \log J\,\boldsymbol{F}^{-\mathrm{t}}\,\underline{\otimes}\,\boldsymbol{F}^{-1}\right] \tag{12}$$

Two nonstandard tensor products $\bar{\otimes}$ and $\underline{\otimes}$ of two second-order tensors $\boldsymbol{A}$ and $\boldsymbol{B}$ are the fourth-order tensors $\mathbb{D} = \boldsymbol{A}\,\bar{\otimes}\,\boldsymbol{B}$ with components $D_{ijkl} = A_{ik}B_{jl}$ and $\mathbb{C} = \boldsymbol{A}\,\underline{\otimes}\,\boldsymbol{B}$ with $C_{ijkl} = A_{il}B_{jk}$.

In general, the microstructure consists of various materials and each of them has its own material parameters. In this contribution, it is assumed that the microstructure consists of only two types of materials being *inclusions* distributed in a *matrix*. This assumption is only made for the sake of simplicity and in order to focus on the main features of this work. It is straightforward to introduce more materials into this study; nevertheless, it involves more notations and details without providing additional insight into the problem of interest here.

2.3 Micro-to-Macro Transition. Central idea of the first-order strain-driven computational homogenization is to prescribe the macroscopic deformation gradient ${}^{\mathrm{M}}\boldsymbol{F}$ onto the microproblem and to compute the overall response of the microproblem, and in particular, the macro Piola stress ${}^{\mathrm{M}}\boldsymbol{P}$ and macro Piola tangent ${}^{\mathrm{M}}\mathbb{A}$. In this section, microscopic quantities are related to their macroscopic counterparts through volume averaging over the RVE and fundamental reasoning. It proves convenient to define the averaging operator $\langle\{\bullet\}\rangle$ in the material configuration as the integral over the domain $\mathcal{B}_0$ divided by the volume $\mathscr{V}_0$ as

$$\langle\{\bullet\}\rangle := \frac{1}{\mathscr{V}_0}\int_{\mathcal{B}_0}\{\bullet\}\,\mathrm{d}V \qquad \text{with} \qquad \mathscr{V}_0 = \int_{\mathcal{B}_0}\mathrm{d}V \tag{13}$$

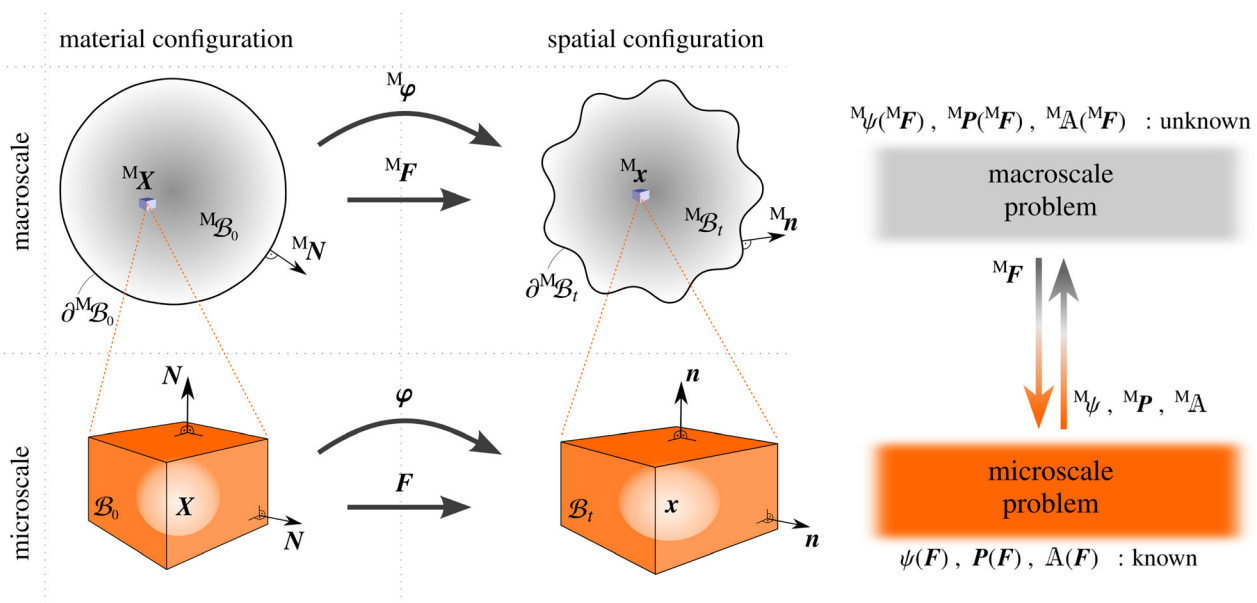

Fig. 1 Graphical summary of computational homogenization. The macroscopic domain ${}^{\mathrm{M}}\mathcal{B}_0$ is mapped to the spatial configuration ${}^{\mathrm{M}}\mathcal{B}_t$ via the nonlinear deformation map ${}^{\mathrm{M}}\varphi$. The domain $\mathcal{B}_0$ corresponds to a microscopic RVE. The motion φ of the RVE is associated with a macroscopic point ${}^{\mathrm{M}}\boldsymbol{X}$ within the bulk. In view of the first-order strain-driven homogenization, the macroscopic deformation gradient is given, and the macro Piola stress and the macro Piola tangent are sought. These quantities are evaluated through solving boundary value problems at the microscale.

The volume $\mathscr{V}_0$ is the total volume surrounded by the (external) boundary $\partial\mathcal{B}_0$. Note that in the case of porous materials, $\mathscr{V}_0$ takes also the pore's volume into account.

2.3.1 Average Piola Stress Theorem. THEOREM. *Let $\boldsymbol{P}_c$ be a given constant stress tensor and $\partial\mathcal{B}_0$ be the entire boundary of the domain $\mathcal{B}_0$ with outward unit normal $\boldsymbol{N}$ as shown in Fig. 1. If $\boldsymbol{P}\cdot\boldsymbol{N}=\boldsymbol{t}_0=\boldsymbol{P}_c\cdot\boldsymbol{N}$ is prescribed on $\partial\mathcal{B}_0$, then $\langle\boldsymbol{P}\rangle=\boldsymbol{P}_c$.*

Proof. In order to prove the average Piola stress theorem, we employ Lemma 1 given in Sec. A.1 of Appendix A which states

$$\langle\boldsymbol{P}\rangle=\frac{1}{\mathscr{V}_0}\int_{\partial\mathcal{B}_0}\boldsymbol{t}_0\otimes\boldsymbol{X}\,\mathrm{d}A \tag{14}$$

Therefore, we have

$$\begin{aligned}\langle\boldsymbol{P}\rangle&=\frac{1}{\mathscr{V}_0}\int_{\partial\mathcal{B}_0}\boldsymbol{t}_0\otimes\boldsymbol{X}\,\mathrm{d}A=\frac{1}{\mathscr{V}_0}\int_{\partial\mathcal{B}_0}\boldsymbol{P}_c\cdot\boldsymbol{N}\otimes\boldsymbol{X}\,\mathrm{d}A\\&=\frac{1}{\mathscr{V}_0}\boldsymbol{P}_c\cdot\int_{\partial\mathcal{B}_0}\boldsymbol{N}\otimes\boldsymbol{X}\,\mathrm{d}A\end{aligned} \tag{15}$$

Using the lemma $\int_{\partial\mathcal{B}_0}\boldsymbol{N}\otimes\boldsymbol{X}\,\mathrm{d}A=\mathscr{V}_0\boldsymbol{I}$ proven in Sec. A.2 of Appendix A, the relation (15) can be written as

$$\langle\boldsymbol{P}\rangle=\frac{1}{\mathscr{V}_0}\boldsymbol{P}_c\cdot[\mathscr{V}_0\boldsymbol{I}]=\boldsymbol{P}_c$$

The average Piola stress theorem states that when a body is subject to the traction $\boldsymbol{P}_c\cdot\boldsymbol{N}$, the Piola stress averaged over the entire body is the same as $\boldsymbol{P}_c$ regardless of the complexity of the stress field within the RVE domain. In the context of the micro-to-macro transition, the average Piola stress theorem motivates the assumption of the macro Piola stress to be the average micro Piola stress as

$${}^{\mathrm{M}}\boldsymbol{P}=\langle\boldsymbol{P}\rangle=\frac{1}{\mathscr{V}_0}\int_{\mathcal{B}_0}\boldsymbol{P}\,\mathrm{d}V=\frac{1}{\mathscr{V}_0}\int_{\partial\mathcal{B}_0}\boldsymbol{t}_0\otimes\boldsymbol{X}\,\mathrm{d}A \tag{16}$$

2.3.2 Average Deformation Gradient Theorem. THEOREM. *Let $\boldsymbol{F}_c$ be a given constant deformation gradient tensor and $\partial\mathcal{B}_0$ be the entire boundary of the domain $\mathcal{B}_0$ with outward unit normal $\boldsymbol{N}$ as shown in Fig. 1. If $\boldsymbol{\varphi}=\boldsymbol{F}_c\cdot\boldsymbol{X}$ is prescribed on $\partial\mathcal{B}_0$, then $\langle\boldsymbol{F}\rangle=\boldsymbol{F}_c$.*

Proof. In order to prove the average deformation gradient theorem, we employ the gradient theorem as follows:

$$\begin{aligned}\langle\boldsymbol{F}\rangle&=\frac{1}{\mathscr{V}_0}\int_{\mathcal{B}_0}\boldsymbol{F}\,\mathrm{d}V=\frac{1}{\mathscr{V}_0}\int_{\mathcal{B}_0}\mathrm{Grad}\boldsymbol{\varphi}\,\mathrm{d}V=\frac{1}{\mathscr{V}_0}\int_{\partial\mathcal{B}_0}\boldsymbol{\varphi}\otimes\boldsymbol{N}\,\mathrm{d}A\\&=\frac{1}{\mathscr{V}_0}\boldsymbol{F}_c\cdot\int_{\partial\mathcal{B}_0}\boldsymbol{X}\otimes\boldsymbol{N}\,\mathrm{d}A\end{aligned} \tag{17}$$

Using the lemma $\int_{\partial\mathcal{B}_0}\boldsymbol{N}\otimes\boldsymbol{X}\,\mathrm{d}A=\mathscr{V}_0\boldsymbol{I}$ proven in Sec. A.2 of Appendix A, the relation (17) can be written as

$$\langle\boldsymbol{F}\rangle=\frac{1}{\mathscr{V}_0}\boldsymbol{F}_c\cdot[\mathscr{V}_0\boldsymbol{I}^{\mathrm{t}}]=\boldsymbol{F}_c\cdot\boldsymbol{I}=\boldsymbol{F}_c$$

The average deformation gradient theorem states that when a body is subject to deformation $\boldsymbol{F}_c\cdot\boldsymbol{X}$ on its boundary, the deformation gradient averaged over the entire body is the same as $\boldsymbol{F}_c$ regardless of the complexity of the deformation gradient field within the RVE domain. In the context of the micro-to-macro transition, the average deformation gradient theorem motivates the assumption of the macrodeformation gradient to be the average microdeformation gradient as

$${}^{\mathrm{M}}\boldsymbol{F}=\langle\boldsymbol{F}\rangle=\frac{1}{\mathscr{V}_0}\int_{\mathcal{B}_0}\boldsymbol{F}\,\mathrm{d}V=\frac{1}{\mathscr{V}_0}\int_{\partial\mathcal{B}_0}\boldsymbol{\varphi}\otimes\boldsymbol{N}\,\mathrm{d}A \tag{18}$$

2.3.3 Hill–Mandel Condition. The celebrated Hill–Mandel condition stipulates incremental internal energy equivalence between the macro- and microscales as

$$\langle\boldsymbol{P}:\delta\boldsymbol{F}\rangle-{}^{\mathrm{M}}\boldsymbol{P}:\delta{}^{\mathrm{M}}\boldsymbol{F}\overset{!}{=}0 \tag{19}$$

In order to solve the microproblem, the boundary conditions on the RVE that satisfy the Hill–Mandel condition must be determined. These are obtained with the aid of Hill's lemma

$$\langle\boldsymbol{P}:\delta\boldsymbol{F}\rangle-{}^{\mathrm{M}}\boldsymbol{P}:\delta{}^{\mathrm{M}}\boldsymbol{F}=\int_{\partial\mathcal{B}_0}\left[\delta\boldsymbol{\varphi}-\delta{}^{\mathrm{M}}\boldsymbol{F}\cdot\boldsymbol{X}\right]\cdot\left[\boldsymbol{t}_0-{}^{\mathrm{M}}\boldsymbol{P}\cdot\boldsymbol{N}\right]\mathrm{d}A \tag{20}$$

proven in Sec. A.3 of Appendix A. Hill's lemma (20) expresses the left-hand side of the Hill–Mandel condition (19) in terms of a surface integral over the boundary of the RVE. Hill's lemma transforms the Hill–Mandel condition into a boundary integral from which suitable boundary conditions can be extracted. In order to satisfy the Hill–Mandel condition, the right-hand side of Eq. (20) should identically vanish. The following conditions sufficiently satisfy the Hill–Mandel condition as can be easily deduced:

- Constant deformation condition in $\mathcal{B}_0$ leading to Voigt's bound (Taylor's assumption)

$$\rightsquigarrow\quad\boldsymbol{\varphi}={}^{\mathrm{M}}\boldsymbol{F}\cdot\boldsymbol{X}\quad\text{in }\mathcal{B}_0$$

- Linear displacement boundary conditions (DBC)

$$\rightsquigarrow\quad\boldsymbol{\varphi}={}^{\mathrm{M}}\boldsymbol{F}\cdot\boldsymbol{X}\quad\text{on }\partial\mathcal{B}_0$$

- Periodic displacement and antiperiodic traction boundary conditions (PBC)

$$\rightsquigarrow\quad\left[\boldsymbol{\varphi}-{}^{\mathrm{M}}\boldsymbol{F}\cdot\boldsymbol{X}\right]:\text{periodic}\quad\text{and}\quad\left[\boldsymbol{t}_0-{}^{\mathrm{M}}\boldsymbol{P}\cdot\boldsymbol{N}\right]:\text{antiperiodic}\quad\text{on }\partial\mathcal{B}_0$$

- Constant traction boundary conditions (TBC)

$$\rightsquigarrow\quad\boldsymbol{t}_0={}^{\mathrm{M}}\boldsymbol{P}\cdot\boldsymbol{N}\quad\text{on }\partial\mathcal{B}_0$$

- Constant stress condition in $\mathcal{B}_0$ leading to Reuss' bound (Sachs' assumption)

$$\rightsquigarrow\quad\boldsymbol{P}={}^{\mathrm{M}}\boldsymbol{P}\quad\text{in }\mathcal{B}_0$$

Note that, for the periodic boundary conditions, antiperiodic traction $\boldsymbol{t}_0$ satisfies the antiperiodicity of $[\boldsymbol{t}_0-{}^{\mathrm{M}}\boldsymbol{P}\cdot\boldsymbol{N}]$ since ${}^{\mathrm{M}}\boldsymbol{P}\cdot\boldsymbol{N}$ is antiperiodic itself due to antiperiodicity of the boundary normals.

Remark on Balance of Angular Momentum. These canonical conditions automatically satisfy the balance of angular momentum at the macroscale and guarantee the symmetry of ${}^{\mathrm{M}}\boldsymbol{P}.{}^{\mathrm{M}}\boldsymbol{F}^{\mathrm{t}}$ [462]. This fact is proven in Sec. A.4 of Appendix A.

2.3.4 Average Piola Tangent Theorem. THEOREM. *Let ${}^{\mathrm{M}}\boldsymbol{F}$ and ${}^{\mathrm{M}}\boldsymbol{P}$ be given macrodeformation gradient tensor and macro Piola stress tensor, respectively, and also, ${}^{\mathrm{M}}\boldsymbol{F}=\langle\boldsymbol{F}\rangle$ and ${}^{\mathrm{M}}\boldsymbol{P}=\langle\boldsymbol{P}\rangle$. The deformation gradient may not be uniform within the RVE but can be decomposed into a uniform part and a zero-mean fluctuation part as $\boldsymbol{F}={}^{\mathrm{M}}\boldsymbol{F}+\tilde{\boldsymbol{F}}$. Let the fourth-order tensor $\mathbb{B}$ be the linear mapping from $\delta{}^{\mathrm{M}}\boldsymbol{F}$ to its fluctuations $\delta\tilde{\boldsymbol{F}}$ as $\delta\tilde{\boldsymbol{F}}=\mathbb{B}:\delta{}^{\mathrm{M}}\boldsymbol{F}$. The macro Piola tangent ${}^{\mathrm{M}}\mathbb{A}$ is, in general, not the average of the micro Piola tangent ${}^{\mathrm{M}}\mathbb{A}\neq\langle\mathbb{A}\rangle$ but it can be computed according to ${}^{\mathrm{M}}\mathbb{A}=\langle\mathbb{A}+\mathbb{A}:\mathbb{B}\rangle$.*

Proof. In order to prove the average Piola tangent theorem stated above, recall that $\delta{}^{\mathrm{M}}\boldsymbol{P}={}^{\mathrm{M}}\mathbb{A}:\delta{}^{\mathrm{M}}\boldsymbol{F}$. Then, from the assumption that the variation of the macro Piola stress is the average of the variation of the micro Piola stress over the RVE domain, we have

$$
\begin{aligned}
\delta^{\mathrm{M}}\boldsymbol{P} &= \langle \delta \boldsymbol{P} \rangle \\
&= \langle \mathbb{A} : \delta \boldsymbol{F} \rangle \\
&= \langle \mathbb{A} : [\delta^{\mathrm{M}}\boldsymbol{F} + \delta\tilde{\boldsymbol{F}}] \rangle \\
&= \langle \mathbb{A} : \delta^{\mathrm{M}}\boldsymbol{F} + \mathbb{A} : \delta\tilde{\boldsymbol{F}} \rangle \\
&= \langle \mathbb{A} : \delta^{\mathrm{M}}\boldsymbol{F} + \mathbb{A} : \mathbb{B} : \delta^{\mathrm{M}}\boldsymbol{F} \rangle \\
&= \underbrace{\langle \mathbb{A} + \mathbb{A} : \mathbb{B} \rangle}_{{}^{\mathrm{M}}\mathbb{A}} : \delta^{\mathrm{M}}\boldsymbol{F}
\end{aligned}
$$

Remark. The framework presented in this section is particularly suitable for purely elastic materials. If capturing inelastic behavior of the material, e.g., damage, is of interest, the Piola stress would not only be a function of the deformation gradient but also of an internal variable. Therefore, the variation of the Piola stress with respect to the internal variable has to be considered as well. Providing every details about this issue would deviate us from the main objective of this contribution, and we refer the interested readers to the in-depth analysis provided by Temizer and Wriggers [463].

3 Computation

3.1 Finite Element Formulation of the Microproblem. In this section, we present a general finite element formulation for solving the boundary value problem at the microscale. We start with deriving the weak form of the balance of linear momentum and then discretize it in space. The resulting nonlinear system of equations is linearized and solved using the Newton–Raphson scheme.

3.1.1 Weak Form. In order to establish the weak form of the governing equation (6), both sides are contracted from the left by a vector valued test function $\delta\boldsymbol{\varphi}$ and integrated over the bulk domain of the material configuration. Employing the divergence theorem and considering that the test function is defined such that it vanishes over the Dirichlet portion of the boundary, the global weak form of the balance of linear momentum reads

$$
\int_{\mathcal{B}_0} \boldsymbol{P} : \mathrm{Grad}\delta\boldsymbol{\varphi}\, \mathrm{d}V - \int_{\partial\mathcal{B}_{0,\mathrm{N}}} \delta\boldsymbol{\varphi} \cdot \boldsymbol{t}_0^{\mathrm{p}}\, \mathrm{d}A \overset{!}{=} 0 \qquad \forall \delta\boldsymbol{\varphi} \in \mathcal{H}_0^1(\mathcal{B}_0) \tag{21}
$$

where $\mathcal{H}_0^1$ denotes the Sobolev space

$$
\mathcal{H}_0^1(\mathcal{B}_0) = \{\boldsymbol{y} = \boldsymbol{y}(\boldsymbol{X}) : \boldsymbol{y}, \mathrm{Grad}\boldsymbol{y} \in \mathcal{L}^2(\mathcal{B}_0), \boldsymbol{y} = 0 \text{ on } \partial\mathcal{B}_{0,\mathrm{D}}\} \tag{22}
$$

and $\partial\mathcal{B}_{0,\mathrm{D}}$ denotes the Dirichlet portion of the boundary $\partial\mathcal{B}_{0,\mathrm{D}} \subset \partial\mathcal{B}_0$.

3.1.2 Discretization. Next, the material domain is discretized into sets of bulk and surface elements as

$$
\overset{\#\mathrm{be}}{\underset{\beta=1}{\mathbf{A}}} \int_{\mathcal{B}_0^\beta} \boldsymbol{P} : \mathrm{Grad}\delta\boldsymbol{\varphi}\, \mathrm{d}V - \overset{\#\mathrm{se}}{\underset{\gamma=1}{\mathbf{A}}} \int_{\partial\mathcal{B}_{0,\mathrm{N}}^\gamma} \delta\boldsymbol{\varphi} \cdot \boldsymbol{t}_0^{\mathrm{p}}\, \mathrm{d}A \overset{!}{=} 0 \tag{23}
$$

where #be and #se represent the number of bulk and surface elements, respectively. The domain of the bulk element β is denoted $\mathcal{B}_0^\beta$, and $\partial\mathcal{B}_{0,\mathrm{N}}^\gamma$ denotes the domain of the surface element γ upon which traction, and not deformation, is prescribed.

The geometries of the bulk and surface elements are approximated using the natural coordinates $\boldsymbol{\xi}$. The Bubnov–Galerkin finite element method and standard interpolations together with the isoparametric concept are employed as follows:

$$
\begin{aligned}
\boldsymbol{X}|_{\mathcal{B}_0^\beta} &\approx \boldsymbol{X}(\boldsymbol{\xi}) = \sum_{\alpha=1}^{\#\mathrm{nbe}} N^\alpha(\boldsymbol{\xi})\boldsymbol{X}^\alpha \qquad \boldsymbol{X}|_{\partial\mathcal{B}_{0,\mathrm{N}}^\gamma} \approx \boldsymbol{X}(\boldsymbol{\xi}) = \sum_{\alpha=1}^{\#\mathrm{nse}} N^\alpha(\boldsymbol{\xi})\boldsymbol{X}^\alpha \\
\boldsymbol{x}|_{\mathcal{B}_0^\beta} &\approx \boldsymbol{x}(\boldsymbol{\xi}) = \sum_{\alpha=1}^{\#\mathrm{nbe}} N^\alpha(\boldsymbol{\xi})\boldsymbol{x}^\alpha \qquad \boldsymbol{x}|_{\partial\mathcal{B}_{0,\mathrm{N}}^\gamma} \approx \boldsymbol{x}(\boldsymbol{\xi}) = \sum_{\alpha=1}^{\#\mathrm{nse}} N^\alpha(\boldsymbol{\xi})\boldsymbol{x}^\alpha \\
\delta\boldsymbol{\varphi}|_{\mathcal{B}_0^\beta} &\approx \delta\boldsymbol{\varphi}(\boldsymbol{\xi}) = \sum_{\alpha=1}^{\#\mathrm{nbe}} N^\alpha(\boldsymbol{\xi})\delta\boldsymbol{\varphi}^\alpha \qquad \delta\boldsymbol{\varphi}|_{\partial\mathcal{B}_{0,\mathrm{N}}^\gamma} \approx \delta\boldsymbol{\varphi}(\boldsymbol{\xi}) = \sum_{\alpha=1}^{\#\mathrm{nse}} N^\alpha(\boldsymbol{\xi})\delta\boldsymbol{\varphi}^\alpha
\end{aligned} \tag{24}
$$

where N denotes the shape functions. Note that we use the same notation for the shape functions of the bulk and surface elements. However, they shall not be mistaken as their domains are different. That is, N in Eq. $(24)_{\mathrm{left}}$ denotes the shape functions of the bulk element defined on $\boldsymbol{\xi} \in [-1,1]^{\mathrm{PD}}$, and N in Eq. $(24)_{\mathrm{right}}$ denotes the shape functions of the boundary element defined on $\boldsymbol{\xi} \in [-1,1]^{\mathrm{PD}-1}$ with PD being the problem dimension. Number of nodes per bulk and surface elements are represented by #nbe and #nse, respectively.

The fully discrete weak form of the balance of linear momentum is obtained by replacing the test functions in Eq. (23) with their spatial approximations defined in Eq. (24). The fully discrete form of residual vector associated with the global node I reads

$$
\boldsymbol{R}^I := \underbrace{\overset{\#\mathrm{be}}{\underset{\beta=1}{\mathbf{A}}} \int_{\mathcal{B}_0^\beta} \boldsymbol{P} \cdot \mathrm{Grad}N^i\, \mathrm{d}V}_{\boldsymbol{R}^I_{\mathrm{int}}} - \underbrace{\overset{\#\mathrm{se}}{\underset{\gamma=1}{\mathbf{A}}} \int_{\partial\mathcal{B}_{0,\mathrm{N}}^\gamma} \boldsymbol{t}_0^{\mathrm{p}} \cdot N^i\, \mathrm{d}A}_{\boldsymbol{R}^I_{\mathrm{ext}}} \overset{!}{=} \boldsymbol{0} \tag{25}
$$

where i is the local node corresponding to the global node I. We denote the first and second terms of Eq. (25) as $\boldsymbol{R}^I_{\mathrm{int}}$ and $\boldsymbol{R}^I_{\mathrm{ext}}$ representing all the internal and external forces acting on node I, respectively. The nodal residuals are arranged in a global residual vector $\mathbf{R}$, and the fully discrete nonlinear system of governing equations becomes

$$
\mathbf{R} = \mathbf{R}(\mathbf{d}) \overset{!}{=} 0, \quad \mathbf{R} = \mathbf{R}_{\mathrm{int}} + \mathbf{R}_{\mathrm{ext}} \tag{26}
$$

where $\mathbf{d}$ is the unknown global vector of deformations, and $\mathbf{R}_{\mathrm{int}}$ and $\mathbf{R}_{\mathrm{ext}}$ are the assembled vectors of $\boldsymbol{R}^I_{\mathrm{int}}$ and $\boldsymbol{R}^I_{\mathrm{ext}}$, respectively. Note that we use upright letters for assembled vectors in Eq. (26) to distinguish them from the global nodal vectors in Eq. (25). The same argument holds for the tangent stiffness in Sec. 3.1.3.

3.1.3 Linearization. In order to find the solution of the system (26), the Newton–Raphson scheme is utilized. The consistent linearization of the resulting system of equations yields

$$
\begin{aligned}
&\mathbf{R}(\mathbf{d}_{n+1}) = \mathbf{R}(\mathbf{d}_n) + \mathbf{K} \cdot \Delta\mathbf{d}_n \overset{!}{=} 0 \quad \text{with} \quad \mathbf{K} = \frac{\partial \mathbf{R}}{\partial \mathbf{d}}\Big|_n, \\
&\mathbf{d}_{n+1} = \mathbf{d}_n + \Delta\mathbf{d}_n
\end{aligned} \tag{27}
$$

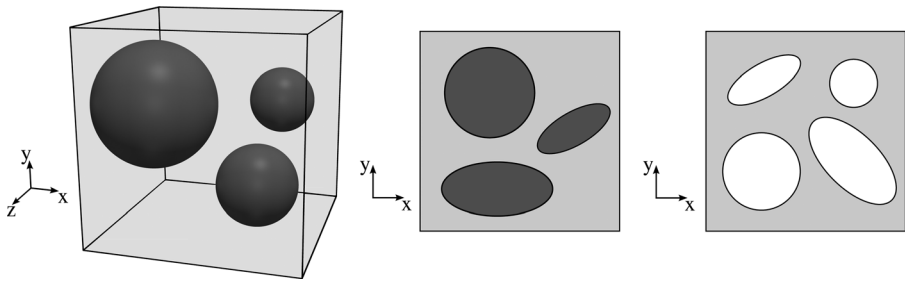

Fig. 2 Examples of three- and two-dimensional microstructures: cubic microstructure with random distribution of spherical particles (left), rectangular microstructures with random shape and distribution of the inclusions (middle), and pores (right)

where n is the iteration step and $\mathbf{K}$ is the assembled tangent stiffness matrix of nodal stiffness

$$\boldsymbol{K}^{IJ} = \int_{\mathcal{B}_0} \frac{\partial \boldsymbol{P}}{\partial \boldsymbol{F}} \bar{:} [\mathrm{Grad}N^I \otimes \mathrm{Grad}N^J] \, \mathrm{d}V \tag{28}$$

The nonstandard (double) contraction $\bar{:}$ of a fourth-order tensor $\mathbb{A}$ and a second-order tensor $\boldsymbol{B}$ is a second-order tensor $\boldsymbol{C} = \mathbb{A} \bar{:} \boldsymbol{B}$ with components $C_{ik} = A_{ijkl}B_{jl}$. Here, we assume that the prescribed traction is constant and is not a follower force, thus $\partial \mathbf{R}_{\mathrm{ext}}/\partial \mathbf{d} = 0$. Solving Eq. (27) yields the iterative increment $\Delta \mathbf{d}_n$ and consequently $\mathbf{d}_{n+1}$.

3.2 Microdeformation Implementation. While computational algorithms to implement DBC and PBC are well established and discussed by many authors [241,246,462,464,465], special care should be taken to deal with the stiffness matrix singularity due to prescribing a pure Neumann boundary condition on the RVE to implement TBC. Several authors have treated this problem using either mass-type diagonal perturbation to regularize the stiffness matrix [462], construction of a free-flexibility matrix to preserve the rigid body modes [466], adding very soft materials to the microstructure, or in the most extreme case, completely fixing enough degrees-of-freedom to make the problem well defined. Here, we present a geometrically independent yet computationally inexpensive and robust algorithm to implement TBC for finite deformation analysis. This section details on the computational algorithms to implement TBC and Sachs' assumption. Furthermore, we briefly cover the computational algorithms to implement the Taylor's assumption, DBC, and PBC for the sake of completeness and in order to demonstrate the similarities and differences among various boundary conditions. The input of all algorithms is the macrodeformation gradient, and the output is the macro Piola stress. The derivation of the macro Piola tangent will be discussed in detail in Sec. 3.4.

Throughout this section, we assume that the microstructure consists of two different materials: the matrix and the inclusion. The matrix is assumed to be a rectangular sample filling the two-dimensional space in $[0, 1]^2$ with inclusions of arbitrary shape and distribution. In the limit of extremely compliant inclusions, the microstructure represents porous media. We will also consider three-dimensional microstructures filling the space in $[0, 1]^3$.

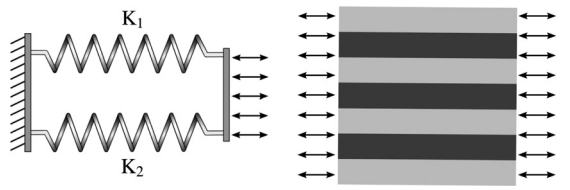

Fig. 4 Taylor's assumption representations via system of parallel springs and multiphase composites

Figure 2 illustrates three sample microstructures. In the following sections, we often show the material configuration of the RVE with a gray-border square and do not depict the microstructure details so as to avoid cluttered figures.

3.2.1 Taylor's Assumption. Taylor's assumption, also referred to as isostrain condition, assumes a linear homogeneous mapping of the entire RVE domain and is implemented by deforming both the inclusion and the matrix identically and according to the macrodeformation gradient. This is illustrated in Fig. 3. Note that the choice of rectangular inclusions in Fig. 3 is only to highlight the linear homogeneous deformation within the microstructure and shall not be understood as any kind of limitation on the generality of the presented framework.

Under the Taylor's assumption, the stress equilibrium at the interface between the inclusion and the matrix is violated. The apparent property of the material obtained under this condition and the classical Voigt's bound coincide in the linear regime. As depicted in Fig. 4, the Taylor's assumption can be resembled by a set of parallel springs or a multiphase composite with parallel constituents aligned in the direction of the applied displacement such that they all share the same deformation.

This configuration furnishes the stiffest possible response from two or more springs or constituents. Consequently, the overall response of the microstructure under this condition is highly overestimated referred to as Voigt's (Taylor's) bound. The algorithm to implement the Taylor's assumption is given as follows:

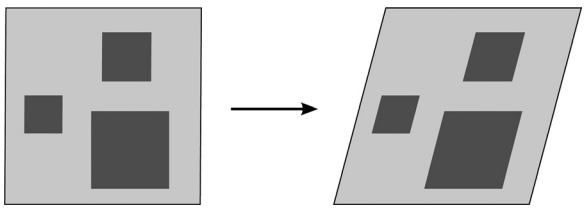

Fig. 3 The inclusions and the matrix deform identically under the Taylor's assumption

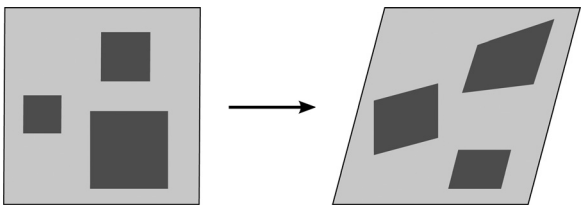

Fig. 5 The inclusions and the matrix do not necessarily deform identically under DBC

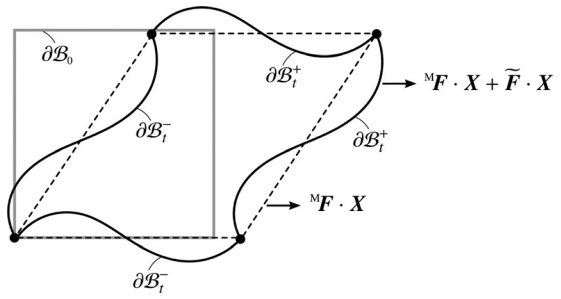

Fig. 6 Graphical illustration of PBC implementation setting. The boundary of the RVE is decomposed into minus and plus parts. Positions of the boundary nodes are determined through two distinct fields: $^{M}\boldsymbol{F}\cdot\boldsymbol{X}$ and $\tilde{\boldsymbol{F}}\cdot\boldsymbol{X}$.

Algorithm 1: Taylor's assumption

input: $^{M}\boldsymbol{F}$, material parameters, f (inclusion volume fraction)
create two separate unit elements representing the inclusion and the matrix;
assign Dirichlet BC to the boundaries of the unit elements;
prescribe boundary nodes deformations according to $^{M}\boldsymbol{F}$;
evaluate volume average of the Piola stress in the inclusion $\langle\boldsymbol{P}\rangle^{f}$ and in the matrix $\langle\boldsymbol{P}\rangle^{m}$;
output: $^{M}\boldsymbol{P}=f\langle\boldsymbol{P}\rangle^{f}+[1-f]\langle\boldsymbol{P}\rangle^{m}$

3.2.2 Linear Displacement Boundary Conditions. Implementation of DBC is carried out by prescribing the deformations on the boundary nodes according to the macrodeformation gradient while the inner nodes are free. The displacements of the inner nodes are updated accordingly such that the residual vector is minimized. This is in contrast to Taylor's assumption where the deformations of all the nodes are prescribed (see Fig. 5). The algorithm to implement DBC is given as follows:

Algorithm 2: Linear displacement boundary conditions

input: $^{M}\boldsymbol{F}$, **material parameters**
assign Dirichlet BC to the boundary nodes;
prescribe boundary nodes deformations through $^{M}\boldsymbol{F}$ incrementally;
solve the system of equations (27);
update inner nodes positions;
output: $^{M}\boldsymbol{P}=\langle\boldsymbol{P}\rangle$

3.2.3 Periodic Displacement and Antiperiodic Traction Boundary Conditions. In order to implement PBC, the RVE boundary in both the material and the spatial configuration is decomposed into two disjoint sets as shown in Fig. 6: a minus part $\partial\mathcal{B}_0^-$, $\partial\mathcal{B}_t^-$ and a plus part $\partial\mathcal{B}_0^+$, $\partial\mathcal{B}_t^+$ with $\partial\mathcal{B}_0^-\cup\partial\mathcal{B}_0^+=\partial\mathcal{B}_0$ and $\partial\mathcal{B}_t^-\cup\partial\mathcal{B}_t^+=\partial\mathcal{B}_t$.

Any quantity on minus and plus parts is denoted as $\{\bullet\}^-$ and $\{\bullet\}^+$, respectively, and $\{\bullet\}^*$ denotes quantities within the bulk domain. Following these notations, and considering that no external force is exerted on the bulk domain, i.e., $\boldsymbol{R}^*_{\text{ext}}=0$, the system of equations (27) can be represented as

$$\begin{bmatrix}\boldsymbol{R}^-_{\text{int}}+\boldsymbol{R}^-_{\text{ext}}\\ \boldsymbol{R}^*_{\text{int}}\\ \boldsymbol{R}^+_{\text{int}}+\boldsymbol{R}^+_{\text{ext}}\end{bmatrix}+\begin{bmatrix}\boldsymbol{K}^{--} & \boldsymbol{K}^{-*} & \boldsymbol{K}^{-+}\\ \boldsymbol{K}^{*-} & \boldsymbol{K}^{**} & \boldsymbol{K}^{*+}\\ \boldsymbol{K}^{+-} & \boldsymbol{K}^{+*} & \boldsymbol{K}^{++}\end{bmatrix}\begin{bmatrix}\Delta\boldsymbol{x}^-\\ \Delta\boldsymbol{x}^*\\ \Delta\boldsymbol{x}^+\end{bmatrix}=0 \tag{29}$$

Based on the fact that the deformation gradient at the RVE level can be decomposed into a uniform part and a fluctuation part as $\boldsymbol{F}=^{M}\boldsymbol{F}+\tilde{\boldsymbol{F}}$, two distinct fields contribute to the positions of the boundary nodes: a homogeneous field given by the linear mapping through the macroscopic deformation gradient $^{M}\boldsymbol{F}\cdot\boldsymbol{X}$ and a nonhomogeneous fluctuation field $\tilde{\boldsymbol{F}}\cdot\boldsymbol{X}$ as

$$\boldsymbol{x}^+=^{M}\boldsymbol{F}\cdot\boldsymbol{X}^++\tilde{\boldsymbol{F}}\cdot\boldsymbol{X}^+,\quad \boldsymbol{x}^-=^{M}\boldsymbol{F}\cdot\boldsymbol{X}^-+\tilde{\boldsymbol{F}}\cdot\boldsymbol{X}^- \tag{30}$$

The deformation fluctuation field on the opposite boundary nodes is assumed to be periodic in a PBC implementation. That is, $\tilde{\boldsymbol{F}}\cdot\boldsymbol{X}^+=\tilde{\boldsymbol{F}}\cdot\boldsymbol{X}^-$, and therefore, from Eq. (30) it follows that

$$\boldsymbol{x}^+-\boldsymbol{x}^-=^{M}\boldsymbol{F}\cdot[\boldsymbol{X}^+-\boldsymbol{X}^-]\quad\Longleftrightarrow\quad\boldsymbol{x}^+=^{M}\boldsymbol{F}\cdot[\boldsymbol{X}^+-\boldsymbol{X}^-]+\boldsymbol{x}^- \tag{31}$$

Hence, the displacements of the opposite boundary nodes are equal to each other, $\Delta\boldsymbol{x}^+=\Delta\boldsymbol{x}^-$, and one of them can be eliminated from the system of equations (29). Here, we omit $\Delta\boldsymbol{x}^+$ from the system by adding the columns of the stiffness matrix associated with the opposite boundary nodes as

$$\begin{bmatrix}\boldsymbol{R}^-_{\text{int}}+\boldsymbol{R}^-_{\text{ext}}\\ \boldsymbol{R}^*_{\text{int}}\\ \boldsymbol{R}^+_{\text{int}}+\boldsymbol{R}^+_{\text{ext}}\end{bmatrix}+\begin{bmatrix}\boldsymbol{K}^{--}+\boldsymbol{K}^{-+} & \boldsymbol{K}^{-*}\\ \boldsymbol{K}^{*-}+\boldsymbol{K}^{*+} & \boldsymbol{K}^{**}\\ \boldsymbol{K}^{+-}+\boldsymbol{K}^{++} & \boldsymbol{K}^{+*}\end{bmatrix}\begin{bmatrix}\Delta\boldsymbol{x}^-\\ \Delta\boldsymbol{x}^*\end{bmatrix}=0 \tag{32}$$

The antiperiodicity of $\boldsymbol{t}_0$ is enforced by assuming that the parallel boundary nodes have the same traction but in opposite directions. Under such assumption, the nodal external residual on the opposite boundary nodes satisfy $\boldsymbol{R}^+_{\text{ext}}=-\boldsymbol{R}^-_{\text{ext}}$. So, the system of equations (32) can be further reduced by adding the first and the last rows corresponding to $\boldsymbol{R}^-$ and $\boldsymbol{R}^+$, respectively, to each other as

$$\begin{bmatrix}\cancel{\boldsymbol{R}^-_{\text{ext}}+\boldsymbol{R}^+_{\text{ext}}}^{\,0}+\boldsymbol{R}^-_{\text{int}}+\boldsymbol{R}^+_{\text{int}}\\ \boldsymbol{R}^*_{\text{ext}}\end{bmatrix}+\begin{bmatrix}\boldsymbol{K}^{-+}+\boldsymbol{K}^{--}+\boldsymbol{K}^{++}+\boldsymbol{K}^{+-} & \boldsymbol{K}^{-*}+\boldsymbol{K}^{+*}\\ \boldsymbol{K}^{*+}+\boldsymbol{K}^{*-} & \boldsymbol{K}^{**}\end{bmatrix}\begin{bmatrix}\Delta\boldsymbol{x}^-\\ \Delta\boldsymbol{x}^*\end{bmatrix}=0 \tag{33}$$

Once $\Delta\boldsymbol{x}^-$ is evaluated, it is used to update the positions of all the boundary nodes.

In order to remove the rigid body motions, the motion of one of the corner nodes is prescribed and set to zero. This makes the deformation fluctuations associated to all other corners to vanish according to the deformation fluctuation periodicity assumption of PBC. Hence, the deformations of the corner nodes are determined only through the macroscopic deformation gradient. The algorithm to implement PBC is given as follows:

Algorithm 3: Periodic displacement and antiperiodic traction boundary conditions

input: $^{M}\boldsymbol{F}$, **material parameters**
assign Dirichlet BC to the corner nodes;
prescribe corner nodes deformations through $^{M}\boldsymbol{F}$ incrementally;
$\boldsymbol{x}^+=^{M}\boldsymbol{F}\cdot[\boldsymbol{X}^+-\boldsymbol{X}^-]+\boldsymbol{x}^-$;
solve the reduced system of equations (33);
$\boldsymbol{x}^-=\boldsymbol{X}^-+\Delta\boldsymbol{x}^-$ and $\boldsymbol{x}^*=\boldsymbol{X}^*+\Delta\boldsymbol{x}^*$;
$\boldsymbol{x}^+=^{M}\boldsymbol{F}\cdot[\boldsymbol{X}^+-\boldsymbol{X}^-]+\boldsymbol{x}^-$;
output: $^{M}\boldsymbol{P}=\langle\boldsymbol{P}\rangle$

3.2.4 Constant Traction Boundary Conditions. Implementation of TBC is performed by prescribing $^{M}\boldsymbol{P}\cdot\boldsymbol{N}$ uniformly on the boundary of the material configuration with $^{M}\boldsymbol{P}$ being constant. At the beginning of the algorithm, $^{M}\boldsymbol{P}$ is unknown. Therefore, an initial guess for the macro Piola stress is required to start the algorithm. We initiate $^{M}\boldsymbol{P}$ with zero. It is then updated iteratively until the volume average of the deformation gradient reaches the macrodeformation gradient, that is, until $\langle\boldsymbol{F}\rangle=^{M}\boldsymbol{F}$.

In order to cope with the singularity of the stiffness matrix due to prescribing purely Neumann boundary condition, sufficient constraints should be added to eliminate rigid body motions using

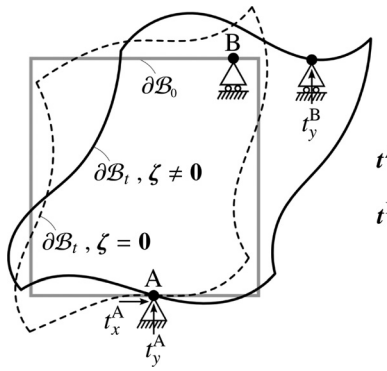

Fig. 7 The entire boundary $\partial\mathcal{B}_0$ except point A in both directions and point B in *y*-direction is prescribed with ${}^M\boldsymbol{P} \cdot \boldsymbol{N}$. Point A is fixed in both directions and point B is fixed in *y*-direction so as to remove rigid body motions. Fixing these points can lead to introduction of spurious forces on the Dirichlet part of the boundary. The spurious tractions are denoted $\boldsymbol{\zeta}$. The dashed line and the solid black line indicate the deformation of the microstructure in the absence and presence of the spurious forces, respectively.

semi-Dirichlet boundary conditions. First, we assign Dirichlet boundary conditions to three degrees-of-freedom in two-dimensional problems and six degrees-of-freedom in three-dimensional problems. Second, at the same time, we guarantee that the Dirichlet part possesses the same traction identical to the prescribed traction on the Neumann part so as to meet the necessary assumption of the TBC, namely, uniform distribution of traction over the entire boundary of the RVE. This is performed by modifying the locations of the semi-Dirichlet constraints such that they accommodate for TBC. This procedure is further elaborated in what follows.

In order to remove translational rigid body motions, a Dirichlet boundary condition is assigned to an arbitrary point A on the material configuration boundary in both directions (see Fig. 7). Assigning Dirichlet boundary conditions to any other point (e.g., point B with $X_x^B \neq X_x^A$) in *y*-direction eliminates the rotational rigid body motions. But, if the solution of the TBC, illustrated using the dashed line in Fig. 7, necessitates point B to displace in the direction that it is fixed, extra reaction forces (in addition to the contributions from ${}^M\boldsymbol{P} \cdot \boldsymbol{N}$) would exert on the Dirichlet part resulting in inaccurate and unrealistic displacements and stresses. Henceforth, we denote these extra forces as *spurious forces* in the sense that they violate the essential prerequisite of the constant traction boundary conditions. The corresponding spurious tractions are denoted $\boldsymbol{\zeta}$.

The total nodal traction on points A and B considering the existence of the spurious tractions reads $\boldsymbol{t}^A = {}^M\boldsymbol{P} \cdot \boldsymbol{N}^A + \boldsymbol{\zeta}^A$ and $\boldsymbol{t}^B = {}^M\boldsymbol{P} \cdot \boldsymbol{N}^B + \boldsymbol{\zeta}^B$ with $\boldsymbol{\zeta}$ being the spurious traction vector, $\zeta_x^A = 0$ and $\zeta_y^A = -\zeta_y^B$. Accordingly, the volume average of the Piola stress reads

$$\begin{aligned}\langle \boldsymbol{P} \rangle &= \frac{1}{\mathscr{V}_0}\int_{\partial\mathcal{B}_0} \boldsymbol{t}_0^p \otimes \boldsymbol{X}\, \mathrm{d}A = \frac{1}{\mathscr{V}_0}\int_{\partial\mathcal{B}_0} [{}^M\boldsymbol{P} \cdot \boldsymbol{N}] \otimes \boldsymbol{X}\, \mathrm{d}A \\ &+ \frac{1}{\mathscr{V}_0}\sum_{i=\mathrm{A,B}} \boldsymbol{\zeta}^i \otimes \boldsymbol{X}^i\, \delta A^i = {}^M\boldsymbol{P} \\ &+ \frac{1}{\mathscr{V}_0}\left\{ \begin{bmatrix} 0 \\ \zeta_y^A \end{bmatrix} \otimes \begin{bmatrix} X_x^A \\ X_y^A \end{bmatrix} + \begin{bmatrix} 0 \\ \zeta_y^B \end{bmatrix} \otimes \begin{bmatrix} X_x^B \\ X_y^B \end{bmatrix} \right\} \delta A = {}^M\boldsymbol{P} \\ &+ \frac{1}{\mathscr{V}_0}\begin{bmatrix} 0 & 0 \\ \zeta_y^A X_x^A + \zeta_y^B X_x^B & \zeta_y^A X_y^A + \zeta_y^B X_y^B \end{bmatrix} \delta A\end{aligned}$$

assuming that the effective nodal areas of points A and B are identical and equal to δA. In order to ensure that the Dirichlet part is under the same traction as prescribed on the Neumann part, both ζ_y^A and ζ_y^B must always vanish.

Recall that the positions of points A and B on the material configuration are arbitrary. A simple concrete case is to assign point A to [0,0] and point B to [1,0], as illustrated in Fig. 8. Based on this setting, the volume average of the Piola stress reads

$$\langle \boldsymbol{P} \rangle = {}^M\boldsymbol{P} + \frac{1}{\mathscr{V}_0}\begin{bmatrix} 0 & 0 \\ \zeta_y^B & 0 \end{bmatrix} \delta A \tag{34}$$

from which the required condition to suppress the spurious traction component ζ_y^B is derived as

$$\zeta_y^B \stackrel{!}{=} 0 \iff \langle P_{yx} \rangle - {}^M P_{yx} \stackrel{!}{=} 0 \tag{35}$$

In order to satisfy this condition, rather than fixing the point B in its initial position on the material configuration, we prescribe and successively update the position of this point in *y*-direction until it no longer introduces an extra traction.

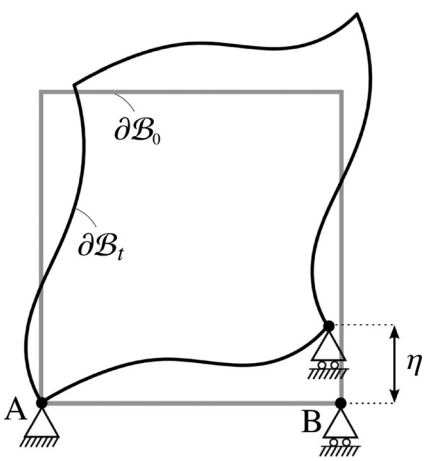

Fig. 8 Graphical illustration of the TBC implementation setting. We prescribe and update ${}^M\boldsymbol{P} \cdot \boldsymbol{N}$ and η iteratively until $\langle F \rangle - {}^M F \stackrel{!}{=} 0$ and $\zeta_y^B \stackrel{!}{=} 0$ are satisfied.

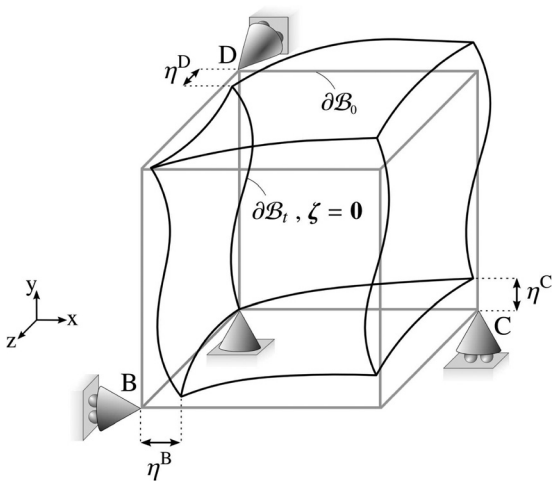

Fig. 9 Graphical illustration of the TBC implementation setting in three-dimensional problems. We prescribe and update ${}^M\boldsymbol{P} \cdot \boldsymbol{N}$, η^B, η^C, and η^D iteratively until $\langle F \rangle - {}^M F \stackrel{!}{=} 0$, $\zeta_x^B \stackrel{!}{=} 0$, $\zeta_y^C \stackrel{!}{=} 0$, and $\zeta_z^D \stackrel{!}{=} 0$ are satisfied. Note that point D is free to move in *x*- and *y*-directions.

On the other hand, in order to reach the macroscopic deformation gradient, the condition $\langle \boldsymbol{F} \rangle - {}^{\mathrm{M}}\boldsymbol{F} \stackrel{!}{=} 0$ must be satisfied. These conditions are inserted into a vector denoted as error vector $\boldsymbol{\Omega}$ which is a nonlinear function of ${}^{\mathrm{M}}\boldsymbol{P}$ and η

$$\boldsymbol{\Omega}({}^{\mathrm{M}}\boldsymbol{P}, \eta) = \left[\langle \boldsymbol{F} \rangle - {}^{\mathrm{M}}\boldsymbol{F}, \zeta_y^{\mathrm{B}} \right]^{\mathrm{t}} \stackrel{!}{=} 0 \tag{36}$$

with η being the displacement to be prescribed at point B in y-direction. The consistent linearization of this nonlinear vector function reads

$$\begin{aligned} &\boldsymbol{\Omega}\left({}^{\mathrm{M}}\boldsymbol{P}_{n+1}, \eta_{n+1}\right) = \boldsymbol{\Omega}\left({}^{\mathrm{M}}\boldsymbol{P}_n, \eta_n\right) + \frac{\partial \boldsymbol{\Omega}}{\partial {}^{\mathrm{M}}\boldsymbol{P}}|_n : \Delta {}^{\mathrm{M}}\boldsymbol{P}_n \\ &+ \frac{\partial \boldsymbol{\Omega}}{\partial \eta}|_n \Delta\eta_n \stackrel{!}{=} 0 \; {}^{\mathrm{M}}\boldsymbol{P}_{n+1} = {}^{\mathrm{M}}\boldsymbol{P}_n + \Delta {}^{\mathrm{M}}\boldsymbol{P}_n, \quad \eta_{n+1} = \eta_n + \Delta\eta_n \end{aligned} \tag{37}$$

where n is the iteration step. Solving Eq. (37) yields the iterative increment $\Delta {}^{\mathrm{M}}\boldsymbol{P}_n$, $\Delta\eta_n$ and consequently ${}^{\mathrm{M}}\boldsymbol{P}_{n+1}$ and η_{n+1}. The algorithm to implement TBC is given as follows:

Algorithm 4: Constant traction boundary conditions

input: ${}^{\mathrm{M}}\boldsymbol{F}$, **material parameters**
  ${}^{\mathrm{M}}\boldsymbol{P} = 0, \eta = 0$;
  assign homogeneous Dirichlet and semi-Dirichlet BC to eliminate rigid body motion;
  while ${}^{\mathrm{M}}\boldsymbol{P}$ *and* η *are not correct* **do**
    apply ${}^{\mathrm{M}}\boldsymbol{P} \cdot \boldsymbol{N}$ on the Neumann part and update semi-Dirichlet BC;
    Solve the system of equations (27);
    evaluate $\langle \boldsymbol{P} \rangle$ and $\langle \boldsymbol{F} \rangle$;
    $\boldsymbol{\Omega}({}^{\mathrm{M}}\boldsymbol{P}, \eta) = \left[\langle \boldsymbol{F} \rangle - {}^{\mathrm{M}}\boldsymbol{F}, \langle P_{yx} \rangle - {}^{\mathrm{M}}P_{yx} \right]^{\mathrm{t}}$;
    if $||\boldsymbol{\Omega}|| < \mathrm{tol}$ **then**
      ${}^{\mathrm{M}}\boldsymbol{P}$ and η are correct
    else
      solve the system of equations (37);
      ${}^{\mathrm{M}}\boldsymbol{P} = {}^{\mathrm{M}}\boldsymbol{P} + \Delta {}^{\mathrm{M}}\boldsymbol{P}$;
      $\eta = \eta + \Delta\eta$;
    end
  end
output: ${}^{\mathrm{M}}\boldsymbol{P}$

In three-dimensional problems, six degrees-of-freedom need to be fixed to prevent rigid body motions. Figure 9 illustrates how to implement TBC in three-dimensional space. Similar to two-dimensional problem, it is performed through assigning Dirichlet boundary condition to point A in x-, y-, and z-directions to eliminate translational rigid body motions and semi-Dirichlet boundary conditions to the points B in x-direction, C in y-direction, and D in z-direction to remove rotational rigid body motions. That is, we first assign Dirichlet boundary conditions to these degrees-of-freedom and then update their locations until a uniform distribution of traction on the RVE is achieved. Prescribing any location on these degrees-of-freedom not identical to their final locations leads to the evolution of spurious forces on the Dirichlet part of the boundary. Taking the existence of spurious forces into account, the total nodal tractions on points A, B, C, D read $\boldsymbol{t}^i = {}^{\mathrm{M}}\boldsymbol{P} \cdot \boldsymbol{N}^i + \boldsymbol{\zeta}^i$ for $i = \mathrm{A}, \mathrm{B}, \mathrm{C}, \mathrm{D}$. Accordingly, the volume average of the Piola stress becomes

$$\begin{aligned} \langle \boldsymbol{P} \rangle &= \frac{1}{\mathscr{V}_0} \int_{\partial \mathcal{B}_0} \boldsymbol{t}_0^{\mathrm{p}} \otimes \boldsymbol{X} \, \mathrm{d}A \\ &= \frac{1}{\mathscr{V}_0} \int_{\partial \mathcal{B}_0} [{}^{\mathrm{M}}\boldsymbol{P} \cdot \boldsymbol{N}] \otimes \boldsymbol{X} \, \mathrm{d}A + \frac{1}{\mathscr{V}_0} \sum_{i=\mathrm{A,B,C,D}} \boldsymbol{\zeta}^i \otimes \boldsymbol{X}^i \, \delta A^i \\ &= {}^{\mathrm{M}}\boldsymbol{P} + \frac{1}{\mathscr{V}_0} \left\{ \begin{bmatrix} \zeta_x^{\mathrm{A}} \\ \zeta_y^{\mathrm{A}} \\ \zeta_z^{\mathrm{A}} \end{bmatrix} \otimes \begin{bmatrix} 0 \\ 0 \\ 0 \end{bmatrix} + \begin{bmatrix} \zeta_x^{\mathrm{B}} \\ 0 \\ 0 \end{bmatrix} \otimes \begin{bmatrix} 0 \\ 0 \\ 1 \end{bmatrix} \right. \\ &\quad \left. + \begin{bmatrix} 0 \\ \zeta_y^{\mathrm{C}} \\ 0 \end{bmatrix} \otimes \begin{bmatrix} 1 \\ 0 \\ 0 \end{bmatrix} + \begin{bmatrix} 0 \\ 0 \\ \zeta_z^{\mathrm{D}} \end{bmatrix} \otimes \begin{bmatrix} 0 \\ 1 \\ 0 \end{bmatrix} \right\} \\ \delta A &= {}^{\mathrm{M}}\boldsymbol{P} + \frac{1}{\mathscr{V}_0} \begin{bmatrix} 0 & 0 & \zeta_x^{\mathrm{B}} \\ \zeta_y^{\mathrm{C}} & 0 & 0 \\ 0 & \zeta_z^{\mathrm{D}} & 0 \end{bmatrix} \delta A \, , \end{aligned}$$

from which the required conditions to suppress the spurious forces are derived

$$\zeta_x^{\mathrm{B}} \stackrel{!}{=} 0 \Longleftrightarrow \langle P_{xz} \rangle - {}^{\mathrm{M}}P_{xz} \stackrel{!}{=} 0, \quad \zeta_y^{\mathrm{C}} \stackrel{!}{=} 0 \Longleftrightarrow \langle P_{yx} \rangle - {}^{\mathrm{M}}P_{yx} \stackrel{!}{=} 0,$$
$$\zeta_z^{\mathrm{D}} \stackrel{!}{=} 0 \Longleftrightarrow \langle P_{zy} \rangle - {}^{\mathrm{M}}P_{zy} \stackrel{!}{=} 0$$

In order to satisfy these conditions, we prescribe and successively update the positions of the points B, C, D in x-, y-, and z-directions, respectively. Hence, the error vector reads $\boldsymbol{\Omega}({}^{\mathrm{M}}\boldsymbol{P}, \eta^{\mathrm{B}}, \eta^{\mathrm{C}}, \eta^{\mathrm{D}}) = [\langle \boldsymbol{F} \rangle - {}^{\mathrm{M}}\boldsymbol{F}, \zeta_x^{\mathrm{B}}, \zeta_y^{\mathrm{C}}, \zeta_z^{\mathrm{D}}]^{\mathrm{t}} =^{!} 0$ with $\eta^{\mathrm{B}}, \eta^{\mathrm{C}}$, and η^{D} being the prescribed displacements on points B–D. The consistent linearization of this nonlinear vector function reads

$$\begin{aligned} &\boldsymbol{\Omega}\left({}^{\mathrm{M}}\boldsymbol{P}_{n+1}, \eta_{n+1}^{\mathrm{B}}, \eta_{n+1}^{\mathrm{C}}, \eta_{n+1}^{\mathrm{D}}\right) = \boldsymbol{\Omega}\left({}^{\mathrm{M}}\boldsymbol{P}_n, \eta_n^{\mathrm{B}}, \eta_n^{\mathrm{C}}, \eta_n^{\mathrm{D}}\right) \\ &+ \frac{\partial \boldsymbol{\Omega}}{\partial {}^{\mathrm{M}}\boldsymbol{P}}|_n : \Delta {}^{\mathrm{M}}\boldsymbol{P}_n + \frac{\partial \boldsymbol{\Omega}}{\partial \eta^{\mathrm{B}}}|_n \Delta\eta_n^{\mathrm{B}} + \frac{\partial \boldsymbol{\Omega}}{\partial \eta^{\mathrm{C}}}|_n \Delta\eta_n^{\mathrm{C}} \\ &+ \frac{\partial \boldsymbol{\Omega}}{\partial \eta^{\mathrm{D}}}|_n \Delta\eta_n^{\mathrm{D}} \stackrel{!}{=} 0 \quad {}^{\mathrm{M}}\boldsymbol{P}_{n+1} = {}^{\mathrm{M}}\boldsymbol{P}_n + \Delta {}^{\mathrm{M}}\boldsymbol{P}_n, \\ &\eta_{n+1}^{\mathrm{B}} = \eta_n^{\mathrm{B}} + \Delta\eta_n^{\mathrm{B}}, \quad \eta_{n+1}^{\mathrm{C}} = \eta_n^{\mathrm{C}} + \Delta\eta_n^{\mathrm{C}}, \quad \eta_{n+1}^{\mathrm{D}} = \eta_n^{\mathrm{D}} + \Delta\eta_n^{\mathrm{D}} \end{aligned} \tag{38}$$

where n is the iteration step. Solving Eq. (38) yields the iterative increment $\Delta {}^{\mathrm{M}}\boldsymbol{P}_n$, $\Delta\eta_n^{\mathrm{B}}$, $\Delta\eta_n^{\mathrm{C}}$, and $\Delta\eta_n^{\mathrm{D}}$ and consequently ${}^{\mathrm{M}}\boldsymbol{P}_{n+1}$, η_{n+1}^{B}, η_{n+1}^{C}, and η_{n+1}^{D}.

Remark. Another well-known approach from the literature to implement constant traction boundary conditions in the context of the finite element analysis is given by Miehe and Koch [357], Miehe [462], Larsson and Runesson [232], and Fish and Fan [467]. This approach is based on employing a variational formulation and imposing the prescribed macrodeformation gradient via a Lagrange multiplier which is identified by the macro Piola stress. More precisely, the Lagrange multiplier is added as a new unknown to the problem and updated along with the unknown vector of displacements, see Appendix C for further details about this approach. We shall note (i) our proposed algorithm would become nearly identical to the algorithm given by Miehe if we insert the condition (36) into the residual vector in Eq. (26) and update the displacements, macro Piola stress, and the prescribed displacement at semi-Dirichlet boundary condition simultaneously, and (ii) the applicability of our proposed approach is not limited to the strain-driven computational homogenization but it is also capable of efficiently dealing with stress-driven

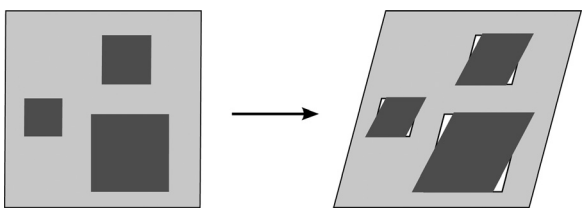

Fig. 10 The compatibility of the deformation field is violated under Sachs' assumption

homogenization. This is discussed in Appendix B. The algorithm proposed in Ref. [462] may be capable of coping with such problems but it is critically developed for the strain-driven homogenization framework. We have implemented the approach of in Ref. [462] too, and both approaches obviously lead to identical results. A thorough comparison of both approaches is out of the scope of this review and shall be studied in a separate contribution.

3.2.5 Sachs' Assumption. Sachs' assumption, also referred to as isostress condition, postulates that the entire domain of the RVE has the same stress ${}^{\mathrm{M}}\boldsymbol{P}$. In other words, both the inclusion and the matrix assume the same stress ${}^{\mathrm{M}}\boldsymbol{P}$, but not the same deformations. Clearly, this condition violates the compatibility of the deformation field. This is illustrated in Fig. 10. The apparent property of the material obtained under this condition and the classical Reuss' bound coincide in the linear regime.

Sachs' assumption allows to simplify the geometry of the RVE to two separate unit elements representing the inclusion and the matrix each possessing the same stress ${}^{\mathrm{M}}\boldsymbol{P}$. We begin the algorithm with ${}^{\mathrm{M}}\boldsymbol{P}=0$ and improve it iteratively until the volume average of the deformation gradient in the inclusion and the matrix reaches the macroscopic deformation gradient. That is, $\langle \boldsymbol{F}\rangle^{\mathrm{tot}} = {}^{\mathrm{M}}\boldsymbol{F}$ given $\langle \boldsymbol{F}\rangle^{\mathrm{tot}} = f\langle \boldsymbol{F}\rangle^{\mathrm{f}} + [1-f]\langle \boldsymbol{F}\rangle^{\mathrm{m}}$ with $\langle \boldsymbol{F}\rangle^{\mathrm{f}}$ and $\langle \boldsymbol{F}\rangle^{\mathrm{m}}$ being the volume averages of the deformation gradient in the inclusion and in the matrix, respectively.

Similar to TBC implementation, translational rigid body motions are eliminated by assigning Dirichlet boundary condition to points A = [0,0] and C = [0,0] in both directions (see Fig. 11). In order to remove rotational rigid body motions and also to ensure uniform distribution of the traction on the boundaries of the matrix and the inclusion, the locations of points B and D are prescribed using semi-Dirichlet boundary conditions and updated iteratively until no spurious force develops. We should, however, highlight that the prescribed displacements at point [1,0] in y-direction for the inclusion and the matrix are, in general, not identical.

The error vector takes the form $\boldsymbol{\Omega}({}^{\mathrm{M}}\boldsymbol{P}, \eta^{\mathrm{f}}, \eta^{\mathrm{m}}) = [\langle \boldsymbol{F}\rangle^{\mathrm{tot}} - {}^{\mathrm{M}}\boldsymbol{F}, \zeta_y^{\mathrm{B}}, \zeta_y^{\mathrm{D}}]^{\mathrm{t}} \overset{!}{=} 0$, with η^{f} and η^{m} being the prescribed displacements on points B and D, respectively, in y-direction. Spurious tractions on points B and D are denoted ζ_y^{B} and ζ_y^{D}, respectively. The consistent linearization of this vector function would be

$$\begin{aligned}
&\boldsymbol{\Omega}\left({}^{\mathrm{M}}\boldsymbol{P}_{n+1}, \eta^{\mathrm{f}}_{n+1}, \eta^{\mathrm{m}}_{n+1}\right) = \boldsymbol{\Omega}\left({}^{\mathrm{M}}\boldsymbol{P}_{n}, \eta^{\mathrm{f}}_{n}, \eta^{\mathrm{m}}_{n}\right) + \frac{\partial \boldsymbol{\Omega}}{\partial {}^{\mathrm{M}}\boldsymbol{P}}\Big|_n : \Delta {}^{\mathrm{M}}\boldsymbol{P}_n \\
&+ \frac{\partial \boldsymbol{\Omega}}{\partial \eta^{\mathrm{f}}}\Big|_n \Delta\eta^{\mathrm{f}}_n + \frac{\partial \boldsymbol{\Omega}}{\partial \eta^{\mathrm{m}}}\Big|_n \Delta\eta^{\mathrm{m}}_n \overset{!}{=} 0 \quad {}^{\mathrm{M}}\boldsymbol{P}_{n+1} = {}^{\mathrm{M}}\boldsymbol{P}_n + \Delta {}^{\mathrm{M}}\boldsymbol{P}_n, \\
&\eta^{\mathrm{f}}_{n+1} = \eta^{\mathrm{f}}_n + \Delta\eta^{\mathrm{f}}_n, \quad \eta^{\mathrm{m}}_{n+1} = \eta^{\mathrm{m}}_n + \Delta\eta^{\mathrm{m}}_n \,. \qquad (39)
\end{aligned}$$

Solving Eq. (39) yields the iterative increment $\Delta {}^{\mathrm{M}}\boldsymbol{P}_n$, $\Delta\eta^{\mathrm{f}}_n$, and $\Delta\eta^{\mathrm{m}}_n$ and consequently ${}^{\mathrm{M}}\boldsymbol{P}_{n+1}$, η^{f}_{n+1}, and η^{m}_{n+1}.

In passing, we mention that the presentation of Sachs' assumption in three dimensions is formally identical to the two-dimensional case, and formulating this problem in two dimensions here was carried out for simplicity.

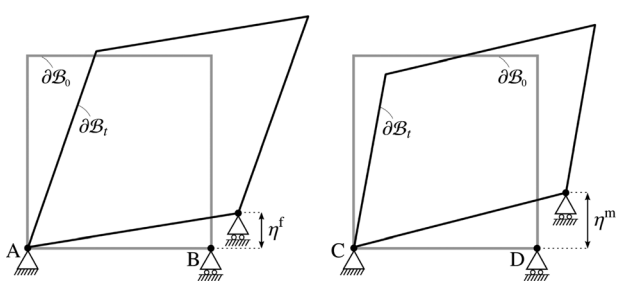

Fig. 11 The left and right unit elements represent the inclusion and the matrix, respectively

Sachs' assumption can be represented by a set of serial springs or a multiphase composite with parallel constituents which are aligned perpendicular to the direction of the applied force such that they carry the same force. This is illustrated in Fig. 12.

This system furnishes the most compliant possible response from two or more springs or constituents. Likewise, the overall response of the microstructure under this condition is always highly underestimated and referred to as Reuss' (Sachs') bound. The algorithm to implement Sachs' assumption is given as follows:

Algorithm 5: Sachs' assumption

input: ${}^{\mathrm{M}}\boldsymbol{F}$, **material parameters,** f
  ${}^{\mathrm{M}}\boldsymbol{P}=0$, $\eta^{\mathrm{f}}=0$, $\eta^{\mathrm{m}}=0$;
  create two separate unit elements representing the inclusion and the matrix;
  assign homogeneous Dirichlet and semi-Dirichlet BC to eliminate rigid body motion;
  while ${}^{\mathrm{M}}\boldsymbol{P}$, η^{f} *and* η^{m} *are not correct* **do**
    apply ${}^{\mathrm{M}}\boldsymbol{P}\cdot\boldsymbol{N}$ on Neumann part of the unit elements and update semi-Dirichlet BCs;
    solve the system of equations (27);
    evaluate $\langle \boldsymbol{F}\rangle^{\mathrm{tot}}$, $\langle \boldsymbol{P}\rangle^{\mathrm{f}}$ and $\langle \boldsymbol{P}\rangle^{\mathrm{m}}$;
    $\boldsymbol{\Omega}({}^{\mathrm{M}}\boldsymbol{P}, \eta^{\mathrm{f}}, \eta^{\mathrm{m}}) = [\langle \boldsymbol{F}\rangle^{\mathrm{tot}} - {}^{\mathrm{M}}\boldsymbol{F}, \langle P_{yx}\rangle^{\mathrm{f}} - {}^{\mathrm{M}}P_{yx}, \langle P_{yx}\rangle^{\mathrm{m}} - {}^{\mathrm{M}}P_{yx}]^{\mathrm{t}}$;
    if $||\boldsymbol{\Omega}|| <$ to/ **then**
      ${}^{\mathrm{M}}\boldsymbol{P}$, η^{f} and η^{m} are correct
    else
      Solve the system of equations (39);
      ${}^{\mathrm{M}}\boldsymbol{P} = {}^{\mathrm{M}}\boldsymbol{P} + \Delta {}^{\mathrm{M}}\boldsymbol{P}$;
      $\eta^{\mathrm{f}} = \eta^{\mathrm{f}} + \Delta\eta^{\mathrm{f}}$;
      $\eta^{\mathrm{m}} = \eta^{\mathrm{m}} + \Delta\eta^{\mathrm{m}}$
    end
  end
output: ${}^{\mathrm{M}}\boldsymbol{P}$

3.3 Numerical Examples of the Microproblem. The objective of this section is to illustrate the performance of the proposed scheme via a series of numerical examples. In doing so, a macro-deformation gradient is prescribed, and the algorithms in the previous sections are exploited to solve the microproblem. Both two-dimensional numerical examples corresponding to fiber-reinforced composites as well as three-dimensional microstructure representing particle-reinforced composites are studied.

First, the influence of the choice of the boundary conditions on the evolution of the macro Piola stress for various macrodeformation gradients is investigated. Both two- and three-dimensional microstructures are considered. This is then followed by studying the influence of different inclusion material parameters on the overall microresponse. Finally, the effects of number and distribution of the inclusions on the overall behavior of two microstructures are examined. More specifically, periodic and random microstructures are studied in detail.

The inclusion volume fraction is set to $f=25\%$ for all the sections. The samples are discretized by four- and eight-node bilinear finite elements in two- and three-dimensional problems, respectively. The samples and the associated finite element discretizations are shown in Fig. 13. The material parameters of the matrix are assumed as the shear modulus $\mu^{\mathrm{m}}=8.0$ and the Poisson's

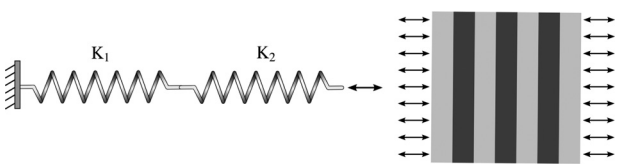

Fig. 12 Sachs' assumption representation via system of serial springs and multiphase composites

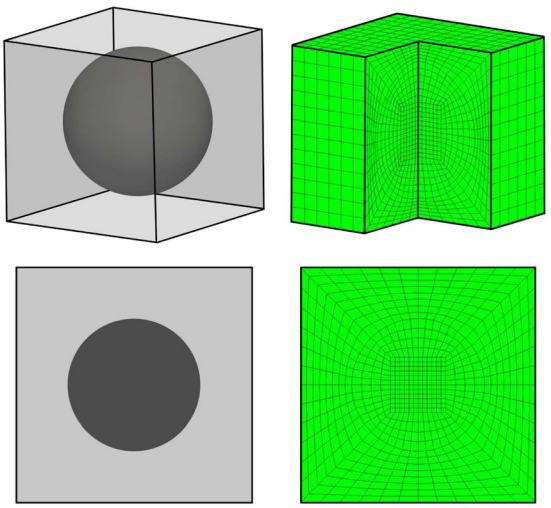

Fig. 13 Mesh qualities of the three- and two-dimensional samples

ratio $\nu^{\mathrm{m}} = 0.3$. The same Poisson's ratio is chosen for the inclusion material. Both inclusion and the matrix are assumed to behave according to the constitutive free energy density (10). The inclusion to matrix shear modulus ratio is denoted r. Perfect bonding between the matrix and the inclusion is assumed. All the examples are solved using our in-house finite element code in C++ syntax. The solution procedure is robust and for all examples shows asymptotically the quadratic rate of convergence associated with the Newton–Raphson scheme.

3.3.1 Illustration of Geometrically Nonlinear Overall Response of the Microstructure. The primary objective of this section is to illustrate the computational efficiency and robustness of the presented framework and to investigate the influence of the applied macrodeformation gradient on the average response of two- and three-dimensional microstructures under various conditions.

First, two macroscopic deformation gradients of uniaxial stretch in x-direction and simple-shear deformation in the xy-plane are imposed, and the influence of the choice of the boundary condition on the macroscopic Piola stress is examined. Next, the overall microstructural response with increasing the deformation for both deformation types is evaluated. The macrodeformation gradients for simple-shear and uniaxial stretch deformation types are of the form

$$ {}^{\mathrm{M}}\boldsymbol{F} = \begin{bmatrix} 1 & {}^{\mathrm{M}}F_{xy} \\ 0 & 1 \end{bmatrix} \quad \text{and} \quad {}^{\mathrm{M}}\boldsymbol{F} = \begin{bmatrix} {}^{\mathrm{M}}F_{xx} & 0 \\ 0 & 1 \end{bmatrix} $$

for two-dimensional problems and

$$ {}^{\mathrm{M}}\boldsymbol{F} = \begin{bmatrix} 1 & {}^{\mathrm{M}}F_{xy} & 0 \\ 0 & 1 & 0 \\ 0 & 0 & 1 \end{bmatrix} \quad \text{and} \quad {}^{\mathrm{M}}\boldsymbol{F} = \begin{bmatrix} {}^{\mathrm{M}}F_{xx} & 0 & 0 \\ 0 & 1 & 0 \\ 0 & 0 & 1 \end{bmatrix} $$

for three-dimensional problems, respectively, with ${}^{\mathrm{M}}F_{xx}$ and ${}^{\mathrm{M}}F_{xy}$ being the stretch and the shear. The stretch varies from the case of no stretch ${}^{\mathrm{M}}F_{xx} = 1.0$ up to ${}^{\mathrm{M}}F_{xx} = 3.5$ and the shear varies from the case of no shear ${}^{\mathrm{M}}F_{xy} = 0$ up to ${}^{\mathrm{M}}F_{xy} = 2.5$. Additionally, Taylor's and Sachs' assumptions are added to the remaining boundary conditions to solve the microproblem. For both sets of studies, inclusion material parameters of $r = 0.1$ and $r = 10$ are considered. Recall that $r = 0.1$ indicates that the inclusion is ten times more compliant to the matrix, and the extreme of $r \to 0$ leads to porous materials. Similarly, $r = 10$ indicates that the inclusion is ten times stiffer than the matrix and the limit of $r \to \infty$ recovers rigid inclusions in the matrix.

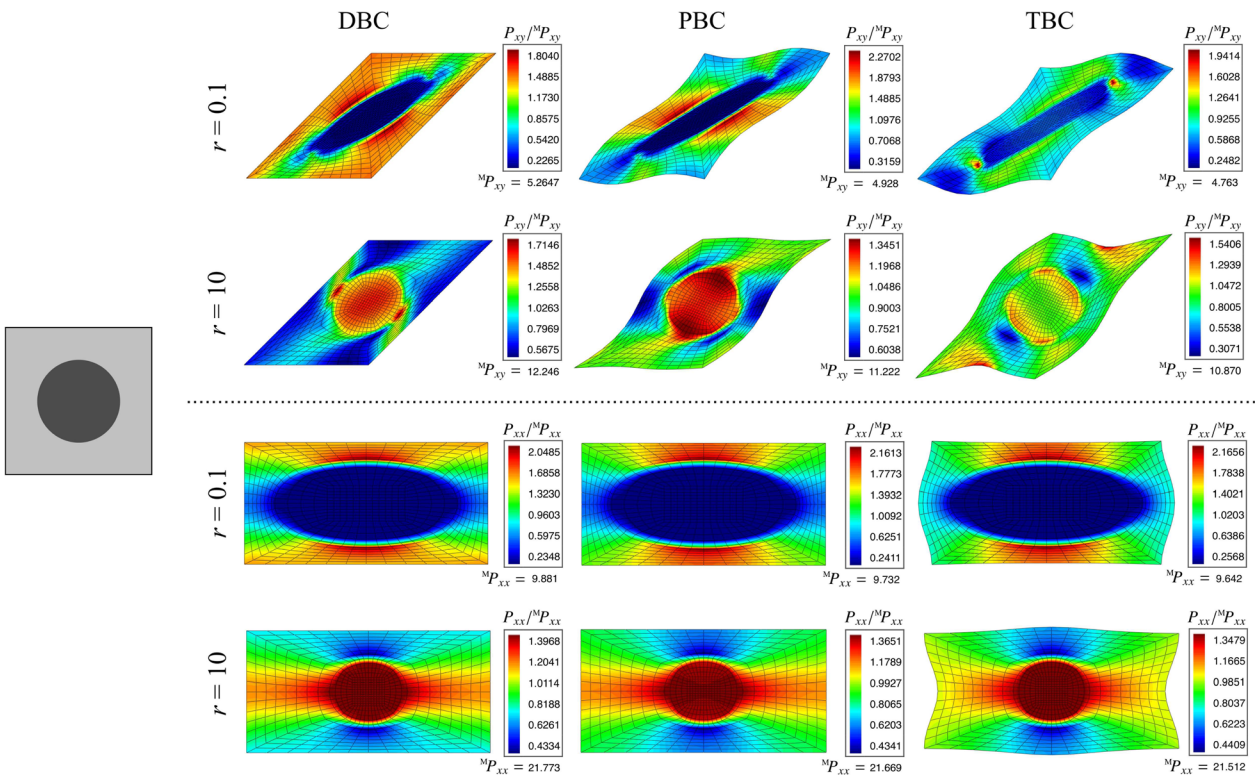

Fig. 14 Two-dimensional microstructure analysis using DBC, PBC, and TBC for $r = 0.1$ and $r = 10$. Top: simple-shear deformation in *xy*-plane. Distribution of the micro Piola stress (*xy*-component) normalized by its macro counterpart. Bottom: Uniaxial stretch in *x*-direction. Distribution of the micro Piola stress (*xx*-component) normalized by its macro counterpart.

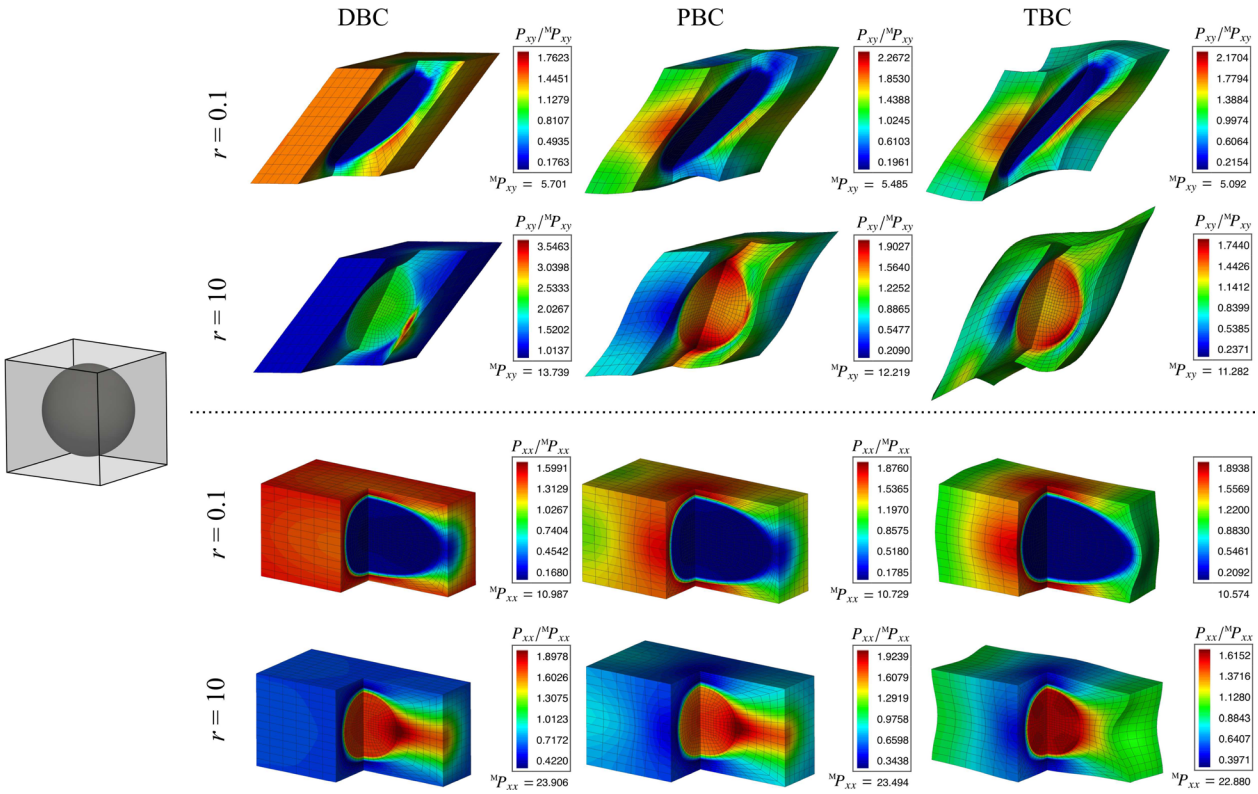

Fig. 15 Three-dimensional microstructure analysis using DBC, PBC, and TBC for $r = 0.1$ and $r = 10$. Top: simple-shear deformation in *xy*-plane. Distribution of the micro Piola stress (*xy*-component) normalized by its macro counterpart. Bottom: Uniaxial stretch in *x*-direction: Distribution of the micro Piola stress (*xx*-component) normalized by its macro counterpart.

Figure 14 illustrates the numerical results for the micro Piola stress distribution normalized by the corresponding macro Piola stress. The numerical simulations indicate that when 100% simple-shear deformation is applied on the two-dimensional microstructure and $r = 0.1$, the overall response using DBC overestimates the results from PBC by 6.83%. On the contrary, the response obtained using TBC underestimates the PBC results by 3.46%. When the inclusion is stronger than the matrix, the overall

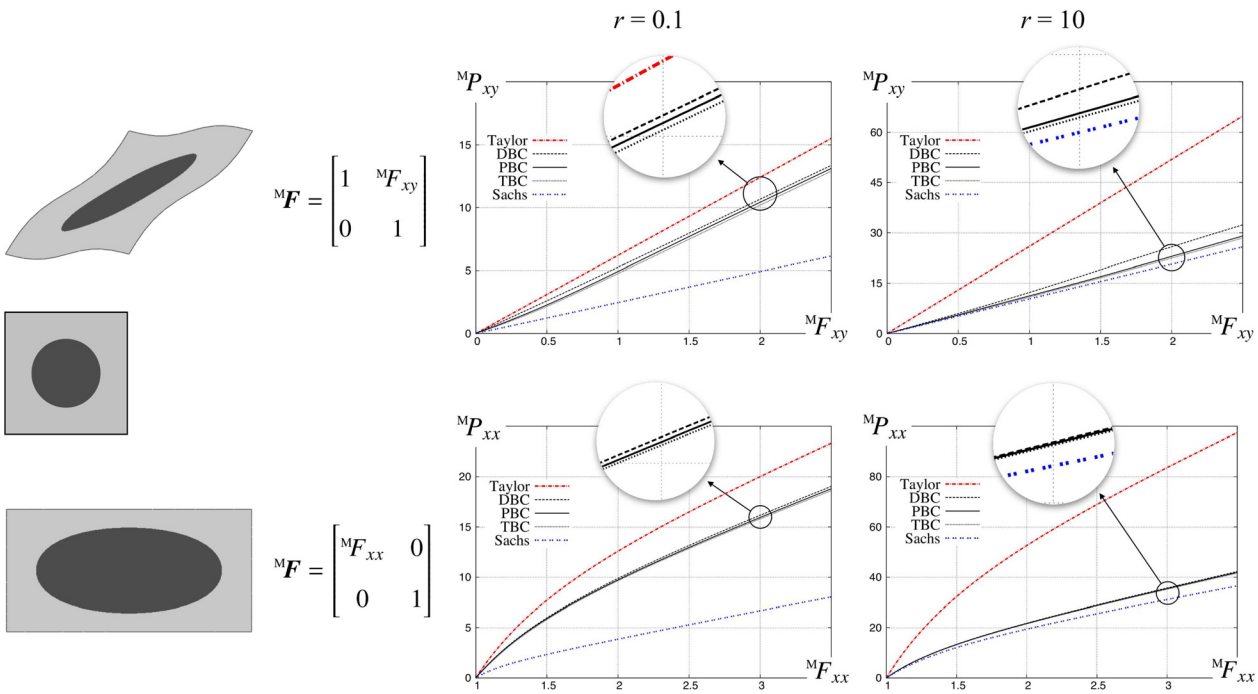

Fig. 16 Evolution of the macro Piola stress due to the increase of simple-shear deformation (top) and uniaxial stretch (bottom) for $r = 0.1$ (left) and $r = 10$ (right) for the two-dimensional microstructure. The depicted deformation modes correspond to the results of the PBC for 100% deformation with $r = 0.1$.

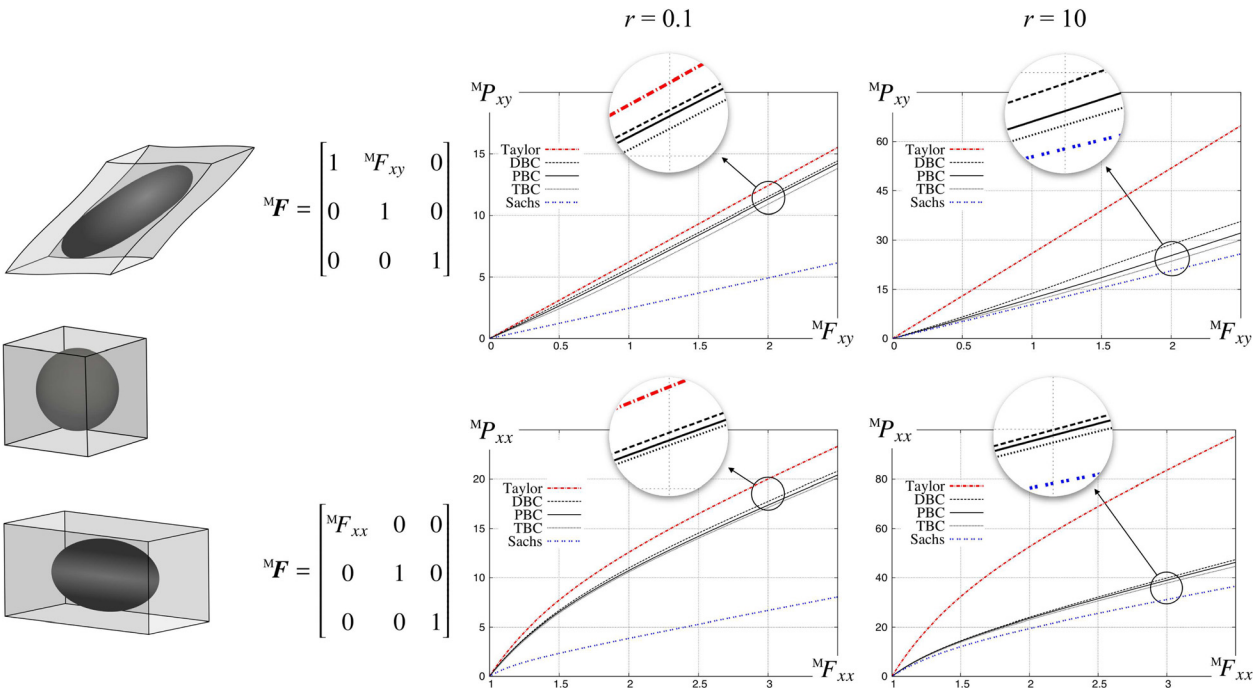

Fig. 17 Evolution of the macro Piola stress due to the increase of simple-shear deformation (top) and uniaxial stretch (bottom) for $r = 0.1$ (left) and $r = 10$ (right) for the three-dimensional microstructure. The depicted deformation modes correspond to the results of the PBC for 100% deformation with $r = 0.1$.

response under DBC overestimates the one under PBC with 9.12% while TBC underestimation remains almost the same, and it gives 3.23% underestimated response compared to the PBC. In contrast, when the microstructure undergoes 100% uniaxial stretch, utilizing different boundary conditions leads to much more similar responses compared to simple-shear test, for both cases of $r = 0.1$ and $r = 10$.

The same study is conducted for a three-dimensional microstructure, as shown in Fig. 15. It is verified that the gaps between the results of different boundary conditions are wider in all the cases compared to the two-dimensional microstructure. The only exception is found to be the 100% simple-shear deformation type where the inclusion is more compliant to the matrix. In this case, the DBC overestimates the results of the PBC by 3.93%, which is lower than its counterpart in the two-dimensional microstructure. Moreover, it is observed that the macro Piola stresses obtained for three-dimensional microstructure overestimate the ones obtained for two-dimensional microstructures for all the cases. Clearly, the choice of the boundary condition does not affect the microresponse when the inclusion and the matrix are identical.

Figures 16 and 17 depict the evolution of the macro Piola stress versus the prescribed macrodeformation gradient obtained using Taylor's assumption, DBC, PBC, TBC, and Sachs' assumption for two deformation types and different inclusion material parameters for two-dimensional and three-dimensional microstructures, respectively.

Regardless of the applied deformation type and deformation value, the results of DBC, PBC, and TBC are bounded by the Taylor's bound from the top and by the Sachs' bound from the bottom with DBC and TBC overestimating and underestimating the results of the PBC, respectively. However, the results from different boundary conditions tend more toward the Taylor's bound when the inclusion is more compliant to the matrix while they approach the results from the Sachs' bound when the inclusion is stiffer than the matrix. Note that different boundary conditions render more similar results for uniaxial stretch compared to simple-shear deformation for all the prescribed deformation values.

3.3.2 Influence of Material Parameters. This section details on the impact of the inclusion to matrix shear modulus ratio r on the overall response of the two-dimensional microstructure. The value of r varies from 0.0001 with inclusions resembling voids up to 10,000 with inclusions resembling rigid particles distributed in

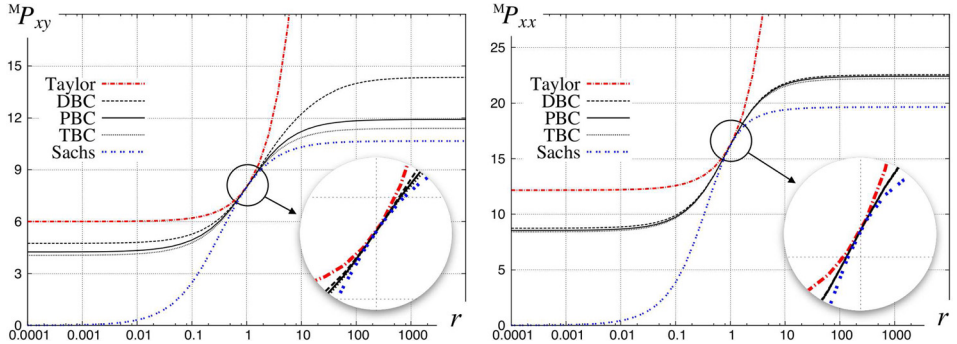

Fig. 18 Evolution of macro Piola stress due to the increase of f from 0.0001 to 10,000 when 100% simple-shear deformation (left) and uniaxial stretch (right) is imposed

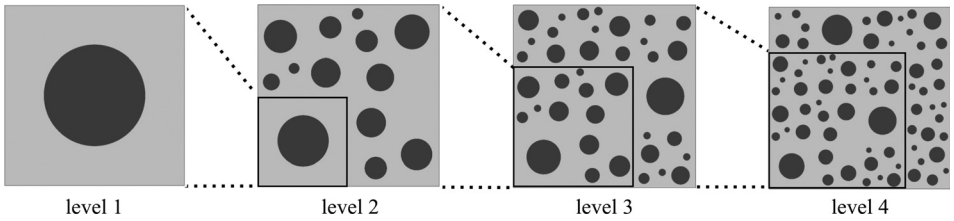

Fig. 19 Level *n* of the random microstructure consists of all the smaller microstructures and the information associated to size *n*. All the levels have the inclusion volume fraction of 25%.

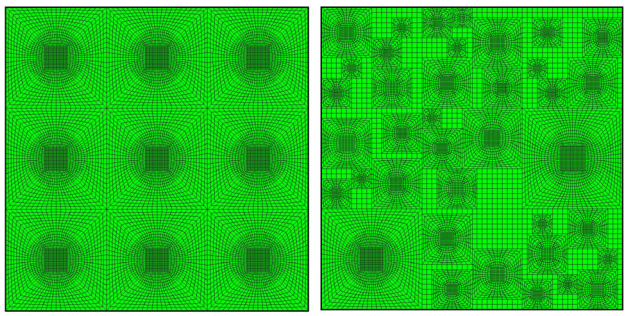

Fig. 20 Mesh qualities of periodic and random microstructures

the matrix. The microstructure undergoes 100% simple-shear deformation in *xy*-plane and 100% uniaxial stretch in *x*-direction. Figure 18 shows that regardless of the deformation type, increasing r from 0.0001 to 0.01 does not have a significant impact on the overall behavior for DBC, PBC, and TBC. However, increasing this value from 0.01 to 100 gives a rapid rise in the macroresponse. Further increase of this value does not result in a substantial variation of the average microresponse. But the results from the Taylor's bound increase indefinitely as the value of r increases, while, on the other hand, the results from the Sachs' bound approach zero as the composite resembles porous materials. Both behaviors are nonphysical and can be well explained by considering the microstructure as systems of parallel and serial springs as explained in Secs. 3.2.1 and 3.2.5. Again, the gaps between the results of the different boundary conditions are wider for simple-shear deformation compared to uniaxial stretch for both $r = 0.1$ and $r = 10$. Moreover, the results from DBC, TBC, and PBC always lie between the two bounds where DBC overestimates and TBC underestimates the PBC. Numerical results also confirm that the results from different boundary conditions are closer to Taylor's bound for $r < 1$ and tend more toward the Sachs' bound for $r > 1$.

3.3.3 Influence of the Number of Inclusions. A common assumption in computational homogenization is that the inclusions are uniformly distributed in the material which is often a simplification of real composites. Heterogeneous materials usually have a nonperiodic or spatially random microstructural composition. Obviously, variation of the inclusion distribution in the microstructure considerably affects the overall response of the composite. This section aims to highlight the influence of different morphologies of the microstructures on the macroresponse of the material. The macro Piola stress for various microstructures with identical inclusion volume fraction of 25% but different number of inclusions for both periodic and random distributions is evaluated and compared. Periodic microstructures are modeled by circular inclusions of the same size distributed uniformly while random microstructures contain inclusions of different size spread nonuniformly such that inclusions do not overlap. Contacts of the inclusions with the borders of the microstructure are also avoided. The first level of the random microstructure is exactly the same as the first level of the periodic microstructure. That is, a unit cell with 25% inclusion volume fraction. Any higher level of random microstructure, for example, level n, is created such that it contains the information of all the lower level random microstructures, 1, …, $n-1$, and the information associated to the level n itself. This is schematically shown for the first four levels of random microstructure in Fig. 19.

Both types of microstructures are discretized by four-node bilinear finite elements. As an example, Fig. 20 depicts the mesh resolutions for periodic and random microstructures of level 3. The algorithm employed to generate finite element meshes for microstructures considered in this section is not described as it is out of the scope of the current contribution. See, for instance, Refs. [468–481] for details on different approaches to generate and deal with complex microstructures.

Note that in spite of increasing the number of inclusions inside the microstructure, the physical size of all the microstructures remains identical. This study is conducted for 1% and 25% uniaxial stretch in x-direction with $r = 0.1$ and $r = 10$. Both periodic

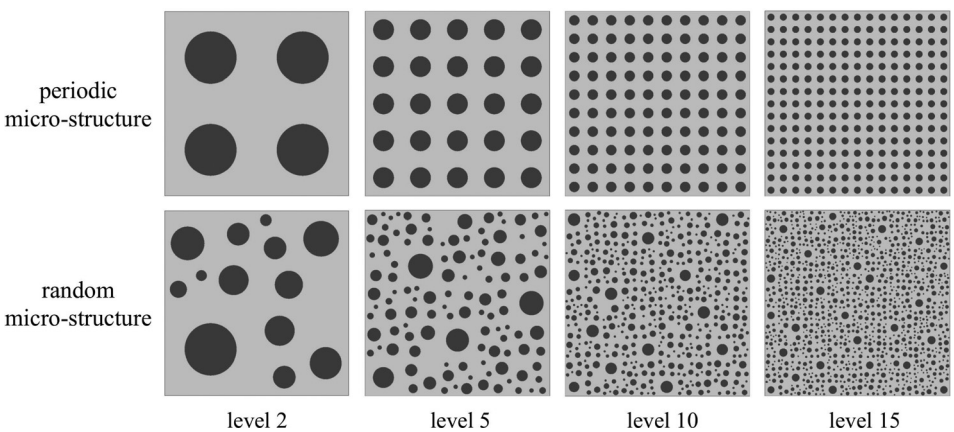

Fig. 21 Periodic and random microstructures. The inclusion volume fraction in all the microstructures is set to be $f = 25\%$.

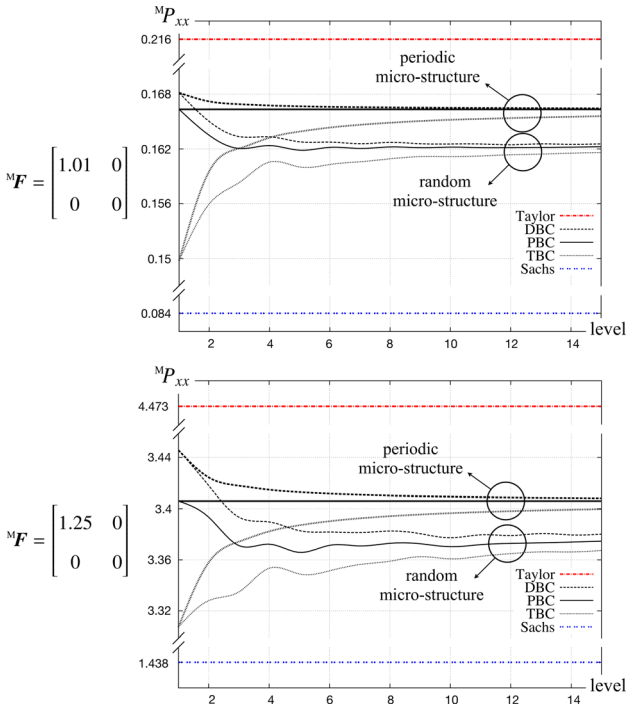

Fig. 22 Evolution of macrostress versus number of inclusions for 1% (top) and 25% (bottom) of uniaxial stretch and $r = 0.1$. Results of the Taylor's and Sachs' bounds are independent of the distribution pattern of the microstructure and only depend on the volume fraction. Choice of the boundary condition becomes less significant as the number of inclusions inside the RVE increases. Note that the results which are drawn by bolder lines correspond to periodic microstructures.

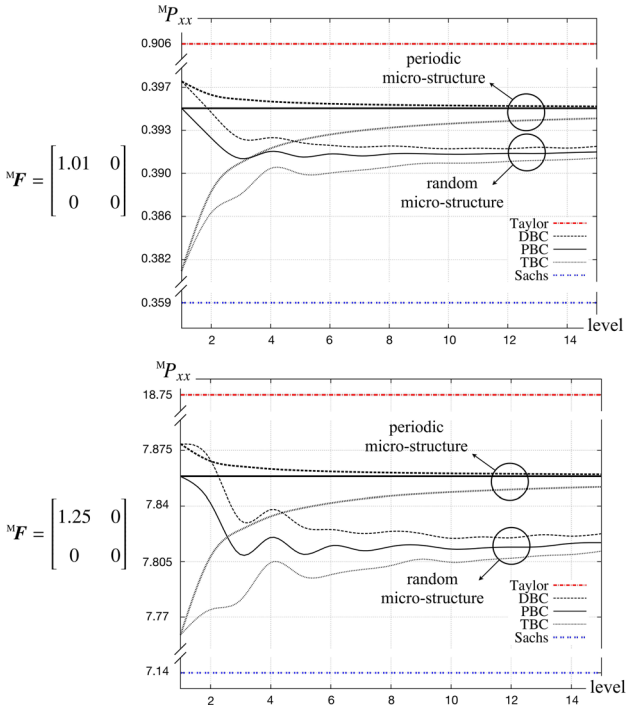

Fig. 23 Evolution of macrostress versus number of inclusions for 1% (top) and 25% (bottom) of uniaxial stretch and $r = 10$. Results of the Taylor's and Sachs' bounds are independent of the distribution pattern of the microstructure and only depend on the volume fraction. Choice of the boundary condition becomes less significant as the number of inclusions inside the RVE increases. Note that the results which are drawn by bolder lines correspond to periodic microstructures.

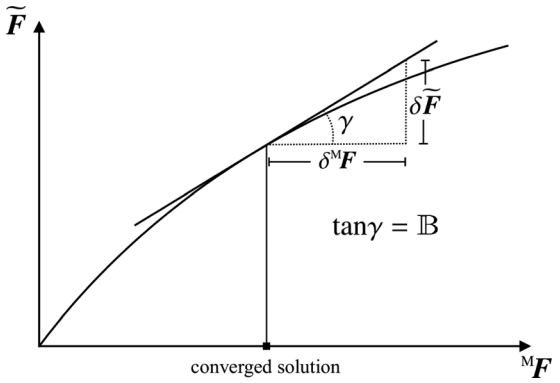

Fig. 24 The ratio $\delta\tilde{F}/\delta^{\mathrm{M}}F$ is evaluated through solving linear problems at the converged solution of the microproblem

and random microstructures from level 1 up to level 15 are considered (see Fig. 21).

Figures 22 and 23 show the evolution of the macro Piola stress with increasing number of inclusions both periodically and randomly for 1% (top) and 25% (bottom) of uniaxial stretch for $r = 0.1$ and $r = 10$, respectively. The numerical simulations illustrate that the results from the Taylor's and Sachs' assumptions are independent of the inclusion distribution pattern and solely depend on the inclusion volume fraction and provide a very rough estimate of the material response. In both types of the microstructures and deformations, the gap between the results from DBC, PBC, and TBC becomes smaller as the number of inclusions inside the matrix increases without exactly reaching each other. This trend is smoother for periodic microstructure compared to the case of random microstructure where minor fluctuations are observed. These fluctuations are however damped as the number of inclusions increases sufficiently.

3.4 Finite Element Formulation of the Macroproblem (FE^2). Solving the full two-scale problem involves satisfying the linear momentum not only at the microscale but also at the macroscale. Deriving the finite element formulation of the macroscale problem is nearly identical to the microscale problem and is not presented here for the sake of brevity. The fully discrete form of residual vector associated with the global node I at the macroscale reads

$$
{}^{\mathrm{M}}\boldsymbol{R}^{I}\left({}^{\mathrm{M}}\mathbf{d}\right) := \mathop{\mathsf{A}}_{\beta=1}^{\#\mathrm{be}} \int_{{}^{\mathrm{M}}\mathcal{B}_0^{\beta}} {}^{\mathrm{M}}\boldsymbol{P}.{}^{\mathrm{M}}\mathrm{Grad}N^{i}\ \mathrm{d}^{\mathrm{M}}V - \mathop{\mathsf{A}}_{\gamma=1}^{\#\mathrm{se}} \int_{{}^{\mathrm{M}}\partial\mathcal{B}_{0,\mathrm{N}}^{\gamma}} {}^{\mathrm{M}}\boldsymbol{t}_0^{\mathrm{p}} \cdot N^{i}\ \mathrm{d}^{\mathrm{M}}A - \mathop{\mathsf{A}}_{\beta=1}^{\#\mathrm{be}} \int_{{}^{\mathrm{M}}\mathcal{B}_0^{\beta}} {}^{\mathrm{M}}\boldsymbol{b}_0^{\mathrm{p}} \cdot N^{i}\ \mathrm{d}^{\mathrm{M}}V \overset{!}{=} \mathbf{0} \tag{40}
$$

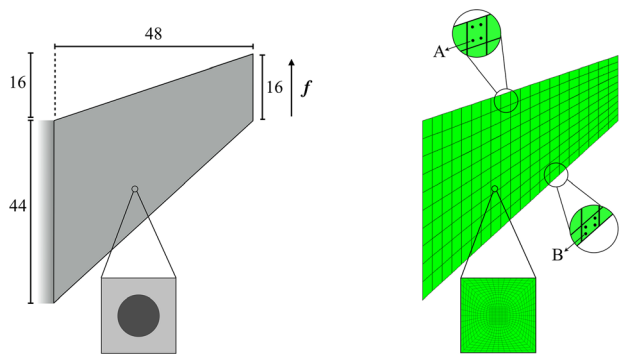

Fig. 25 Macro- and microscale samples and the associated finite element discretizations

The nodal residuals are arranged in a global residual vector ${}^{\mathrm{M}}\mathbf{R}$, and the fully discrete nonlinear system of governing equations reads

$$ {}^{\mathrm{M}}\mathbf{R} = {}^{\mathrm{M}}\mathbf{R}({}^{\mathrm{M}}\mathbf{d}) \stackrel{!}{=} 0 \tag{41} $$

with ${}^{\mathrm{M}}\mathbf{d}$ being the unknown global vector of macroscopic deformations. Similar to the microproblem procedure, the Newton–Raphson scheme is utilized to solve this nonlinear problem. The consistent linearization of the system of equations (41) yields

$$ {}^{\mathrm{M}}\mathbf{R}({}^{\mathrm{M}}\mathbf{d}_{n+1}) = {}^{\mathrm{M}}\mathbf{R}({}^{\mathrm{M}}\mathbf{d}_n) + {}^{\mathrm{M}}\mathbf{K} \cdot \Delta^{\mathrm{M}}\mathbf{d}_n \stackrel{!}{=} \mathbf{0} $$
$$ \text{with} \quad {}^{\mathrm{M}}\mathbf{K} = \frac{\partial^{\mathrm{M}}\mathbf{R}}{\partial^{\mathrm{M}}\mathbf{d}}\Big|_n, \quad {}^{\mathrm{M}}\mathbf{d}_{n+1} = {}^{\mathrm{M}}\mathbf{d}_n + \Delta^{\mathrm{M}}\mathbf{d}_n \tag{42} $$

where n is the iteration step and $\mathbf{K}$ is the assembled macroscopic tangent stiffness matrix of nodal stiffness

$$ {}^{\mathrm{M}}\boldsymbol{K}^{IJ} = \int_{{}^{\mathrm{M}}\mathcal{B}_0} \frac{\partial^{\mathrm{M}}\boldsymbol{P}}{\partial^{\mathrm{M}}\boldsymbol{F}} \bar{:} \left[{}^{\mathrm{M}}\mathrm{Grad}N^I \otimes {}^{\mathrm{M}}\mathrm{Grad}N^J\right] \mathrm{d}^{\mathrm{M}}V = \int_{{}^{\mathrm{M}}\mathcal{B}_0} {}^{\mathrm{M}}\mathbb{A} \bar{:} \left[{}^{\mathrm{M}}\mathrm{Grad}N^I \otimes {}^{\mathrm{M}}\mathrm{Grad}N^J\right] \mathrm{d}^{\mathrm{M}}V \tag{43} $$

Solving Eq. (42) yields the iterative increment $\Delta^{\mathrm{M}}\mathbf{d}_n$ and consequently ${}^{\mathrm{M}}\mathbf{d}_{n+1}$.

As discussed in Sec. 2.3, the macro Piola stress is calculated as the volume average of its micro counterpart. However, the macro Piola tangent is not the volume average of the micro Piola tangents, but computed as ${}^{\mathrm{M}}\mathbb{A} = \langle \mathbb{A} + \mathbb{A} : \mathbb{B} \rangle$. Recall that $\mathbb{B}$ is a fourth-order tensor that linearly maps the variation of the macrodeformation gradient $\delta^{\mathrm{M}}\boldsymbol{F}$ to the variation of the microdeformation gradient fluctuations $\delta\tilde{\boldsymbol{F}}$ as $\delta\tilde{\boldsymbol{F}} = \mathbb{B} : \delta^{\mathrm{M}}\boldsymbol{F}$. In this section, a systematic algorithm to calculate the tensor $\mathbb{B}$ and accordingly ${}^{\mathrm{M}}\mathbb{A}$ is given.

We determine $\mathbb{B}$ at the converged solution of the nonlinear microproblem and based on the linear relationship between $\delta^{\mathrm{M}}\boldsymbol{F}$ and $\delta\tilde{\boldsymbol{F}}$. Therefore, regardless of $\delta^{\mathrm{M}}\boldsymbol{F}$, the ratio $\delta\tilde{\boldsymbol{F}}/\delta^{\mathrm{M}}\boldsymbol{F}$ remains constant. That is, $\mathbb{B}$ is numerically evaluated by perturbing ${}^{\mathrm{M}}\boldsymbol{F}$ and calculating the resultant $\delta\tilde{\boldsymbol{F}}$ through solving a system of linear problems. This is schematically shown in Fig. 24. Detailed algorithm to compute $\mathbb{B}$ and ${}^{\mathrm{M}}\mathbb{A}$ is given as follows:

Algorithm 6: Macroscopic Piola tangent

input: ${}^{\mathrm{M}}\boldsymbol{F}$, **material parameters**
  solve the non-linear problem using Alg. 1,2,3,4 or 5 and store $\mathbb{A}$;
  for $r = 1 \rightarrow \mathrm{PD}$ **do**
    for $s = 1 \rightarrow \mathrm{PD}$ **do**
      $\delta^{\mathrm{M}}\boldsymbol{F}_{ij} = \delta_{ir}\delta_{js} \quad i,j = 1,\ldots,\mathrm{PD}$;
      solve the problem linearly for $\delta^{\mathrm{M}}\boldsymbol{F}$ at the converged solution;
      $\mathbb{B}_{ijrs} = \delta\tilde{\boldsymbol{F}}_{ij} \quad i,j = 1,\ldots,\mathrm{PD}$;
    end
  end
output: ${}^{\mathrm{M}}\mathbb{A} = \langle \mathbb{A} + \mathbb{A} : \mathbb{B} \rangle$

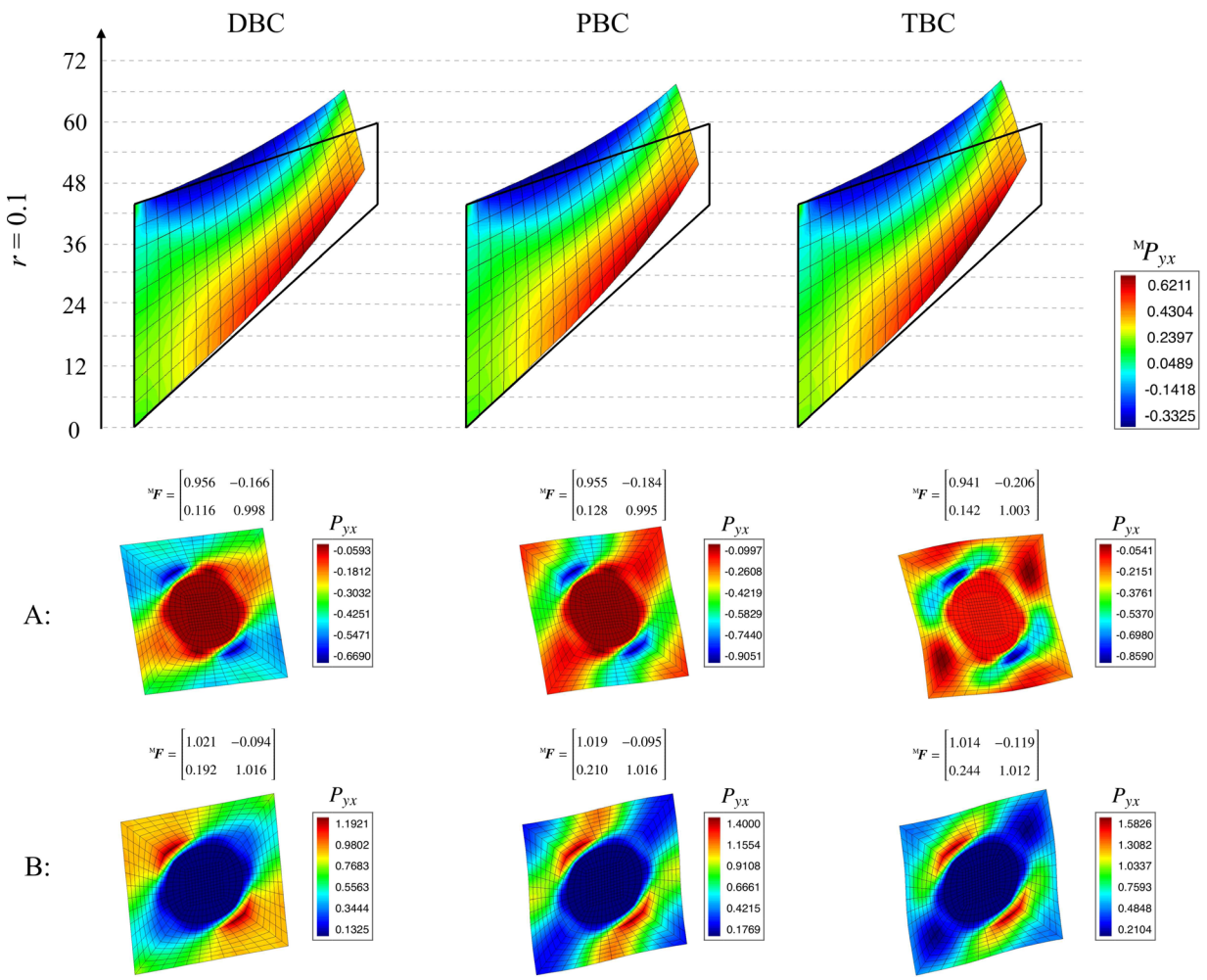

Fig. 26 Distribution of the *yx*-component of the stress within the macrostructure and its microstructures. The microproblem is solved through different boundary conditions and $r = 0.1$.

In the above algorithm, $\underline{\delta}$ denotes the Kronecker delta. Note that prescribing $\delta^{\mathrm{M}}\boldsymbol{F}$ or $\alpha\ \delta^{\mathrm{M}}\boldsymbol{F}$, with α being any real number, both render the same result. Here, we work with identities for simplicity. Otherwise, the coefficients should be properly normalized by α. See Refs. [363] and [414] for further discussions about computation of macro Piola tangent in the discrete formulation. Once ${}^{\mathrm{M}}\mathbb{A}$ is calculated, all the ingredients to perform the full FE^2 simulation are provided.

3.5 Numerical Examples of FE^2 for Various Microdeformation Assumptions. Equipped with the complete strain-driven computational homogenization framework for finite deformation analysis, full FE^2 simulations of a Cook's membrane problem made of uniformly arranged fiber-reinforced composite are performed under varying conditions. As depicted in Fig. 25, the macrosample is fixed along the left side and is loaded by the force vector of $\boldsymbol{f} = [0, 5]^{\mathrm{t}}$ along the right side.

The microstructure of the composite is a unit cell possessing the inclusion volume fraction of 25%. Similar to previous numerical examples, the material parameters of the matrix are assumed to be shear modulus $\mu^{\mathrm{m}} = 8.0$ and Poisson's ratio $\nu^{\mathrm{m}} = 0.3$. The simulations are carried out for two different inclusion material types of $r = 0.1$ and $r = 10$, along with three different boundary conditions, DBC, PBC, and TBC, to solve the boundary value problem at the microscale. In addition to the response of the macroproblem, the responses of the microproblems at two different points corresponding to the Gauss points located at the bottom left corner of two macroelements are presented. These points are labeled A and B and illustrated in Fig. 25. The figure also depicts the macro- and microsample and their mesh resolutions. The macrodomain and the microstructure are discretized by 200 and 720 bilinear finite elements, respectively. Figures 26 and 27 show the distribution of the yx-component of the stress within the macrostructure and the corresponding microstructures at points A and B for $r = 0.1$ and $r = 10$, respectively.

As anticipated, the highest macrostructural deformation is observed in the case that the microproblem is solved using TBC, and the inclusion is more compliant to the matrix. Obviously, the higher deformation of the composites under employing TBC leads to the evolution of slightly more stress concentrations within the macrostructure. The numerical results confirm that different boundary conditions render almost identical macrostructural deformations and stress distributions when the inclusion is stiffer than the matrix.

4 Summary

A comprehensive review of the first-order strain-driven computational homogenization scheme at finite deformations with primary focus on associated computational aspects is presented. First, the historical development of analytical and computational methods available in the literature to model heterogeneous materials is reviewed; their specific features are extensively discussed and in several cases compared. Next, the main emphasis is put on establishing a unifying first-order strain-driven computational homogenization framework based on the finite element method,

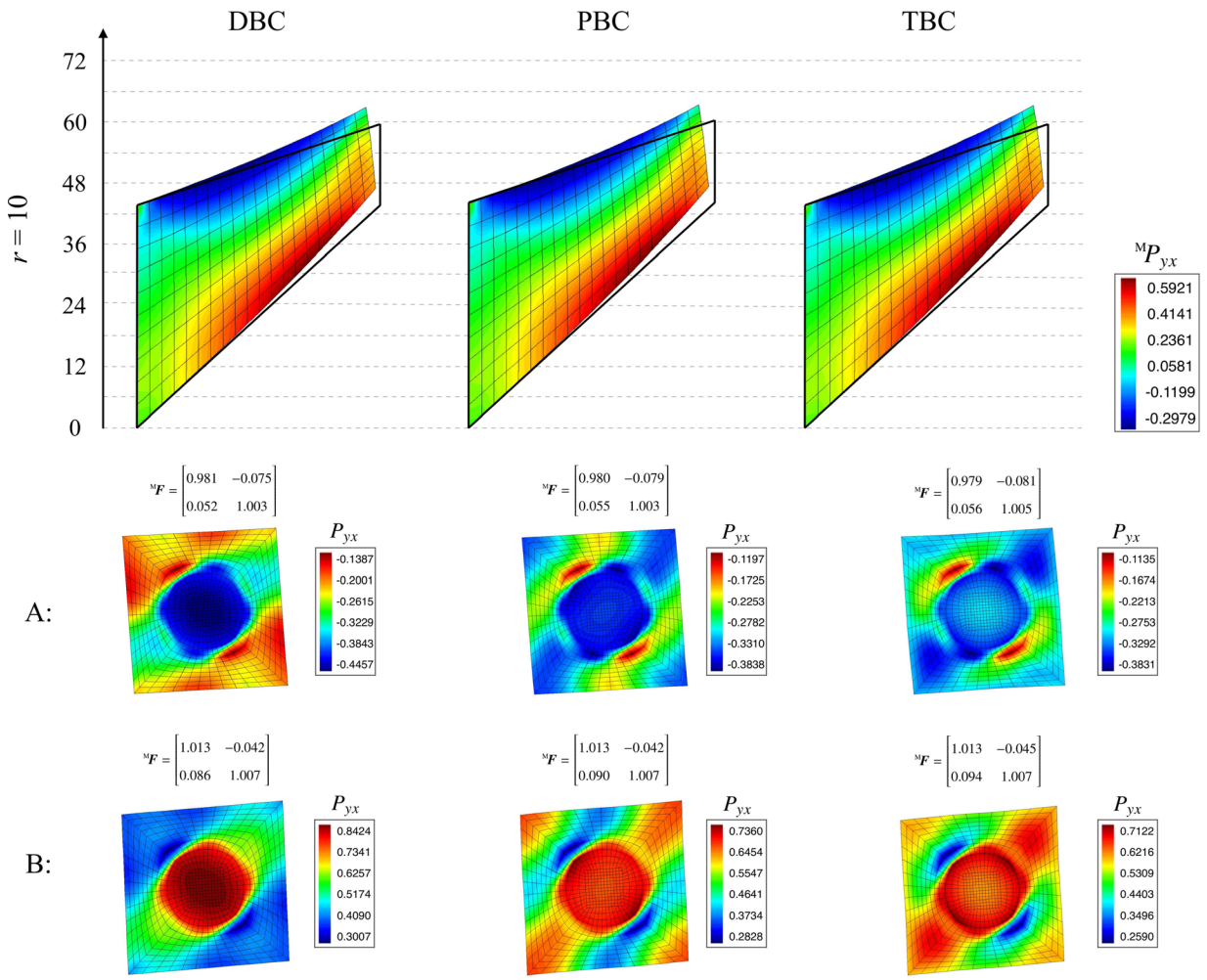

Fig. 27 Distribution of the *yx*-component of the stress within the macrostructure and its microstructures. The microproblem is solved through different boundary conditions and $r = 10$.

thereby the behavior of multiphase materials under large deformations is captured. More particularly, computational issues regarding the finite element implementation of different boundary conditions satisfying the Hill–Mandel condition to solve the microscale problem are introduced and explored. These conditions are linear DBCs, periodic displacement and antiperiodic TBCs, and finally, constant TBCs. Furthermore, the computational details to implement the nonlinear extensions of the Voigt's and Reuss' bounds known as the Taylor's and Sachs' assumptions are given. The efficiency of the proposed framework is demonstrated through presenting numerical examples for two- and three-dimensional microproblems under various conditions. In particular, the influence of the choice of the boundary condition, mismatch between the phases, amount of deformation, number of inclusions, and their distribution pattern on the overall response of the material is investigated. Finally, a concise and unified formulation to compute the macrotangent is given. Equipped with the presented framework, full FE^2 simulation of a Cook's membrane made of uniformly arranged fiber-reinforced composite is performed. The numerical results show that utilizing different boundary conditions at the microscale leads to qualitatively almost identical macroscopic response.

Finally, noting that homogenization is a rich, vast, and mature field, including all the relevant works in a single review paper is hardly possible. Nonetheless, we endeavored to selectively mention notable and pioneering contributions as well as recent developments revolving around this subject. The authors would welcome anyone's comment in the case that any major contribution is not included in this review.

Acknowledgment

The support of this work by the Cluster of Excellence "Engineering of Advanced Materials" at the University of Erlangen–Nuremberg, which is funded by the DFG within the framework of its "Excellence Initiative," is greatly appreciated.

Nomenclature

$\mathbb{A}$ = Piola tangent
A = assembly operator
$\mathcal{B}_t$ = spatial configuration
$\mathcal{B}_0$ = material configuration
$\mathbf{d}$ = global vector of deformation
DBC = displacement boundary conditions
Det = determinant operator
Div = divergence operator
f = inclusion volume fraction
$\boldsymbol{F}$ = deformation gradient
Grad = gradient operator
$\boldsymbol{I}$ = identity tensor
J = Jacobian of the deformation gradient
$\boldsymbol{K}$ = nodal stiffness tensor
$\mathbf{K}$ = assembled tangent stiffness matrix
$\boldsymbol{n}$ = spatial unit normal to boundary
N = shape functions of bulk and surface elements
$\boldsymbol{N}$ = material unit normal to boundary
$\boldsymbol{P}$ = Piola stress
PD = problem dimension
r = inclusion to matrix stiffness ratio
$\boldsymbol{R}$ = nodal residual vector
$\mathbf{R}$ = assembled residual vector
$\boldsymbol{t}_0^{\mathrm{p}}$ = prescribed traction on material configuration
TBC = traction boundary conditions
$\mathscr{V}_0$ = material bounded volume
$\boldsymbol{x}$ = spatial coordinates
$\boldsymbol{X}$ = material coordinates
$\delta\boldsymbol{\varphi}$ = test function
$\boldsymbol{\mu}, \boldsymbol{\lambda}$ = Lamé parameters
$\boldsymbol{\varphi}$ = deformation map
ψ = free energy density function
$\partial\mathcal{B}_t$ = boundary of spatial configuration
$\partial\mathcal{B}_0$ = boundary of material configuration
$\partial\mathcal{B}_{0,\mathrm{D}}$ = Dirichlet boundary of material configuration
$\partial\mathcal{B}_{0,\mathrm{N}}$ = Neumann boundary of material configuration
$\langle\rangle$ = volume averaging operator
$\{\tilde{\bullet}\}$ = fluctuation part of $\{\cdot\}$
$\{\bullet\}^{\mathrm{t}}$ = transpose of $\{\cdot\}$
$\{\bullet\}^{-\mathrm{t}}$ = transpose inverse of $\{\cdot\}$
$^{\mathrm{M}}\{\bullet\}$ = macro counterpart of micro $\{\cdot\}$
$\{\bullet\}^{-1}$ = inverse of $\{\cdot\}$
#be = number of bulk elements
#nbe = number of nodes per bulk element
#nse = number of nodes per surface element
#se = number of surface elements

Note:

- The term *Piola tangent* refers to the derivative of the Piola stress with respect to its work conjugate, the deformation gradient, and is a fourth-order constitutive tensor.
- The terms *macro* and *micro* are frequently used instead of macroscopic and microscopic.
- The term *inclusion* is used to refer to fibers in two-dimensional problems and to inclusions in three-dimensional problems.

Appendix A: Useful Lemmas and Relations

In this section, some useful lemmas and relations which are employed in this work are given. Furthermore, the intermediate steps and technicalities of some proofs are detailed. The extension of the relations and proofs presented in this section to account for surface energies is given in Ref. [252].

A.1 Lemma 1

$$\langle \boldsymbol{P} \rangle = \frac{1}{\mathscr{V}_0} \int_{\partial\mathcal{B}_0} \boldsymbol{t}_0 \otimes \boldsymbol{X} \, \mathrm{d}A$$

Proof of the Lemma 1

$$\langle \boldsymbol{P} \rangle = \frac{1}{\mathscr{V}_0} \int_{\mathcal{B}_0} \boldsymbol{P} \, \mathrm{d}V = \frac{1}{\mathscr{V}_0} \int_{\mathcal{B}_0} \boldsymbol{P} \cdot \boldsymbol{I} \, \mathrm{d}V = \frac{1}{\mathscr{V}_0} \int_{\mathcal{B}_0} \boldsymbol{P} \cdot \mathrm{Grad}\boldsymbol{X} \, \mathrm{d}V$$

using the relation $\boldsymbol{P} \cdot \mathrm{Grad}\boldsymbol{X} = \mathrm{Div}(\boldsymbol{P} \bar{\otimes} \boldsymbol{X}) - \mathrm{Div}\boldsymbol{P} \otimes \boldsymbol{X}$ and the fact that $\mathrm{Div}\boldsymbol{P} = 0$ inside $\mathcal{B}_0$

$$= \frac{1}{\mathscr{V}_0} \int_{\mathcal{B}_0} \mathrm{Div}(\boldsymbol{P} \bar{\otimes} \boldsymbol{X}) \, \mathrm{d}V$$

with the aid of the divergence theorem

$$= \frac{1}{\mathscr{V}_0} \int_{\partial\mathcal{B}_0} [\boldsymbol{P} \bar{\otimes} \boldsymbol{X}] \cdot \boldsymbol{N} \, \mathrm{d}A = \frac{1}{\mathscr{V}_0} \int_{\partial\mathcal{B}_0} \boldsymbol{P} \cdot \boldsymbol{N} \otimes \boldsymbol{X} \, \mathrm{d}A$$

from the balance equations $(6)_2$

$$= \frac{1}{\mathscr{V}_0} \int_{\partial\mathcal{B}_0} \boldsymbol{t}_0 \otimes \boldsymbol{X} \, \mathrm{d}A \qquad \square$$

The nonstandard product $\bar{\otimes}$ between a second-order tensor $\boldsymbol{A}$ and a vector $\boldsymbol{b}$ renders a third-order tensor $\mathrm{C} = \boldsymbol{A} \bar{\otimes} \boldsymbol{b}$ with its components $C_{ijk} = A_{ik} b_j$.

A.2 Lemma 2

$$\int_{\partial\mathcal{B}_0} \boldsymbol{N} \otimes \boldsymbol{X} \, \mathrm{d}A = \mathscr{V}_0 \boldsymbol{I}$$

Proof of the Lemma 2. Using the gradient theorem

$$\int_{\partial\mathcal{B}_0} \boldsymbol{N}\otimes\boldsymbol{X}\,\mathrm{d}A = \int_{\mathcal{B}_0} [\mathrm{Grad}\boldsymbol{X}]^{\mathrm{t}}\,\mathrm{d}V = \int_{\mathcal{B}_0} \boldsymbol{I}\,\mathrm{d}V = \boldsymbol{I}\int_{\mathcal{B}_0}\mathrm{d}V = \mathscr{V}_0\,\boldsymbol{I}$$

A.3 Hill's Lemma

$$\langle \boldsymbol{P}\colon \delta\boldsymbol{F}\rangle - {}^{\mathrm{M}}\boldsymbol{P}\colon \delta^{\mathrm{M}}\boldsymbol{F} = \frac{1}{\mathscr{V}_0}\int_{\partial\mathcal{B}_0}\left[\delta\boldsymbol{\varphi} - \delta^{\mathrm{M}}\boldsymbol{F}\cdot\boldsymbol{X}\right]\cdot\left[\boldsymbol{t}_0 - {}^{\mathrm{M}}\boldsymbol{P}\cdot\boldsymbol{N}\right]\mathrm{d}A \tag{A1}$$

In order to prove Hill's lemma, the right-hand side is expanded and manipulated until it eventually results in the left-hand side. Since only the equality operator is used, all the steps are also valid in the reverse order. First, we use $\boldsymbol{t}_0 = \boldsymbol{P}\cdot\boldsymbol{N}$ on $\partial\mathcal{B}_0$ and expand the right-hand side

$$\begin{aligned}
&\int_{\partial\mathcal{B}_0}\left[\delta\boldsymbol{\varphi} - \delta^{\mathrm{M}}\boldsymbol{F}\cdot\boldsymbol{X}\right]\cdot\left[\boldsymbol{t}_0 - {}^{\mathrm{M}}\boldsymbol{P}\cdot\boldsymbol{N}\right]\mathrm{d}A = \int_{\partial\mathcal{B}_0}\left[\delta\boldsymbol{\varphi} - \delta^{\mathrm{M}}\boldsymbol{F}\cdot\boldsymbol{X}\right]\cdot\left[\boldsymbol{P}\cdot\boldsymbol{N} - {}^{\mathrm{M}}\boldsymbol{P}\cdot\boldsymbol{N}\right]\mathrm{d}A\\
&= \int_{\partial\mathcal{B}_0}\delta\boldsymbol{\varphi}\cdot[\boldsymbol{P}\cdot\boldsymbol{N}]\,\mathrm{d}A - \int_{\partial\mathcal{B}_0}\delta\boldsymbol{\varphi}\cdot[{}^{\mathrm{M}}\boldsymbol{P}\cdot\boldsymbol{N}]\,\mathrm{d}A - \int_{\partial\mathcal{B}_0}[\delta^{\mathrm{M}}\boldsymbol{F}\cdot\boldsymbol{X}]\cdot\boldsymbol{P}\cdot\boldsymbol{N}\,\mathrm{d}A + \int_{\partial\mathcal{B}_0}[\delta^{\mathrm{M}}\boldsymbol{F}\cdot\boldsymbol{X}].{}^{\mathrm{M}}\boldsymbol{P}\cdot\boldsymbol{N}\,\mathrm{d}A\\
&= \int_{\partial\mathcal{B}_0}[\delta\boldsymbol{\varphi}\cdot\boldsymbol{P}]\cdot\boldsymbol{N}\,\mathrm{d}A - \int_{\partial\mathcal{B}_0}{}^{\mathrm{M}}\boldsymbol{P}\colon[\delta\boldsymbol{\varphi}\otimes\boldsymbol{N}]\,\mathrm{d}A - \int_{\partial\mathcal{B}_0}\delta^{\mathrm{M}}\boldsymbol{F}\colon[[\boldsymbol{P}\cdot\boldsymbol{N}]\otimes\boldsymbol{X}]\,\mathrm{d}A + \int_{\partial\mathcal{B}_0}[\delta^{\mathrm{M}}\boldsymbol{F}^{\mathrm{t}}.{}^{\mathrm{M}}\boldsymbol{P}]\colon[\boldsymbol{X}\otimes\boldsymbol{N}]\,\mathrm{d}A
\end{aligned}$$

Using the divergence theorem on the first integral and taking the constants out of the integral operators

$$= \int_{\mathcal{B}_0}\mathrm{Div}(\delta\boldsymbol{\varphi}\cdot\boldsymbol{P})\,\mathrm{d}V - {}^{\mathrm{M}}\boldsymbol{P}\colon\int_{\partial\mathcal{B}_0}\delta\boldsymbol{\varphi}\otimes\boldsymbol{N}\,\mathrm{d}A - \delta^{\mathrm{M}}\boldsymbol{F}\colon\int_{\partial\mathcal{B}_0}[[\boldsymbol{P}\cdot\boldsymbol{N}]\otimes\boldsymbol{X}]\,\mathrm{d}A + [\delta^{\mathrm{M}}\boldsymbol{F}^{\mathrm{t}}.{}^{\mathrm{M}}\boldsymbol{P}]\colon\int_{\partial\mathcal{B}_0}\boldsymbol{X}\otimes\boldsymbol{N}\,\mathrm{d}A$$

The first integral is simplified with the relation $\mathrm{Div}(\delta\boldsymbol{\varphi}\cdot\boldsymbol{P}) = \delta\boldsymbol{\varphi}\cdot\mathrm{Div}\boldsymbol{P} + \boldsymbol{P}\colon\mathrm{Grad}\delta\boldsymbol{\varphi} = \boldsymbol{P}\colon\delta\boldsymbol{F}$ since $\mathrm{Div}\boldsymbol{P} = 0$ due to balance of linear momentum. The second integral is rewritten using the gradient theorem as $\int_{\partial\mathcal{B}_0}\delta\boldsymbol{\varphi}\otimes\boldsymbol{N}\,\mathrm{d}A = \int_{\mathcal{B}_0}\mathrm{Grad}\delta\boldsymbol{\varphi}\,\mathrm{d}V$. The third integral is indeed the first term on the right-hand side of Lemma 1 since $\boldsymbol{t}_0 = \boldsymbol{P}\cdot\boldsymbol{N}$, and therefore, it can be expressed as $\int_{\partial\mathcal{B}_0}[[\boldsymbol{P}\cdot\boldsymbol{N}]\otimes\boldsymbol{X}]\,\mathrm{d}A = \mathscr{V}_0\,\langle\boldsymbol{P}\rangle$. The last integral simplifies using Lemma 2 in its transposed format as $\int_{\partial\mathcal{B}_0}\boldsymbol{X}\otimes\boldsymbol{N}\,\mathrm{d}A = \mathscr{V}_0\,\boldsymbol{I}$

$$\begin{aligned}
&= \int_{\mathcal{B}_0}\boldsymbol{P}\colon\delta\boldsymbol{F}\,\mathrm{d}V - {}^{\mathrm{M}}\boldsymbol{P}\colon\int_{\mathcal{B}_0}\mathrm{Grad}\delta\boldsymbol{\varphi}\,\mathrm{d}V - \delta^{\mathrm{M}}\boldsymbol{F}\colon\langle\boldsymbol{P}\rangle + [\delta^{\mathrm{M}}\boldsymbol{F}^{\mathrm{t}}.{}^{\mathrm{M}}\boldsymbol{P}]\colon[\mathscr{V}_0\,\boldsymbol{I}]\\
&= \mathscr{V}_0\,\langle\boldsymbol{P}\colon\delta\boldsymbol{F}\rangle - \mathscr{V}_0\,{}^{\mathrm{M}}\boldsymbol{P}\colon\langle\delta\boldsymbol{F}\rangle - \mathscr{V}_0\,\langle\boldsymbol{P}\rangle\colon\delta^{\mathrm{M}}\boldsymbol{F} + \mathscr{V}_0\,{}^{\mathrm{M}}\boldsymbol{P}\colon\delta^{\mathrm{M}}\boldsymbol{F}\,.
\end{aligned}$$

From the definitions of the average Piola stress (16) and the average deformation gradient (18)

$$\begin{aligned}
&= \mathscr{V}_0\,\langle\boldsymbol{P}\colon\delta\boldsymbol{F}\rangle - \mathscr{V}_0\,{}^{\mathrm{M}}\boldsymbol{P}\colon\delta^{\mathrm{M}}\boldsymbol{F} - \mathscr{V}_0\,{}^{\mathrm{M}}\boldsymbol{P}\colon\delta^{\mathrm{M}}\boldsymbol{F} + \mathscr{V}_0\,{}^{\mathrm{M}}\boldsymbol{P}\colon\delta^{\mathrm{M}}\boldsymbol{F}\\
&= \mathscr{V}_0\,\langle\boldsymbol{P}\colon\delta\boldsymbol{F}\rangle - \mathscr{V}_0\,{}^{\mathrm{M}}\boldsymbol{P}\colon\delta^{\mathrm{M}}\boldsymbol{F} = \mathscr{V}_0\left[\,\langle\boldsymbol{P}\colon\delta\boldsymbol{F}\rangle - {}^{\mathrm{M}}\boldsymbol{P}\colon\delta^{\mathrm{M}}\boldsymbol{F}\,\right].
\end{aligned}$$

A.4 Balance of Angular Momentum at the Macroscale. The global form of the balance of angular momentum at the microscale in the material configuration is

$$\int_{\partial\mathcal{B}_0}\boldsymbol{\varphi}\times\boldsymbol{t}\,\mathrm{d}V = 0 \quad\Longleftrightarrow\quad \int_{\partial\mathcal{B}_0}\boldsymbol{t}\otimes\boldsymbol{\varphi}\,\mathrm{d}A = \int_{\partial\mathcal{B}_0}\boldsymbol{\varphi}\otimes\boldsymbol{t}\,\mathrm{d}A \tag{A2}$$

A.4.1 Linear DBCs. In case of linear DBCs, substituting the material configuration position vector $\boldsymbol{\varphi} = {}^{\mathrm{M}}\boldsymbol{F}\cdot\boldsymbol{X}$ into Eq. $(A2)_2$ leads to

$$\begin{aligned}
&\int_{\partial\mathcal{B}_0}\boldsymbol{t}\otimes\boldsymbol{\varphi}\,\mathrm{d}A = \int_{\partial\mathcal{B}_0}\boldsymbol{\varphi}\otimes\boldsymbol{t}\,\mathrm{d}A\\
&\Longleftrightarrow \int_{\partial\mathcal{B}_0}\boldsymbol{t}\otimes{}^{\mathrm{M}}\boldsymbol{F}\cdot\boldsymbol{X}\,\mathrm{d}A = \int_{\partial\mathcal{B}_0}{}^{\mathrm{M}}\boldsymbol{F}\cdot\boldsymbol{X}\otimes\boldsymbol{t}\,\mathrm{d}A\\
&\Longleftrightarrow \int_{\partial\mathcal{B}_0}\boldsymbol{t}\otimes\boldsymbol{X}\,\mathrm{d}A.{}^{\mathrm{M}}\boldsymbol{F}^{\mathrm{t}} = {}^{\mathrm{M}}\boldsymbol{F}\cdot\int_{\partial\mathcal{B}_0}\boldsymbol{X}\otimes\boldsymbol{t}\,\mathrm{d}A\\
&\Longleftrightarrow {}^{\mathrm{M}}\boldsymbol{P}.{}^{\mathrm{M}}\boldsymbol{F}^{\mathrm{t}} = {}^{\mathrm{M}}\boldsymbol{F}.{}^{\mathrm{M}}\boldsymbol{P}^{\mathrm{t}}
\end{aligned}$$

A.4.2 Periodic Displacement and Antiperiodic TBCs. Taking into account the periodicity of the boundary displacement fluctuations leading to $\boldsymbol{\varphi}^+ = \boldsymbol{\varphi}^- + {}^{\mathrm{M}}\boldsymbol{F} \cdot [\boldsymbol{X}^+ - \boldsymbol{X}^-]$ and antiperiodicity of the boundary tractions, that is, $\boldsymbol{t}^+ = -\boldsymbol{t}^-$, Eq. (A2)$_2$ can be formulated as[5]

$$\begin{aligned}
&\int_{\partial\mathcal{B}_0} \boldsymbol{t} \otimes \boldsymbol{\varphi}\, \mathrm{d}A = \int_{\partial\mathcal{B}_0} \boldsymbol{\varphi} \otimes \boldsymbol{t}\, \mathrm{d}A \\
&\Longleftrightarrow \int_{\partial\mathcal{B}_0^+} \left[\boldsymbol{t} \otimes \boldsymbol{\varphi}^+ - \boldsymbol{t} \otimes \boldsymbol{\varphi}^-\right] \mathrm{d}A = \int_{\partial\mathcal{B}_0^+} \left[\boldsymbol{\varphi}^+ \otimes \boldsymbol{t} - \boldsymbol{\varphi}^- \otimes \boldsymbol{t}\right] \mathrm{d}A \\
&\Longleftrightarrow \int_{\partial\mathcal{B}_0^+} \left[\boldsymbol{t} \otimes \left[\boldsymbol{\varphi}^- + {}^{\mathrm{M}}\boldsymbol{F} \cdot [\boldsymbol{X}^+ - \boldsymbol{X}^-]\right] - \boldsymbol{t} \otimes \boldsymbol{\varphi}^-\right] \mathrm{d}A \\
&= \int_{\partial\mathcal{B}_0^+} \left[\left[\boldsymbol{\varphi}^- + {}^{\mathrm{M}}\boldsymbol{F} \cdot [\boldsymbol{X}^+ - \boldsymbol{X}^-] \otimes \boldsymbol{t}\right] - \boldsymbol{\varphi}^- \otimes \boldsymbol{t}\right] \mathrm{d}A \\
&\Longleftrightarrow \int_{\partial\mathcal{B}_0^+} \boldsymbol{t} \otimes {}^{\mathrm{M}}\boldsymbol{F} \cdot [\boldsymbol{X}^+ - \boldsymbol{X}^-]\, \mathrm{d}A = \int_{\partial\mathcal{B}_0^+} {}^{\mathrm{M}}\boldsymbol{F} \cdot [\boldsymbol{X}^+ - \boldsymbol{X}^-] \otimes \boldsymbol{t}\, \mathrm{d}A \\
&\Longleftrightarrow \int_{\partial\mathcal{B}_0^+} \boldsymbol{t} \otimes [\boldsymbol{X}^+ - \boldsymbol{X}^-]\, \mathrm{d}A \cdot {}^{\mathrm{M}}\boldsymbol{F}^{\mathrm{t}} = {}^{\mathrm{M}}\boldsymbol{F} \cdot \int_{\partial\mathcal{B}_0^+} [\boldsymbol{X}^+ - \boldsymbol{X}^-] \otimes \boldsymbol{t}\, \mathrm{d}A \\
&\Longleftrightarrow \int_{\partial\mathcal{B}_0} \boldsymbol{t} \otimes \boldsymbol{X}\, \mathrm{d}A \cdot {}^{\mathrm{M}}\boldsymbol{F}^{\mathrm{t}} = {}^{\mathrm{M}}\boldsymbol{F} \cdot \int_{\partial\mathcal{B}_0} \boldsymbol{X} \otimes \boldsymbol{t}\, \mathrm{d}A \\
&\Longleftrightarrow {}^{\mathrm{M}}\boldsymbol{P} \cdot {}^{\mathrm{M}}\boldsymbol{F}^{\mathrm{t}} = {}^{\mathrm{M}}\boldsymbol{F} \cdot {}^{\mathrm{M}}\boldsymbol{P}^{\mathrm{t}}
\end{aligned}$$

A.4.3 Constant TBCs. Substitution of constant TBCs definition, i.e., $\boldsymbol{t} = {}^{\mathrm{M}}\boldsymbol{P} \cdot \boldsymbol{N}$, into Eq. (A2)$_2$ renders

$$\begin{aligned}
&\int_{\partial\mathcal{B}_0} \boldsymbol{t} \otimes \boldsymbol{\varphi}\, \mathrm{d}A = \int_{\partial\mathcal{B}_0} \boldsymbol{\varphi} \otimes \boldsymbol{t}\, \mathrm{d}A \\
&\Longleftrightarrow \int_{\partial\mathcal{B}_0} {}^{\mathrm{M}}\boldsymbol{P} \cdot \boldsymbol{N} \otimes \boldsymbol{\varphi}\, \mathrm{d}A = \int_{\partial\mathcal{B}_0} \boldsymbol{\varphi} \otimes {}^{\mathrm{M}}\boldsymbol{P} \cdot \boldsymbol{N}\, \mathrm{d}A \\
&\Longleftrightarrow {}^{\mathrm{M}}\boldsymbol{P} \cdot \int_{\partial\mathcal{B}_0} \boldsymbol{N} \otimes \boldsymbol{\varphi}\, \mathrm{d}A = \int_{\partial\mathcal{B}_0} \boldsymbol{\varphi} \otimes \boldsymbol{N}\, \mathrm{d}A \cdot {}^{\mathrm{M}}\boldsymbol{P}^{\mathrm{t}} \\
&\Longleftrightarrow {}^{\mathrm{M}}\boldsymbol{P} \cdot {}^{\mathrm{M}}\boldsymbol{F}^{\mathrm{t}} = {}^{\mathrm{M}}\boldsymbol{F} \cdot {}^{\mathrm{M}}\boldsymbol{P}^{\mathrm{t}}
\end{aligned}$$

Appendix B: Stress-Driven Homogenization

Numerous problems which are of practical importance require the prescription of the macro Piola stress rather than the macrodeformation gradient [339,460,482]. In this section, we briefly present the computational algorithms to implement DBC, PBC, and TBC in the context of the stress-driven computational homogenization. Implementations of DBC and PBC in stress-driven homogenization are fairly similar to implementation of TBC in the strain-driven homogenization in the sense that iterations are required to reach the final solution. The algorithms start with an initial guess for the macrodeformation gradient. This guess is then iteratively updated until the volume average of the micro Piola stress reaches the macro Piola stress, that is, until $\langle \boldsymbol{P} \rangle = {}^{\mathrm{M}}\boldsymbol{P}$. Hence, the error vector takes the form

$$\boldsymbol{\Omega}({}^{\mathrm{M}}\boldsymbol{F}) = \left[\langle \boldsymbol{P} \rangle - {}^{\mathrm{M}}\boldsymbol{P}\right]^{\mathrm{t}} \stackrel{!}{=} \boldsymbol{0} \tag{B1}$$

The consistent linearization of this nonlinear vector function reads

$$\boldsymbol{\Omega}\left({}^{\mathrm{M}}\boldsymbol{F}_{n+1}\right) = \boldsymbol{\Omega}({}^{\mathrm{M}}\boldsymbol{F}_n) + \frac{\partial \boldsymbol{\Omega}}{\partial {}^{\mathrm{M}}\boldsymbol{F}}\Big|_n : \Delta^{\mathrm{M}}\boldsymbol{F}_n \stackrel{!}{=} 0 \quad {}^{\mathrm{M}}\boldsymbol{F}_{n+1} = {}^{\mathrm{M}}\boldsymbol{F}_n + \Delta^{\mathrm{M}}\boldsymbol{F}_n \tag{B2}$$

where n is the iteration step. Solving Eq. (B2) yields the iterative increment $\Delta^{\mathrm{M}}\boldsymbol{F}_n$ and consequently ${}^{\mathrm{M}}\boldsymbol{F}_{n+1}$. The algorithms to implement DBC and PBC in stress-driven homogenization are given as follows:

[5]Notations and symbols used here and detailed discussion on PBC are given in Sec. 3.2.3

Algorithm 7: Linear displacement boundary conditions (stress-driven)

input: ${}^{\mathrm{M}}\boldsymbol{P}$, material parameters
  ${}^{\mathrm{M}}\boldsymbol{F} = 0$;
  while ${}^{\mathrm{M}}\boldsymbol{F}$ *is not correct* **do**
    run Alg. 2;
    if $||\langle \boldsymbol{P} \rangle - {}^{\mathrm{M}}\boldsymbol{P}|| < \mathrm{tol}$ **then**
      ${}^{\mathrm{M}}\boldsymbol{F}$ is correct
    else
      solve the system of equations (B.2);
      ${}^{\mathrm{M}}\boldsymbol{F} = {}^{\mathrm{M}}\boldsymbol{F} + \Delta^{\mathrm{M}}\boldsymbol{F}$;
    end
  end
output: ${}^{\mathrm{M}}\boldsymbol{F}$

Algorithm 8: Periodic displacement and antiperiodic traction boundary conditions (stress-driven)

input: ${}^{\mathrm{M}}\boldsymbol{P}$, material parameters
  ${}^{\mathrm{M}}\boldsymbol{F} = 0$;
  while ${}^{\mathrm{M}}\boldsymbol{F}$ *is not correct* **do**
    run Alg. 3;
    if $||\langle \boldsymbol{P} \rangle - {}^{\mathrm{M}}\boldsymbol{P}|| < \mathrm{tol}$ **then**
      ${}^{\mathrm{M}}\boldsymbol{F}$ is correct
    else
      solve the system of equations (B.2);
      ${}^{\mathrm{M}}\boldsymbol{F} = {}^{\mathrm{M}}\boldsymbol{F} + \Delta^{\mathrm{M}}\boldsymbol{F}$;
    end
  end
output: ${}^{\mathrm{M}}\boldsymbol{F}$

Implementation of TBC for stress-driven homogenization is performed by prescribing the tractions, ${}^{\mathrm{M}}\boldsymbol{P} \cdot \boldsymbol{N}$, uniformly over the boundary of the microstructure. In order to deal with the rigid body motions, the configuration illustrated in Fig. 8 is employed. Obviously, no iteration for updating the macro Piola stress is required as it is known as the input of the problem. However, the displacement to be prescribed on semi-DBCs has to be updated until uniform distribution of the traction over the boundary of the microstructure is guaranteed. Hence, the condition (36) and the system of equations (37) reduce to

$$\Omega(\eta) = \zeta_y^{\mathrm{B}} \stackrel{!}{=} 0 \tag{B3}$$

and

$$\Omega(\eta_{n+1}) = \Omega(\eta_n) + \frac{\partial \Omega}{\eta}\Big|_n \Delta\eta_n \stackrel{!}{=} 0, \quad \eta_{n+1} = \eta_n + \Delta\eta_n \tag{B4}$$

respectively. The algorithm to implement TBC in stress-driven homogenization is given as follows:

Algorithm 9: Constant traction boundary conditions (stress-driven)

input: ${}^{\mathrm{M}}\boldsymbol{P}$, material parameters
  $\eta = 0$;
  assign homogeneous Dirichlet and semi-Dirichlet BC to eliminate rigid body motion;
  while η *is not correct* **do**
    apply ${}^{\mathrm{M}}\boldsymbol{P} \cdot \boldsymbol{N}$ on the Neumann part and update semi-Dirichlet BC;
    solve the system of equations (27);
    evaluate $\langle \boldsymbol{P} \rangle$;
    $\Omega(\eta) = \left[\langle P_{yx} \rangle - {}^{\mathrm{M}}P_{yx}\right]^{\mathrm{t}}$;
    if $||\Omega|| < \mathrm{tol}$ **then**
      η is correct
    else
      solve the system of equation (B4);
      $\eta = \eta + \Delta\eta$;
    end
  end
output: ${}^{\mathrm{M}}\boldsymbol{F}$

Appendix C: Implementing TBC in a Strain-Driven Homogenization Via a Lagrange Multiplier

The main objective of this section is to briefly address the approach given by Miehe [462] to implement constant TBCs via the Lagrange multiplier method. This methodology is essentially based on solving the incremental minimization problem of homogenization

$$ {}^{\mathrm{M}}W({}^{\mathrm{M}}\boldsymbol{F}) = \inf_{\mathbf{d}}{}^{\mathrm{M}}W(\mathbf{d}) \quad \text{with} \quad {}^{\mathrm{M}}W(\mathbf{d}) = \frac{1}{\mathscr{V}_0}\int_{\mathcal{B}_0} W(\boldsymbol{F};\boldsymbol{X})\,\mathrm{d}V \tag{C1}$$

with $\mathbf{d}$ being the unknown global vector of deformations, which minimizes the average incremental energy of the microstructure for a given macrodeformation gradient. In order to impose the constraint $\langle \boldsymbol{F}\rangle - {}^{\mathrm{M}}\boldsymbol{F} = 0$, the Lagrange multiplier method is used which yields the Lagrangian

$$\Omega(\mathbf{d},\boldsymbol{\lambda};{}^{\mathrm{M}}\boldsymbol{F}) = {}^{\mathrm{M}}W(\mathbf{d}) - \boldsymbol{\lambda}:\left[\langle \boldsymbol{F}\rangle - {}^{\mathrm{M}}\boldsymbol{F}\right] \tag{C2}$$

with $\boldsymbol{\lambda}$ being the Lagrange multiplier. It can be verified that

$$\frac{\partial\Omega\left(\mathbf{d},\boldsymbol{\lambda};{}^{\mathrm{M}}\boldsymbol{F}\right)}{\partial {}^{\mathrm{M}}\boldsymbol{F}} = {}^{\mathrm{M}}\boldsymbol{P} \qquad \text{with} \qquad {}^{\mathrm{M}}\boldsymbol{P} = \boldsymbol{\lambda} \tag{C3}$$

Next, the derivatives of the Lagrangian functional with respect to its variables are set to zero, and the following system of equations is obtained:

$$\begin{cases} \dfrac{\partial\Omega\left(\mathbf{d},{}^{\mathrm{M}}\boldsymbol{P};{}^{\mathrm{M}}\boldsymbol{F}\right)}{\partial\mathbf{d}} = 0 \quad \Rightarrow \quad \underbrace{\dfrac{\partial {}^{\mathrm{M}}W(\mathbf{d})}{\partial\mathbf{d}}}_{\mathbf{R}_{\mathrm{int}}} - \underbrace{{}^{\mathrm{M}}\boldsymbol{P}:\dfrac{\partial\langle\boldsymbol{F}\rangle}{\partial\mathbf{d}}}_{\mathbf{R}_{\mathrm{ext}}} = 0 \\ \dfrac{\partial\Omega\left(\mathbf{d},{}^{\mathrm{M}}\boldsymbol{P};{}^{\mathrm{M}}\boldsymbol{F}\right)}{\partial {}^{\mathrm{M}}\boldsymbol{P}} = 0 \quad \Rightarrow \quad {}^{\mathrm{M}}\boldsymbol{F} - \langle\boldsymbol{F}\rangle = 0 \end{cases} \tag{C4}$$

Linearization of this system of equation yields, in matrix format, the system of equations

$$\begin{bmatrix} \dfrac{\partial\mathbf{R}_{\mathrm{int}}}{\partial\mathbf{d}} & -\dfrac{\partial\mathbf{R}_{\mathrm{ext}}}{\partial {}^{\mathrm{M}}\boldsymbol{P}} \\ -\dfrac{\partial\langle\boldsymbol{F}\rangle}{\partial\mathbf{d}} & 0 \end{bmatrix} \begin{bmatrix} \Delta\mathbf{d} \\ \Delta {}^{\mathrm{M}}\boldsymbol{P} \end{bmatrix} = \begin{bmatrix} \mathbf{R}_{\mathrm{ext}} - \mathbf{R}_{\mathrm{int}} \\ \langle\boldsymbol{F}\rangle - {}^{\mathrm{M}}\boldsymbol{F} \end{bmatrix} \tag{C5}$$

The system of equations (C5) is not singular and can be solved without further modifications.

References

[1] Broughton, J. Q., Abraham, F. F., Bernstein, N., and Kaxiras, E., 1999, "Concurrent Coupling of Length Scales: Methodology and Application," Phys. Rev. B, **60**, pp. 2391–2403.

[2] Oden, J. T., Vemaganti, K., and Moës, N., 1999, "Hierarchical Modeling of Heterogeneous Solids," Comput. Methods Appl. Mech. Eng., **172**(1–4), pp. 3–25.

[3] Takano, N., Zako, M., and Ishizono, M., 2000, "Multi-Scale Computational Method for Elastic Bodies With Global and Local Heterogeneity," J. Comput.-Aided Mater. Des., **7**, pp. 111–132.

[4] Ladevèze, P., Loiseau, O., and Dureisseix, D., 2001, "A Micro–Macro and Parallel Computational Strategy for Highly Heterogeneous Structures," Int. J. Numer. Methods Eng., **52**(1–2), pp. 121–138.

[5] Ghosh, S., Lee, K., and Raghavan, P., 2001, "A Multi-Level Computational Model for Multi-Scale Damage Analysis in Composite and Porous Materials," Int. J. Solids Struct., **38**(14), pp. 2335–2385.

[6] Ibrahimbegović, A., and Markovič, D., 2003, "Strong Coupling Methods in Multi-Phase and Multi-Scale Modeling of Inelastic Behavior of Heterogeneous Structures," Comput. Methods Appl. Mech. Eng., **192**(28–30), pp. 3089–3107, 2003.

[7] Fish, J., and Chen, W., 2004, "Discrete-To-Continuum Bridging Based on Multigrid Principles," Comput. Methods Appl. Mech. Eng., **193**(17–20), pp. 1693–1711.

[8] Markovic, D., and Ibrahimbegovic, A., 2004, "On Micro–Macro Interface Conditions for Micro Scale Based FEM for Inelastic Behavior of Heterogeneous Materials," Comput. Methods Appl. Mech. Eng., **193**(48–51), pp. 5503–5523.

[9] Fish, J., and Yuan, Z., 2005, "Multiscale Enrichment Based on Partition of Unity," Int. J. Numer. Methods Eng., **62**(10), pp. 1341–1359.

[10] Fish, J., 2006, "Bridging the Scales in Nano Engineering and Science," J. Nanopart. Res., **8**(5), pp. 577–594.

[11] Ghosh, S., Bai, J., and Raghavan, P., 2007, "Concurrent Multi-Level Model for Damage Evolution in Microstructurally Debonding Composites," Mech. Mater. **39**(3), pp. 241–266.

[12] Hund, A., and Ramm, E., 2007, "Locality Constraints Within Multiscale Model for Non-Linear Material Behaviour," Int. J. Numer. Methods Eng., **70**(13), pp. 1613–1632.

[13] Mobasher Amini, A., Dureisseix, D., and Cartraud, P., 2009, "Multi-Scale Domain Decomposition Method for Large-Scale Structural Analysis With a Zooming Technique: Application to Plate Assembly," Int. J. Numer. Methods Eng., **79**(4), pp. 417–443.

[14] Larsson, F., and Runesson, K., 2011, "On Two-Scale Adaptive FE Analysis of Micro-Heterogeneous Media With Seamless Scale-Bridging," Comput. Methods Appl. Mech. Eng., **200**(31–40), pp. 2662–2674.

[15] Temizer, İ., and Wriggers, P., 2011, "An Adaptive Multiscale Resolution Strategy for the Finite Deformation Analysis of Microheterogeneous Structures," Comput. Methods Appl. Mech. Eng., **200**(31–40), pp. 2639–2661.

[16] Lloberas-Valls, O., Rixen, D. J., Simone, A., and Sluys, L. J., 2012, "On Micro-To-Macro Connections in Domain Decomposition Multiscale Methods," Comput. Methods Appl. Mech. Eng., **225–228**, pp. 177–196.

[17] Zhang, H. W., Wu, J. K., and Lv, J., 2012, "A New Multiscale Computational Method for Elasto-Plastic Analysis of Heterogeneous Materials," Comput. Mech., **49**(2), pp. 149–169.

[18] Wellmann, C., and Wriggers, P., 2012, "A Two-Scale Model of Granular Materials," Comput. Methods Appl. Mech. Eng., **205–208**, pp. 46–58 (2012).

[19] Khoei, A. R., Jahanbakhshi, F., and Aramoon, A., 2015, "A Concurrent Multi-Scale Technique in Modeling Heterogeneous FCC Nano-Crystalline Structures," Mech. Mater., **83**, pp. 40–65.

[20] Bitencourt, L. A. G., Jr., Manzoli, O. L., Prazeres, P. G. C., Rodrigues, E. A., and Bittencourt, T. N., 2015, "A Coupling Technique for Non-Matching Finite Element Meshes," Comput. Methods Appl. Mech. Eng., **290**, pp. 19–44.

[21] Tadmor, E. B., and Miller, R. E., 2011, *Modeling Materials: Continuum, Atomistic and Multiscale Techniques*, Cambridge University Press, New York.

[22] Lu, G., and Kaxiras, E., 2005, "Overview of Multiscale Simulations of Materials," *Handbook of Theoretical and Computational Nanotechnology*, Vol. 4, M. Rieth, and W. Schommers, eds., American Scientific Publishers, New York, Chap. 22.

[23] Sanchez-Palencia, E., 1974, "Comportements Local et Macroscopique d'un Type de Milieux Physiques Heterogenes," Int. J. Eng. Sci., **12**(4), pp. 331–351.

[24] Bensoussan, A., Lions, J. L., and Papanicolaou, G., 1978, *Asymptotic Analysis for Periodic Structures*, North-Holland, Amsterdam, The Netherlands.

[25] Sanchez-Palencia, E., 1980, *Non-Homogeneous Media and Vibration Theory*, Springer, Berlin, Heidelberg.

[26] Sanchez-Palencia, E., 1983, "Homogenization Method for the Study of Composite Media," *Asymptotic Analysis II* (Lecture Notes in Mathematics), Vol. 985, F. Verhulst, ed., Springer, Berlin, Heidelberg, pp. 192–214.

[27] Ene, H. I., 1983, "On Linear Thermoelasticity of Composite Materials," Int. J. Eng. Sci., **21**(5), pp. 443–448.

[28] Guedes, J. M., and Kikuchi, N., 1990, "Preprocessing and Postprocessing for Materials Based on the Homogenization Method With Adaptive Finite Element Methods," Comput. Methods Appl. Mech. Eng., **83**(2), pp. 143–198.

[29] Terada, K., and Kikuchi, N., 1996, "Microstructural Design of Composites Using the Homogenization Method and Digital Images," J. Soc. Mater. Sci., Jpn., **45**(2), pp. 65–72.

[30] Fish, J., Shek, K., Pandheeradi, M., and Shephard, M. S., 1997, "Computational Plasticity for Composite Structures Based on Mathematical Homogenization: Theory and Practice," Comput. Methods Appl. Mech. Eng., **148**(1–2), pp. 53–73.

[31] Fish, J., Yu, Q., and Shek, K., 1999, "Computational Damage Mechanics for Composite Materials Based on Mathematical Homogenization," Int. J. Numer. Methods Eng., **45**(11), pp. 1657–1679.

[32] Chung, P. W., Tamma, K. K., and Namburu, R. R., 2001, "Asymptotic Expansion Homogenization for Heterogeneous Media, Computational Issues and Applications," Composites Part A, **32**(9), pp. 1291–1301.

[33] Song, Y. S., and Youn, J. R., 2006, "Modeling of Effective Elastic Properties for Polymer Based Carbon Nanotube Composites," Polymer, **47**(6), pp. 1741–1748.

[34] Kalamkarov, A. L., Andrianov, I. V., and Danishevs'kyy, V. V., 2009, "Asymptotic Homogenization of Composite Materials and Structures," ASME Appl. Mech. Rev., **62**(3), p. 030802.

[35] Pinho-da Cruz, J., Oliveira, J. A., and Teixeira-Dias, F., 2009, "Asymptotic Homogenisation in Linear Elasticity. Part I: Mathematical Formulation and Finite Element Modelling," Comput. Mater. Sci., **45**(4), pp. 1073–1080.

[36] J-Dong, W., and Feng, M.-L., 2010, "Asymptotic Expansion Homogenization for Simulating Progressive Damage of 3D Braided Composites," Compos. Struct., **92**(4), pp. 873–882.

[37] Vel, S. S., and Goupee, A. J., 2010, "Multiscale Thermoelastic Analysis of Random Heterogeneous Materials. Part I: Microstructure Characterization and Homogenization of Material Properties," Comput. Mater. Sci., **48**(1), pp. 22–38.
[38] Angioni, S. L., Meo, M., and Foreman, A., 2011, "A Comparison of Homogenization Methods for 2-D Woven Composites," Composites Part B, **42**(2), pp. 181–189.
[39] Chatzigeorgiou, G., Efendiev, Y., and Lagoudas, D. C., 2011, "Homogenization of Aligned 'Fuzzy Fiber' Composites," Int. J. Solids Struct., **48**(19), pp. 2668–2680.
[40] Chatzigeorgiou, G., Efendiev, Y., Charalambakis, N., and Lagoudas, D. C., 2012, "Effective Thermoelastic Properties of Composites With Periodicity in Cylindrical Coordinates," Int. J. Solids Struct., **49**(18), pp. 2590–2603.
[41] Temizer, İ., 2012, "On the Asymptotic Expansion Treatment of Two-Scale Finite Thermoelasticity," Int. J. Eng. Sci., **53**, pp. 74–84.
[42] Kanouté, P., Boso, D. P., Chaboche, J. L., and Schrefler, B. A., 2009, "Multiscale Methods for Composites: A Review," Arch. Comput. Methods Eng., **16**(1), pp. 31–75.
[43] Charalambakis, N., 2010, "Homogenization Techniques and Micromechanics. A Survey and Perspectives," ASME Appl. Mech. Rev., **63**(3), p. 030803.
[44] Ortolano, J. M., Hernández, J. A., and Oliver, J., 2013, "A Comparative Study on Homogenization Strategies for Multi-Scale Analysis of Materials," Centre Internacional de Mètodes Numèrics en Enginyeria (CIMNE).
[45] Chen, W., and Fish, J., 2000, "A Dispersive Model for Wave Propagation in Periodic Heterogeneous Media Based on Homogenization With Multiple Spatial and Temporal Scales," ASME J. Appl. Mech., **68**, pp. 153–161.
[46] Yu, Q., and Fish, J., 2002, "Temporal Homogenization of Viscoelastic and Viscoplastic Solids Subjected to Locally Periodic Loading," Comput. Mech., **29**(3), pp. 199–211.
[47] Ladevèze, P., and Nouy, A., 2003, "On a Multiscale Computational Strategy With Time and Space Homogenization for Structural Mechanics," Comput. Methods Appl. Mech. Eng., **192**(28–30), pp. 3061–3087.
[48] Ladevèze, P., 2004, "Multiscale Modelling and Computational Strategies for Composites," Int. J. Numer. Methods Eng., **60**(1), pp. 233–253.
[49] Zhang, H. W., Zhang, S., Bi, J. Y., and Schrefler, B. A., 2007, "Thermo-Mechanical Analysis of Periodic Multiphase Materials by a Multiscale Asymptotic Homogenization Approach," Int. J. Numer. Methods Eng., **69**(1), pp. 87–113.
[50] Crouch, R., Oskay, C., and Clay, S., 2013, "Multiple Spatio-Temporal Scale Modeling of Composites Subjected to Cyclic Loading," Comput. Mech., **51**(1), pp. 93–107.
[51] Pham, K., Kouznetsova, V. G., and Geers, M. G. D., 2013, "Transient Computational Homogenization for Heterogeneous Materials Under Dynamic Excitation," J. Mech. Phys. Solids, **61**(11), pp. 2125–2146.
[52] Voigt, W., 1889, "Über die Beziehung zwischen den beiden Elastizitätskonstanten isotroper Körper," Wied. Ann., **38**, pp. 573–587.
[53] Reuss, A., 1929, "Berechnung der Fließgrenze von Mischkristallen auf Grund der Plastizitätsbedingung für Einkristalle," ZAMM—J. Appl. Math. Mech., **9**(1), pp. 49–58.
[54] Hill, R., 1952, "The Elastic Behaviour of a Crystalline Aggregate," Proc. Phys. Soc. Sect. A, **65**(4), pp. 349–354.
[55] Babuška, I., 1976, "Homogenization Approach in Engineering," *Computing Methods in Applied Sciences and Engineering* (Lecture Notes in Economics and Mathematical Systems), Vol. 134, R. Glowinski, and J. L. Lions, eds., Springer, Berlin, Heidelberg, pp. 137–153.
[56] Taylor, G. I., 1938, "Plastic Strain in Metals," J. Inst. Met., **62**, pp. 307–324.
[57] Sachs, G., 1928, "Zur Ableitung einer Fließbedingung," Z. Ver. Dtsch. Ing., **72**, pp. 734–736.
[58] Bishop, J. F. W., and Hill, R., 1951, "XLVI. A Theory of the Plastic Distortion of a Polycrystalline Aggregate Under Combined Stresses," London, Edinburgh, Dublin Philos. Mag. J. Sci., **42**(327), pp. 414–427.
[59] Leffers, T., 1979, "A Modified Sachs Approach to the Plastic Deformation of Polycrystals as a Realistic Alternative to the Taylor Model," *Strength of Metals and Alloys*, Vol. 2, P. Haasen, V. Gerold, and G. Kostorz, eds., Pergamon Press, Oxford, UK, pp. 769–774.
[60] Van Houtte, P., 1982, "On the Equivalence of the Relaxed Taylor Theory and the Bishop-Hill Theory for Partially Constrained Plastic Deformation of Crystals," Mater. Sci. Eng., **55**(1), pp. 69–77.
[61] Kocks, U. F., and Chandra, H., 1982, "Slip Geometry in Partially Constrained Deformation," Acta Metall., **30**(3), pp. 695–709.
[62] Van Houtte, P., Li, S., Seefeldt, M., and Delannay, L., 2005, "Deformation Texture Prediction: From the Taylor Model to the Advanced LAMEL Model," Int. J. Plast., **21**(3), pp. 589–624.
[63] Hashin, Z., and Shtrikman, S., 1963, "A Variational Approach to the Theory of the Elastic Behaviour of Multiphase Materials," J. Mech. Phys. Solids, **11**(2), pp. 127–140.
[64] Hashin, Z., and Shtrikman, S., 1962, "A Variational Approach to the Theory of the Effective Magnetic Permeability of Multiphase Materials," J. Appl. Phys., **33**(10), pp. 3125–3131.
[65] Walpole, L. J., 1966, "On Bounds for the Overall Elastic Moduli of Inhomogeneous Systems-II," J. Mech. Phys. Solids, **14**(5), pp. 289–301.
[66] Milton, G. W., and Kohn, R. V., 1988, "Variational Bounds on the Effective Moduli of Anisotropic Composites," J. Mech. Phys. Solids, **36**(6), pp. 597–629.
[67] Zimmerman, R. W., 1992, "Hashin–Shtrikman Bounds on the Poisson Ratio of a Composite Material," Mech. Res. Commun., **19**(6), pp. 563–569.
[68] Beran, M. J., and Molyneux, J., 1966, "Use of Classical Variational Principles to Determine Bounds for the Effective Bulk Modulus in Heterogeneous Media," Q. Appl. Math., **24**, pp. 107–118.
[69] Milton, G. W., and Phan-Thien, N., 1982, "New Bounds on Effective Elastic Moduli of Two-Component Materials," Proc. R. Soc. London: Ser. A, **380**(1779), pp. 305–331.
[70] Torquato, S., 1991, "Random Heterogeneous Media: Microstructure and Improved Bounds on Effective Propertie," ASME Appl. Mech. Rev., **44**(2), pp. 37–76.
[71] Rosen, B. W., and Hashin, Z., 1970, "Effective Thermal Expansion Coefficients and Specific Heats of Composite Materials," Int. J. Eng. Sci., **8**(2), pp. 157–173.
[72] Gibiansky, L. V., and Torquato, S., 1997, "Thermal Expansion of Isotropic Multiphase Composites and Polycrystals," J. Mech. Phys. Solids, **45**(7), pp. 1223–1252.
[73] Bisegna, P., and Luciano, R., 1996, "Variational Bounds for the Overall Properties of Piezoelectric Composites," J. Mech. Phys. Solids, **44**(4), pp. 583–602.
[74] Bisegna, P., and Luciano, R., 1997, "On Methods for Bounding the Overall Properties of Periodic Piezoelectric Fibrous Composites," J. Mech. Phys. Solids, **45**(8), pp. 1329–1356.
[75] Hori, M., and Nemat-Nasser, S., 1998, "Universal Bounds for Effective Piezoelectric Moduli," Mech. Mater., **30**(1), pp. 1–19.
[76] Ostoja-Starzewski, M., 2007, *Microstructural Randomness and Scaling in Mechanics of Materials*, Chapman and Hall/CRC, Boca Raton, FL.
[77] Nemat-Nasser, S., Yu, N., and Hori, M., 1993, "Bounds and Estimates of Overall Moduli of Composites With Periodic Microstructure," Mech. Mater., **15**(3), pp. 163–181.
[78] Bornert, M., Stolz, C., and Zaoui, A., 1996, "Morphologically Representative Pattern-Based Bounding in Elasticity," J. Mech. Phys. Solids, **44**(3), pp. 307–331.
[79] Li, J. Y., and Dunn, M. L., 2001, "Variational Bounds for the Effective Moduli of Heterogeneous Piezoelectric Solids," Philos. Mag. A, **81**(4), pp. 903–926.
[80] Eshelby, J. D., 1957, "The Determination of the Elastic Field of an Ellipsoidal Inclusion, and Related Problems," Proc. R. Soc. London A, **241**(1226), pp. 376–396.
[81] Rodin, G. J., 1996, "Eshelby's Inclusion Problem for Polygons and Polyhedra," J. Mech. Phys. Solids, **44**(12), pp. 1977–1995.
[82] Mura, T., 1997, "The Determination of the Elastic Field of a Polygonal Star Shaped Inclusion," Mech. Res. Commun., **24**(5), pp. 473–482.
[83] Markenscoff, X., 1997, "On the Shape of the Eshelby Inclusions," J. Elasticity, **49**(2), pp. 163–166.
[84] Lubarda, V. A., and Markenscoff, X., 1998, "On the Absence of Eshelby Property for Non-Ellipsoidal Inclusions," Int. J. Solids Struct., **35**(25), pp. 3405–3411.
[85] Kang, H., and Milton, G. W., 2008, "Solutions to the Pólya-Szegö Conjecture and the Weak Eshelby Conjecture," Arch. Ration. Mech. Anal., **188**(1), pp. 93–116.
[86] Liu, L. P., 2008, "Solutions to the Eshelby Conjectures," Proc. R. Soc. London A, **464**(2091), pp. 573–594.
[87] Zou, W., He, Q., Huang, M., and Zheng, Q., 2010, "Eshelby's Problem of Non-Elliptical Inclusions," J. Mech. Phys. Solids, **58**(3), pp. 346–372.
[88] Zhou, K., Hoh, H. J., Wang, X., Keer, L. M., Pang, J. H. L., Song, B., and Wang, Q. J., 2013, "A Review of Recent Works on Inclusions," Mech. Mater., **60**, pp. 144–158.
[89] Zohdi, T. I., and Wriggers, P., 2001, "Computational Micro–Macro Material Testing," Arch. Comput. Methods Eng., **8**(2), pp. 131–228.
[90] Mori, T., and Tanaka, K., 1973, "Average Stress in Matrix and Average Elastic Energy of Materials With Misfitting Inclusions," Acta Metall., **21**(5), pp. 571–574.
[91] Benveniste, Y., 1987, "A New Approach to the Application of Mori-Tanaka's Theory in Composite Materials," Mech. Mater., **6**(2), pp. 147–157.
[92] Luo, H. A., and Weng, G. J., 1987, "On Eshelby's Inclusion Problem in a Three-Phase Spherically Concentric Solid, and a Modification of Mori-Tanaka's Method," Mech. Mater., **6**(4), pp. 347–361.
[93] Kröner, E., 1958, "Berechnung der Elastischen Konstanten des Vielkristalls aus den Konstanten des Einkristalls," Z. Phys., **151**(4), pp. 504–518.
[94] Hill, R., 1965, "A Self-Consistent Mechanics of Composite Materials," J. Mech. Phys. Solids, **13**(4), pp. 213–222.
[95] Budiansky, B., 1965, "On the Elastic Moduli of Some Heterogeneous Materials," J. Mech. Phys. Solids, **13**(4), pp. 223–227.
[96] Walpole, L. J., 1969, "On the Overall Elastic Moduli of Composite Materials," J. Mech. Phys. Solids, **17**(4), pp. 235–251.
[97] Laws, N., 1973, "On the Thermostatics of Composite Materials," J. Mech. Phys. Solids, **21**(1), pp. 9–17.
[98] Willis, J. R., 1977, "Bounds and Self-Consistent Estimates for the Overall Properties of Anisotropic Composites," J. Mech. Phys. Solids, **25**(3), pp. 185–202.
[99] Kerner, E. H., 1956, "The Elastic and Thermo-Elastic Properties of Composite Media," Proc. Phys. Soc. Sect. B, **69**, pp. 808–813.
[100] Hermans, J. J., 1967, "The Elastic Properties of Fiber Reinforced Materials When the Fibers Are Aligned," Proc. K. Ned. Akad. Wet., **70**, pp. 1–9.
[101] Christensen, R. M., and Lo, K. H., 1979, "Solution for Effective Shear Properties in Three Phase Sphere and Cylinder Models," J. Mech. Phys. Solids, **27**(4), pp. 315–330.
[102] Huang, Y., Hu, K. X., Wei, X., and Chandra, H., 1994, "A Generalized Self-Consistent Mechanics Method for Composite Materials With Multiphase Inclusions," J. Mech. Phys. Solids, **42**(3), pp. 491–504.

[103] Chatzigeorgiou, G., Seidel, G. D., and Lagoudas, D. C., 2012, "Effective Mechanical Properties of "Fuzzy Fiber" Composites," Composites Part B, **43**(6), pp. 2577–2593.
[104] McLaughlin, R., 1977, "A Study of the Differential Scheme for Composite Materials," Int. J. Eng. Sci., **15**(4), pp. 237–244.
[105] Norris, A. N., 1985, "A Differential Scheme for the Effective Moduli of Composites," Mech. Mater., **4**(1), pp. 1–16.
[106] Pierard, O., Friebel, C., and Doghri, I., 2004, "Mean-Field Homogenization of Multi-Phase Thermo-Elastic Composites: A General Framework and Its Validation," Compos. Sci. Technol., **64**(10–11), pp. 1587–1603.
[107] Dunn, M. L., and Taya, M., 1993, "Micromechanics Predictions of the Effective Electroelastic Moduli of Piezoelectric Composites," Int. J. Solids Struct., **30**(2), pp. 161–175.
[108] Nemat-Nasser, S., Iwakuma, T., and Hejazi, M., 1982, "On Composites With Periodic Structure," Mech. Mater., **1**(3), pp. 239–267.
[109] Herve, E., and Zaoui, A., 1993, "N-Layered Inclusion-Based Micromechanical Modelling," Int. J. Eng. Sci., **31**(1), pp. 1–10.
[110] Huang, Y., and Hu, K. X., 1995, "A Generalized Self-Consistent Mechanics Method for Solids Containing Elliptical Inclusions," ASME J. Appl. Mech., **62**(3), pp. 566–572.
[111] Benveniste, Y., and Milton, G. W., 2010, "The Effective Medium and the Average Field Approximation Vis-à-Vis the Hashin–Shtrikman Bounds. I. The Self-Consistent Scheme in Matrix-Based Composites," J. Mech. Phys. Solids, **58**(3), pp. 1026–1038.
[112] Benveniste, Y., and Milton, G. W., 2010, "The Effective Medium and the Average Field Approximation Vis-à-Vis the Hashin–Shtrikman Bounds. II. The Generalized Self-Consistent Scheme in Matrix-Based Composites," J. Mech. Phys. Solids, **58**(7), pp. 1039–1056.
[113] Kanaun, S. K., and Levin, V., 2008, *Self-Consistent Methods for Composites-Vol.1: Static Problems*, Springer, Dordrecht, The Netherlands.
[114] Walpole, L. J., 1966, "On Bounds for the Overall Elastic Moduli of Inhomogeneous Systems-I," J. Mech. Phys. Solids, **14**(3), pp. 151–162.
[115] Weng, G. J., 1990, "The Theoretical Connection Between Mori-Tanaka's Theory and the Hashin–Shtrikman–Walpole Bounds," Int. J. Eng. Sci., **28**(11), pp. 1111–1120.
[116] Riccardi, A., and Montheillet, F., 1999, "A Generalized Self-Consistent Method for Solids Containing Randomly Oriented Spheroidal Inclusions," Acta Mech., **133**(1), pp. 39–56.
[117] Hill, R., 1964, "Theory of Mechanical Properties of Fibre-Strengthened Materials: I. Elastic Behaviour," J. Mech. Phys. Solids, **12**(4), pp. 199–212.
[118] Halpin, J. C., 1969, "Stiffness and Expansion Estimates for Oriented Short Fiber Composites," J. Compos. Mater., **3**, pp. 732–734.
[119] Halpin, J. C., and Kardos, J. L., "The Halpin-Tsai Equations: A Review," Polym. Eng. Sci., **16**, pp. 344–352.
[120] Hori, M., and Nemat-Nasser, S., 1993, "Double-Inclusion Model and Overall Moduli of Multi-Phase Composites," Mech. Mater., **14**(3), pp. 189–206.
[121] Hu, G. K., and Weng, G. J., 2000, "The Connections Between the Double-Inclusion Model and the Ponte Castaneda-Willis, Mori-Tanaka, and Kuster-Toksoz Models," Mech. Mater., **32**(8), pp. 495–503.
[122] Aboutajeddine, A., and Neale, K. W., 2005, "The Double-Inclusion Model: A New Formulation and New Estimates," Mech. Mater., **37**(2–3), pp. 331–341.
[123] Tucker, C. L., and Liang, E., 1999, "Stiffness Predictions for Unidirectional Short-Fiber Composites: Review and Evaluation," Compos. Sci. Technol., **59**(5), pp. 655–671.
[124] Hill, R., 1972, "On Constitutive Macro-Variables for Heterogeneous Solids at Finite Strain," Proc. R. Soc. London A, **326**(1565), pp. 131–147.
[125] Ogden, R. W., 1974, "On the Overall Moduli of Non-Linear Elastic Composite Materials," J. Mech. Phys. Solids, **22**(6), pp. 541–553.
[126] Willis, J. R., 1986, "Variational Estimates for the Overall Response of an Inhomogeneous Nonlinear Dielectric," *Homogenization and Effective Moduli of Materials and Media* (The IMA Volumes in Mathematics and Its Applications), Vol. 1, J. L. Ericksen, D. Kinderlehrer, R. Kohn, and J.-L. Lions, eds., Springer, New York, pp. 247–263.
[127] Ponte Castañeda, P., and Willis, J. R., 1988, "On the Overall Properties of Nonlinearly Viscous Composites," Proc. R. Soc. London A, **416**(1850), pp. 217–244.
[128] Suquet, P. M., 1993, "Overall Potentials and Extremal Surfaces of Power Law or Ideally Plastic Composites," J. Mech. Phys. Solids, **41**(6), pp. 981–1002.
[129] Olson, T., 1994, "Improvements on Taylor's Upper Bound for Rigid-Plastic Composites," Mater. Sci. Eng. A, **175**(1–2), pp. 15–20.
[130] Talbot, D. R. S., and Willis, J. R., 1992, "Some Simple Explicit Bounds for the Overall Behaviour of Nonlinear Composites," Int. J. Solids Struct., **29**(14–15), pp. 1981–1987.
[131] Ponte Castañeda, P., 1991, "The Effective Mechanical Properties of Nonlinear Isotropic Composites," J. Mech. Phys. Solids, **39**(1), pp. 45–71.
[132] Ponte Castañeda, P., 1992, "New Variational Principles in Plasticity and Their Application to Composite Materials," J. Mech. Phys. Solids, **40**(8), pp. 1757–1788.
[133] Ponte Castañeda, P., deBotton, G., and Li, G., 1992, "Effective Properties of Nonlinear Inhomogeneous Dielectrics," Phys. Rev. B, **46**(8), pp. 4387–4394.
[134] deBotton, G., and Ponte Castañeda, P., 1993, "Elastoplastic Constitutive Relations for Fiber-Reinforced Solids," Int. J. Solids Struct., **30**(14), pp. 1865–1890.
[135] Ponte Castañeda, P., and Suquet, P., 1998, "Nonlinear Composites," Adv. Appl. Mech., **34**, pp. 171–302.
[136] Ponte Castañeda, P., 1996, "Exact Second-Order Estimates for the Effective Mechanical Properties of Nonlinear Composite Materials," J. Mech. Phys. Solids, **44**(6), pp. 827–862.
[137] Lahellec, N., Mazerolle, F., and Michel, J. C., 2004, "Second-Order Estimate of the Macroscopic Behavior of Periodic Hyperelastic Composites: Theory and Experimental Validation," J. Mech. Phys. Solids, **52**(1), pp. 27–49.
[138] Leroy, Y., and Ponte Castañeda, P., 2001, "Bounds on the Self-Consistent Approximation for Nonlinear Media and Implications for the Second-Order Method," Compt. R. Acad. des Sci.—Ser. IIB, **329**, pp. 571–577.
[139] Ponte Castañeda, P., 2002, "Second-Order Homogenization Estimates for Nonlinear Composites Incorporating Field Fluctuations: I-Theory," J. Mech. Phys. Solids, **50**(4), pp. 737–757.
[140] Ponte Castañeda, P., 2002, "Second-Order Homogenization Estimates for Nonlinear Composites Incorporating Field Fluctuations: II-Application," J. Mech. Phys. Solids, **50**(4), pp. 759–782.
[141] Lopez-Pamies, O., and Ponte Castañeda, P., 2003, "Second-Order Estimates for the Large-Deformation Response of Particle-Reinforced Rubbers," Compt. R. Mécanique, **331**(1), pp. 1–8.
[142] Danas, K., Idiart, M. I., and Ponte Castañeda, P., 2008, "A Homogenization-Based Constitutive Model for Isotropic Viscoplastic Porous Media," Int. J. Solids Struct., **45**(11–12), pp. 3392–3409.
[143] deBotton, G., and Hariton, I., 2002, "High-Rank Nonlinear Sequentially Laminated Composites and Their Possible Tendency Towards Isotropic Behavior," J. Mech. Phys. Solids, **50**(12), pp. 2577–2595.
[144] deBotton, G., 2005, "Transversely Isotropic Sequentially Laminated Composites in Finite Elasticity," J. Mech. Phys. Solids, **53**(6), pp. 1334–1361.
[145] Brun, M., Lopez-Pamies, O., and Ponte Castañeda, P., 2007, "Homogenization Estimates for Fiber-Reinforced Elastomers With Periodic Microstructures," Int. J. Solids Struct., **44**(18–19), pp. 5953–5979.
[146] deBotton, G., and Shmuel, G., 2009, "Mechanics of Composites With Two Families of Finitely Extensible Fibers Undergoing Large Deformations," J. Mech. Phys. Solids, **57**(8), pp. 1165–1181.
[147] Rudykh, S., and deBotton, G., 2012 "Instabilities of Hyperelastic Fiber Composites: Micromechanical Versus Numerical Analyses," J. Elasticity, **106**(2), pp. 123–147.
[148] deBotton, G., and Oren, T., 2013, "Analytical and Numerical Analyses of the Micromechanics of Soft Fibrous Connective Tissues," Biomech. Model. Mechanobiol., **12**(1), pp. 151–166.
[149] Hashin, Z., 1990, "Thermoelastic Properties of Fiber Composites With Imperfect Interface," Mech. Mater., **8**(4), pp. 333–348.
[150] Hashin, Z., 1991, "The Spherical Inclusion With Imperfect Interface," ASME J. Appl. Mech., **58**(2), pp. 444–449.
[151] Qu, J., 1993, "The Effect of Slightly Weakened Interfaces on the Overall Elastic Properties of Composite Materials," Mech. Mater., **14**(4), pp. 269–281.
[152] Gao, Z., 1995, "A Circular Inclusion With Imperfect Interface: Eshelby's Tensor and Related Problems," ASME J. Appl. Mech., **62**(4), pp. 860–866.
[153] Torquato, S., and Rintoul, M. D., 1995, "Effect of the Interface on the Properties of Composite Media," Phys. Rev. Lett., **75**, pp. 4067–4070.
[154] Miloh, T., and Benveniste, Y., 1999, "On the Effective Conductivity of Composites With Ellipsoidal Inhomogeneities and Highly Conducting Interfaces," Proc. R. Soc. London A, **455**(1987), pp. 2687–2706.
[155] Sharma, P., and Ganti, S., 2004, "Size-Dependent Eshelby's Tensor for Embedded Nano-Inclusions Incorporating Surface/Interface Energies," ASME J. Appl. Mech., **71**(5), pp. 663–671.
[156] Duan, H. L., Wang, J., Huang, Z. P., and Karihaloo, B. L., 2005, "Size-Dependent Effective Elastic Constants of Solids Containing Nano-Inhomogeneities With Interface Stress," J. Mech. Phys. Solids, **53**(7), pp. 1574–1596.
[157] Duan, H. L., Wang, J., Karihaloo, B. L., and Huang, Z. P., 2006, "Nanoporous Materials can be Made Stiffer Than Non-Porous Counterparts by Surface Modification," Acta Mater., **54**(11), pp. 2983–2990.
[158] Andrianov, I. V., Bolshakov, V. I., Danishevs'kyy, V. V., and Weichert, D., 2007, "Asymptotic Simulation of Imperfect Bonding in Periodic Fibre-Reinforced Composite Materials Under Axial Shear," Int. J. Mech. Sci., **49**(12), pp. 1344–1354.
[159] Duan, H. L., Yi, X., Huang, Z. P., and Wang, J., 2007, "A Unified Scheme for Prediction of Effective Moduli of Multiphase Composites With Interface Effects. Part I: Theoretical Framework," Mech. Mater., **39**(12), pp. 81–93.
[160] Tan, H., Huang, Y., Liu, C., Ravichandran, G., and Paulino, G. H., 2007, "Constitutive Behaviors of Composites With Interface Debonding: The Extended Mori-Tanaka Method for Uniaxial Tension," Int. J. Fract., **146**(3), pp. 139–148.
[161] Yanase, K., and Ju, J. W., 2012, "Effective Elastic Moduli of Spherical Particle Reinforced Composites Containing Imperfect Interfaces," Int. J. Damage Mech., **21**(1), pp. 97–127.
[162] Buryachenko, V. A., 2013, "General Integral Equations of Thermoelasticity in Micromechanics of Composites With Imperfectly Bonded Interfaces," Int. J. Solids Struct., **50**(20–21), pp. 3190–3206.
[163] Chatzigeorgiou, G., Javili, A., and Steinmann, P., 2015, "Multiscale Modelling for Composites With Energetic Interface at the Micro- or Nanoscale," Math. Mech. Solids, **20**(9), pp. 1130–1145.
[164] Hashin, Z., and Rosen, B. W., 1964, "The Elastic Moduli of Reinforced-Reinforced Materials," ASME J. Appl. Mech., **31**(2), pp. 223–232.
[165] Jayaraman, K., and Reifsnider, K. L., 1992, "Residual Stresses in a Composite With Continuously Varying Young's Modulus in the Fiber/Matrix Interphase," J. Compos. Mater., **26**(6), pp. 770–791.
[166] Cherkaoui, M., Muller, D., Sabar, H., and Berveiller, M., 1996, "Thermoelastic Behavior of Composites With Coated Reinforcements: A Micromechanical Approach and Applications," Comput. Mater. Sci., **5**(1–3), pp. 45–52.

[167] Lutz, M. P., Monteiro, P. J. M., and Zimmerman, R. W., 1997, "Inhomogeneous Interfacial Transition Zone Model for the Bulk Modulus of Mortar," Cem. Concr. Res., **27**(7), pp. 1113–1122.
[168] Hashin, Z., and Monteiro, P. J. M., 2002, "An Inverse Method to Determine the Elastic Properties of the Interphase Between the Aggregate and the Cement Paste," Cem. Concr. Res., **32**(8), pp. 1291–1300.
[169] Lutz, M. P., and Zimmerman, R. W., 2005, "Effect of an Inhomogeneous Interphase Zone on the Bulk Modulus and Conductivity of a Particulate Composite," Int. J. Solids Struct., **42**(2), pp. 429–437.
[170] Shen, L., and Li, J., 2005, "Homogenization of a Fibre/Sphere With an Inhomogeneous Interphase for the Effective Elastic Moduli of Composites," Proc. R. Soc. London A, **461**(2057), pp. 1475–1504.
[171] Lipinski, P., Barhdadi, E. H., and Cherkaoui, M., 2006, "Micromechanical Modelling of an Arbitrary Ellipsoidal Multi-Coated Inclusion," Philos. Mag., **86**(10), pp. 1305–1326.
[172] Basaran, C., and Nie, S., 2007, "A Thermodynamics Based Damage Mechanics Model for Particulate Composites," Int. J. Solids Struct., **44**(3–4), pp. 1099–1114.
[173] Kari, S., Berger, H., Gabbert, U., Guinovart-Diaz, R., Bravo-Castillero, J., and Rodriguez-Ramos, R., 2008, "Evaluation of Influence of Interphase Material Parameters on Effective Material Properties of Three Phase Composites," Compos. Sci. Technol., **68**(3–4), pp. 684–691.
[174] Wang, X., Zhang, J., Wang, Z., Zhou, S., and Sun, X., 2011, "Effects of Interphase Properties in Unidirectional Fiber Reinforced Composite Materials," Mater. Des., **32**(6), pp. 3486–3492.
[175] Benveniste, Y., 2013, "Models of Thin Interphases and the Effective Medium Approximation in Composite Media With Curvilinearly Anisotropic Coated Inclusions," Int. J. Eng. Sci., **72**, pp. 140–154.
[176] Tran, B. V., Pham, D. C., and Nguyen, T. H. G., 2015, "Equivalent-Inclusion Approach and Effective Medium Approximations for Elastic Moduli of Compound-Inclusion Composites," Arch. Appl. Mech., **85**(12), pp. 1983–1995.
[177] Hashin, Z., 1983, "Analysis of Composite Materials—A Survey," ASME J. Appl. Mech., **50**(3), pp. 481–505.
[178] Mura, T., 1987, *Micromechanics of Defects in Solids*, Springer, Dordrecht, The Netherlands.
[179] Christensen, R. M., 1990, "A Critical Evaluation for a Class of Micro-Mechanics Models," J. Mech. Phys. Solids, **38**(3), pp. 379–404.
[180] Aboudi, J., 1992, *Mechanics of Composite Materials: A Unified Micromechanical Approach*, Elsevier, Amsterdam, Netherlands.
[181] Dasgupta, A., and Bhandarkar, S. M., 1992, "A Generalized Self-Consistent Mori-Tanaka Scheme for Fiber-Composites With Multiple Interphases," Mech. Mater., **14**(1), pp. 67–82.
[182] Mura, T., Shodja, H. M., and Hirose, Y., 1996, "Inclusion Problems," ASME Appl. Mech. Rev., **49**, pp. 118–127.
[183] Suquet, P., 1997, *Continuum Micromechanics*, CISM International Centre for Mechanical Sciences/Springer, Vienna, Austria.
[184] Böhm, H. J., 1998, "A Short Introduction to Basic Aspects of Continuum Mechanics," Technical Report, Institute of Lightweight Design and Structural Biomechanics (ILSB), Vienna University of Technology, Wien, Austria, CDL-FMD Report No. 3.
[185] Nemat-Nasser, S., and Hori, M., 1999, *Micromechanics: Overall Properties of Heterogeneous Materials*, Elsevier, Amsterdam, The Netherlands.
[186] Gilormini, P., and Bréchet, Y., 1999, "Syntheses: Mechanical Properties of Heterogeneous Media: Which Material for Which Model? Which Model for Which Material?," Modell. Simul. Mater. Sci. Eng., **7**, pp. 805–816.
[187] Willis, J. R., 2000, "The Overall Response of Nonlinear Composite Media," Eur. J. Mech.—A/Solids, **19**, pp. 165–184.
[188] Zaoui, A., 2002, "Continuum Micromechanics: Survey," J. Eng. Mech., **128**(8), pp. 808–816.
[189] Milton, G. W., 2002, *The Theory of Composites* (Cambridge Monographs on Applied and Computational Mathematics) Cambridge University Press, Cambridge, UK.
[190] Li, L. X., and Wang, T. J., 2005, "A Unified Approach to Predict Overall Properties of Composite Materials," Mater. Charact., **54**(1), pp. 49–62.
[191] Zohdi, T. I., and Wriggers, P., 2005, *Introduction to Computational Micromechanics*, Springer-Verlag, Berlin.
[192] Mercier, S., Molinari, A., Berbenni, S., and Berveiller, M., 2012, "Comparison of Different Homogenization Approaches for Elastic-Viscoplastic Materials," Modell. Simul. Mater. Sci. Eng., **20**(2), p. 024004.
[193] Klusemann, B., Böhm, H. J., and Svendsen, B., 2012, "Homogenization Methods for Multi-Phase Elastic Composites With Non-elliptical Reinforcements: Comparisons and Benchmarks," Eur. J. Mech.—A/Solids, **34**, pp. 21–37.
[194] Dvorak, G., 2013, *Micromechanics of Composite Materials*, Springer, Dordrecht, The Netherlands.
[195] Jöchen, K., 2013, *Homogenization of the Linear and Non-Linear Mechanical Behavior of Polycrystals* (Schriftenreihe Kontinuumsmechanik im Maschinenbau/Karlsruher Institut für Technologie, Institut für Technische Mechanik-Bereich Kontinuumsmechanik), Vol. 4, KIT Scientific Publishing, Karlsruhe, Germany.
[196] Ghossein, E., and Lévesque, M., 2014, "A Comprehensive Validation of Analytical Homogenization Models: The Case of Ellipsoidal Particles Reinforced Composites," Mech. Mater., **75**, pp. 135–150.
[197] Geers, M. G. D., Kouznetsova, V. G., and Brekelmans, W. A. M., 2010, "Multi-Scale Computational Homogenization: Trends and Challenges," J. Comput. Appl. Math., **234**(7), pp. 2175–2182.
[198] Nguyen, V. P., Stroeven, M., and Sluys, L. J., 2011, "Multiscale Continuous And Discontinuous Modelling of Heterogeneous Materials: A Review on Recent Developments," J. Multiscale Modell., **3**(4), pp. 229–270.
[199] Christman, T., Needleman, A., and Suresh, S., 1989, "An Experimental and Numerical Study of Deformation in Metal-Ceramic Composites," Acta Metall., **37**(1), pp. 3029–3050.
[200] Tvergaard, V., 1990, "Analysis of Tensile Properties for a Whisker-Reinforced Metal-Matrix Composite," Acta Metall. Mater., **38**(2), pp. 185–194.
[201] Bao, G., Hutchinson, J. W., and McMeeking, R. M., **1991** "Particle Reinforcement of Ductile Matrices Against Plastic Flow and Creep," Acta Metall. Mater., **39**(8), pp. 1871–1882.
[202] Smit, R. J. M., Brekelmans, W. A. M., and Meijer, H. E. H., 1999, "Prediction of the Large-Strain Mechanical Response of Heterogeneous Polymer Systems: Local and Global Deformation Behaviour of a Representative Volume Element of Voided Polycarbonate," J. Mech. Phys. Solids, **47**(2), pp. 201–221.
[203] van der Sluis, O., Schreurs, P. J. G., and Meijer, H. E. H., 1999, "Effective Properties of a Viscoplastic Constitutive Model Obtained by Homogenisation," Mech. Mater., **31**(11), pp. 743–759.
[204] Mandel, J., 1972, *Plasticité Classique, Viscoplasticité* (CISM Courses and Lectures), Vol. 97, Springer-Verlag, New York.
[205] Molinari, A., and Mercier, S., 2001, "Micromechanical Modelling of Porous Materials Under Dynamic Loading," J. Mech. Phys. Solids, **49**(7), pp. 1497–1516.
[206] Costanzo, F., Gray, G. L., and Andia, P. C., 2005, "On the Definitions of Effective Stress and Deformation Gradient for Use in MD: Hill's Macro-Homogeneity and the Virial Theorem," Int. J. Eng. Sci., **43**(7), pp. 533–555.
[207] Ricker, S., Mergheim, J., and Steinmann, P., 2009, "On the Multiscale Computation of Defect Driving Forces," Int. J. Multiscale Comput. Eng., **7**(5), pp. 457–474.
[208] Reina, C., 2011, "Multiscale Modeling and Simulation of Damage by Void Nucleation and Growth," Ph.D. thesis, California Institute of Technology, Pasadena, CA.
[209] Jacques, N., Mercier, S., and Molinari, A., 2012, "Effects of Microscale Inertia on Dynamic Ductile Crack Growth," J. Mech. Phys. Solids, **60**(4), pp. 665–690.
[210] de Souza Neto, E. A., Blanco, P. J., Sánchez, P. J., and Feijóo, R. A., 2015, "An RVE-Based Multiscale Theory of Solids With Micro-Scale Inertia and Body Force Effects," Mech. Mater., **80(Part A)**, pp. 136–144.
[211] Yue, X., and Weinan, E., 2007, "The Local Microscale Problem in the Multiscale Modeling of Strongly Heterogeneous Media: Effects of Boundary Conditions and Cell Size," J. Comput. Phys., **222**(2), pp. 556–572.
[212] W. E., Ming, P., and Zhang, P., 2005, "Analysis of the Heterogeneous Multiscale Method for Elliptic Homogenization Problems," J. Am. Math. Soc., **18**, pp. 121–156.
[213] Weinan, E., Engquist, B., Li, X., Ren, W., and Vanden-Eijnden, E., 2007, "The Heterogeneous Multiscale Method: A Review," Commun. Comput. Phys., **2**, pp. 367–450.
[214] Wongsto, A., and Li, S., 2005, "Micromechanical FE Analysis of UD Fibre-Reinforced Composites With Fibres Distributed at Random Over the Transverse Cross-Section," Composites Part A, **36**(9), pp. 1246–1266.
[215] Suquet, P., 1987, "Elements of Homogenization for Inelastic Solid Mechanics," *Homogenization Techniques for Composite Media*, E. Sanchez-Palencia, and A. Zaoui, eds., Springer-Verlag, Berlin, pp. 193–287.
[216] Huet, C., 1990, "Application of Variational Concepts to Size Effects in Elastic Heterogeneous Bodies," J. Mech. Phys. Solids, **38**(6), pp. 813–841.
[217] Hollister, S. J., and Kikuchi, N., 1992, "A Comparison of Homogenization and Standard Mechanic Analyses for Periodic Porous Composites," Comput. Mech., **10**(2), pp. 73–95.
[218] Nemat-Nasser, S., and Hori, M., 1995, "Universal Bounds for Overall Properties of Linear and Nonlinear Heterogeneous Solids," J. Eng. Mater. Technol., **117**(4), pp. 412–432.
[219] Hori, M., and Nemat-Nasser, S., 1999, "On Two Micromechanics Theories for Determining Micro–Macro Relations in Heterogeneous Solids," Mech. Mater., **31**(10), pp. 667–682.
[220] van der Sluis, O., Schreurs, P. J. G., Brekelmans, W. A. M., and Meijer, H. E. H., 2000, "Overall Behaviour of Heterogeneous Elastoviscoplastic Materials: Effect of Microstructural Modelling," Mech. Mater., **32**(8), pp. 449–462.
[221] Terada, K., Hori, M., Kyoya, T., and Kikuchi, N., 2000, "Simulation of the Multi-Scale Convergence in Computational Homogenization Approaches," Int. J. Solids Struct., **37**(16), pp. 2285–2311.
[222] Miehe, C., 2002, "Strain-Driven Homogenization of Inelastic Microstructures and Composites Based on an Incremental Variational Formulation," Int. J. Numer. Methods Eng., **55**(11), pp. 1285–1322.
[223] Kanit, T., Forest, S., Galliet, I., Mounoury, V., and Jeulin, D., 2003, "Determination of the Size of the Representative Volume Element for Random Composites: Statistical and Numerical Approach," Int. J. Solids Struct., **40**(13–14), pp. 3647–3679.
[224] Perić, D., de Souza Neto, E. A., Feijóo, R. A., Partovi, M., and Carneiro Molina, A. J., 2011, "On Micro-To-Macro Transitions for Multi-Scale Analysis of Non-Linear Heterogeneous Materials: Unified Variational Basis and Finite Element Implementation," Int. J. Numer. Methods Eng., **87**(1–5), pp. 149–170.
[225] Kaczmarczyk, L., Pearce, C. J., and Bićanić, N., 2008, "Scale Transition and Enforcement of RVE Boundary Conditions in Second-Order Computational Homogenization," Int. J. Numer. Methods Eng., **74**(3), pp. 506–522.

[226] Shen, H., and Brinson, L. C., 2006, "A Numerical Investigation of the Effect of Boundary Conditions and Representative Volume Element Size for Porous Titanium," J. Mech. Mater. Struct., **1**(7), pp. 1179–1204.
[227] Drago, A., and Pindera, M.-J., 2007, "Micro-Macromechanical Analysis of Heterogeneous Materials: Macroscopically Homogeneous vs Periodic Microstructures," Compos. Sci. Technol., **67**(6), pp. 1243–1263.
[228] Mercer, B. S., Mandadapu, K. K., and Papadopoulos, P., 2015, "Novel Formulations of Microscopic Boundary-Value Problems in Continuous Multiscale Finite Element Methods," Comput. Methods Appl. Mech. Eng., **286**, pp. 268–292.
[229] Pecullan, S., Gibiansky, L. V., and Torquato, S., 1999, "Scale Effects on the Elastic Behavior of Periodic and Hierarchical Two-Dimensional Composites," J. Mech. Phys. Solids, **47**(7), pp. 1509–1542.
[230] Jiang, M., Alzebdeh, K., Jasiuk, I., and Ostoja-Starzewski, M., 2001, "Scale and Boundary Conditions Effects in Elastic Properties of Random Composites," Acta Mech., **148**(1), pp. 63–78.
[231] Ostoja-Starzewski, M., 2006, "Material Spatial Randomness: From Statistical to Representative Volume Element," Probab. Eng. Mech., **21**(2), pp. 112–132.
[232] Larsson, F., and Runesson, K., 2007, "RVE Computations With Error Control and Adaptivity: The Power of Duality," Comput. Mech., **39**(5), pp. 647–661.
[233] Saroukhani, S., Vafadari, R., Andersson, R., Larsson, F., and Runesson, K., 2015, "On Statistical Strain and Stress Energy Bounds From Homogenization and Virtual Testing," Eur. J. Mech.—A/Solids, **51**, pp. 77–95.
[234] Xia, Z., Zhang, Y., and Ellyin, F., 2003, "A Unified Periodical Boundary Conditions for Representative Volume Elements of Composites and Applications," Int. J. Solids Struct., **40**(8), pp. 1907–1921.
[235] Hazanov, S., and Huet, C., 1994, "Order Relationships for Boundary Conditions Effect in Heterogeneous Bodies Smaller Than the Representative Volume," J. Mech. Phys. Solids, **42**(12), pp. 1995–2011.
[236] Hazanov, S., and Amieur, M., 1995, ""On Overall Properties of Elastic Heterogeneous Bodies Smaller Than the Representative Volume," Int. J. Eng. Sci., **33**(9), pp. 1289–1301.
[237] Pahr, D. H., and Zysset, P. K., 2008, "Influence of Boundary Conditions on Computed Apparent Elastic Properties of Cancellous Bone," Biomech. Model. Mechanobiol., **7**(6), pp. 463–476.
[238] Mesarovic, S. D., and Padbidri, J., 2005, "Minimal Kinematic Boundary Conditions for Simulations of Disordered Microstructures," Philos. Mag., **85**(1), pp. 65–78.
[239] Coenen, E. W. C., Kouznetsova, V. G., and Geers, M. G. D., 2012, "Novel Boundary Conditions for Strain Localization Analyses in Microstructural Volume Elements," Int. J. Numer. Methods Eng., **90**(1), pp. 1–21.
[240] Inglis, H. M., Geubelle, P. H., and Matouš, K., 2008, "Boundary Condition Effects on Multiscale Analysis of Damage Localization," Philos. Mag., **88**(16), pp. 2373–2397.
[241] Larsson, F., Runesson, K., Saroukhani, S., and Vafadari, R., 2011, "Computational Homogenization Based on a Weak Format of Micro-Periodicity for RVE-Problems," Comput. Methods Appl. Mech. Eng., **200**(1–4), pp. 11–26.
[242] Tyrus, J. M., Gosz, M., and DeSantiago, E., 2007, "A Local Finite Element Implementation for Imposing Periodic Boundary Conditions on Composite Micromechanical Models," Int. J. Solids Struct., **44**(9), pp. 2972–2989.
[243] Glüge, R., 2013, "Generalized Boundary Conditions on Representative Volume Elements And Their Use in Determining the Effective Material Properties," Comput. Mater. Sci., **79**, pp. 408–416.
[244] Fritzen, F., and Böhlke, T., 2010, "Influence of the Type of Boundary Conditions on the Numerical Properties of Unit Cell Problems," Tech. Mech., **30**, pp. 354–363.
[245] Drugan, W. J., and Willis, J. R., 1996, "A Micromechanics-Based Nonlocal Constitutive Equation and Estimates of Representative Volume Element Size for Elastic Composites," J. Mech. Phys. Solids, **44**(4), pp. 497–524.
[246] Kouznetsova, V. G., Geers, M. G. D., and Brekelmans, W. A. M., 2002, "Multi-Scale Constitutive Modelling of Heterogeneous Materials With a Gradient-Enhanced Computational Homogenization Scheme," Int. J. Numer. Methods Eng., **54**(8), pp. 1235–1260.
[247] Kouznetsova, V. G., Geers, M. G. D., and Brekelmans, W. A. M., 2004, "Multi-Scale Second-Order Computational Homogenization of Multi-Phase Materials: A Nested Finite Element Solution Strategy," Comput. Methods Appl. Mech. Eng., **193**(48–51), pp. 5525–5550.
[248] Gitman, I. M., Askes, H., and Aifantis, E. C., 2005, "The Representative Volume Size in Static and Dynamic Micro–Macro Transitions," Int. J. Fract., **135**(1), pp. L3–L9.
[249] Geers, M. G. D., Coenen, E. W. C., and Kouznetsova, V. G., 2007, "Multi-Scale Computational Homogenization of Structured Thin Sheets," Modell. Simul. Mater. Sci. Eng., **15**, pp. 393–404.
[250] Nguyen, V.-D., Becker, G., and Noels, L., 2013, "Multiscale Computational Homogenization Methods With a Gradient Enhanced Scheme Based on the Discontinuous Galerkin Formulation," Comput. Methods Appl. Mech. Eng., **260**, pp. 63–77.
[251] Javili, A., McBride, A., Mergheim, J., Steinmann, P., and Schmidt, U., 2013, "Micro-To-Macro Transitions for Continua With Surface Structure at the Microscale," Int. J. Solids Struct., **50**(16–17), pp. 2561–2572.
[252] Javili, A., Chatzigeorgiou, G., McBride, A., Steinmann, P., and Linder, C., 2015, "Computational Homogenization of Nano-Materials Accounting for Size Effects Via Surface Elasticity," GAMM Mitt., **38**(2), pp. 285–312.
[253] Mindlin, R. D., 1965, "Second Gradient of Strain and Surface-Tension in Linear Elasticity," Int. J. Solids Struct., **1**(4), pp. 417–438.
[254] Cordero, N. M., Forest, S., and Busso, E. P., 2015, "Second Strain Gradient Elasticity of Nano-Objects," J. Mech. Phys. Solids (in press).
[255] Davydov, D., Javili, A., and Steinmann, P., 2013, "On Molecular Statics and Surface-Enhanced Continuum Modeling of Nano-Structures," Comput. Mater. Sci., **69**, pp. 510–519.
[256] Larsson, F., Runesson, K., and Su, F., 2010, "Variationally Consistent Computational Homogenization of Transient Heat Flow," Int. J. Numer. Methods Eng., **81**, pp. 1659–1686.
[257] Sab, K., 1992, "On the Homogenization and the Simulation of Random Materials," Eur. J. Mech.—A/Solids, **11**, pp. 585–607.
[258] Ostoja-Starzewski, M., 1998, "Random Field Models of Heterogeneous Materials," Int. J. Solids Struct., **35**(19), pp. 2429–2455.
[259] Hill, R., 1963, "Elastic Properties of Reinforced Solids: Some Theoretical Principles," J. Mech. Phys. Solids, **11**(5), pp. 357–372.
[260] Huet, C., 1999, "Coupled Size and Boundary-Condition Effects in Viscoelastic Heterogeneous and Composite Bodies," Mech. Mater., **31**(12), pp. 787–829.
[261] Temizer, İ., and Zohdi, T. I., 2007, "A Numerical Method for Homogenization in Non-Linear Elasticity," Comput. Mech., **40**(2), pp. 281–298.
[262] El Houdaigui, F., Forest, S., Gourgues, A.-F., and Jeulin, D., 2007, "On the Size of the Representative Volume Element for Isotropic Elastic Polycrystalline Copper," *IUTAM Symposium on Mechanical Behavior and Micro-Mechanics of Nanostructured Materials* (Solid Mechanics and Its Applications), Vol. 144, Y. L. Bai, Q. S. Zheng, and Y. G. Wei, eds., Springer, Dordrecht, The Netherlands, pp. 171–180.
[263] Gusev, A. A., 1997, "Representative Volume Element Size for Elastic Composites: A Numerical Study," J. Mech. Phys. Solids, **45**(9), pp. 1449–1459.
[264] Shan, Z., and Gokhale, A. M., 2002, "Representative Volume Element for Non-Uniform Micro-Structure," Comput. Mater. Sci., **24**(3), pp. 361–379.
[265] Dirrenberger, J., Forest, S., and Jeulin, D., 2014, "Towards Gigantic RVE Sizes for 3D Stochastic Fibrous Networks," Int. J. Solids Struct., **51**(2), pp. 359–376.
[266] Harper, L. T., Qian, C., Turner, T. A., Li, S., and Warrior, N. A., 2012, "Representative Volume Elements for Discontinuous Carbon Fibre Composites—Part 2: Determining the Critical Size," Compos. Sci. Technol., **72**(2), pp. 204–210.
[267] Jafari, A., Afaghi Khatibi, A., and Mosavi Mashhadi, M., 2011, "Comprehensive Investigation on Hierarchical Multiscale Homogenization Using Representative Volume Element for Piezoelectric Nanocomposites," Composites: Part B, **42**(3), pp. 553–561.
[268] Galli, M., Cugnoni, J., and Botsis, J., 2012, "Numerical and Statistical Estimates of the Representative Volume Element of Elastoplastic Random Composites," Eur. J. Mech.—A/Solids, **33**, pp. 31–38.
[269] Trias, D., Costa, J., Turon, A., and Hurtado, J. E., 2006, "Determination of the Critical Size of a Statistical Representative Volume Element (SRVE) for Carbon Reinforced Polymers," Acta Mater., **54**(13), pp. 3471–3484.
[270] Gitman, I. M., Askes, H., and Sluys, L. J., 2007, "Representative Volume: Existence and Size Determination," Eng. Fract. Mech., **74**(16), pp. 2518–2534.
[271] Böhm, H. J., and Han, W., 2001, "Comparisons Between Three-Dimensional and Two-Dimensional Multi-Particle Unit Cell Models for Particle Reinforced Metal Matrix Composites," Model. Simul. Mater. Sci. Eng., **9**(2), pp. 47–65.
[272] Pelissou, C., Baccou, J., Monerie, Y., and Perales, F., 2009, "Determination of the Size of the Representative Volume Element for Random Quasi-Brittle Composites," Int. J. Solids Struct., **46**(14–15), pp. 2842–2855.
[273] Hoang, T. H., Guerich, M., and Yvonnet, J., 2016, "Determining the Size of RVE for Nonlinear Random Composites in an Incremental Computational Homogenization Framework," J. Eng. Mech., **142**(5), p. 04016018.
[274] Stroeven, M., Askes, H., and Sluys, L. J., 2004, "Numerical Determination of Representative Volumes for Granular Materials," Comput. Methods Appl. Mech. Eng., **193**(30–32), pp. 3221–3238.
[275] Thomas, M., Boyard, N., Perez, L., Jarny, Y., and Delaunay, D., 2008, "Representative Volume Element of Anisotropic Unidirectional Carbon-Epoxy Composite With High-Fibre Volume Fraction," Compos. Sci. Technol., **68**(15–16), pp. 3184–3192.
[276] Khisaeva, Z. F., and Ostoja-Starzewski, M., 2006, "On the Size of RVE in Finite Elasticity of Random Composites," J. Elasticity, **85**, pp. 153–173.
[277] Temizer, İ., Wu, T., and Wriggers, P., 2013, "On the Optimality of the Window Method in Computational Homogenization," Int. J. Eng. Sci., **64**, pp. 66–73.
[278] Salmi, M., Auslender, F., Bornert, M., and Fogli, M., 2012, "Apparent and Effective Mechanical Properties of Linear Matrix-Inclusion Random Composites: Improved Bounds for the Effective Behavior," Int. J. Solids Struct., **49**(10), pp. 1195–1211.
[279] Glüge, R., Weber, M., and Bertram, A., 2012, "Comparison of Spherical and Cubical Statistical Volume Elements With Respect to Convergence, Anisotropy, and Localization Behavior," Comput. Mater. Sci., **63**, pp. 91–104.
[280] Talebi, H., Zi, G., Silani, M., Samaniego, E., and Rabczuk, T., 2012, "A Simple Circular Cell Method for Multilevel Finite Element Analysis," J. Appl. Math., **2012**, p. 526846.
[281] Meier, H. A., Steinmann, P., and Kuhl, E., 2008, "Towards Multiscale Computation of Confined Granular Media: Contact Forces, Stresses and Tangent Operators," Tech. Mech., **28**, pp. 32–42.
[282] Balzani, D., Scheunemann, L., Brands, D., and Schröder, J., 2014, "Construction of Two- and Three-Dimensional Statistically Similar RVEs

for Coupled Micro–Macro Simulations," Comput. Mech., **54**(5), pp. 1269–1284.
[283] Scheunemann, L., Balzani, D., Brands, D., and Schröder, J., 2015, "Design of 3D Statistically Similar Representative Volume Elements Based on Minkowski Functionals," Mech. Mater., **90**, pp. 185–201.
[284] Swaminathan, S., and Ghosh, S., 2006, "Statistically Equivalent Representative Volume Elements for Unidirectional Composite Microstructures: Part I—Without Damage," J. Compos. Mater., **40**, pp. 583–604.
[285] Swaminathan, S., and Ghosh, S., 2006, "Statistically Equivalent Representative Volume Elements for Unidirectional Composite Microstructures: Part II—With Interfacial Debonding," J. Compos. Mater., **40**, pp. 605–621.
[286] Zeman, J., and Šejnoha, M., 2001, "Numerical Evaluation of Effective Elastic Proper Ties of Graphite Fiber Tow Impregnated by Polymer Matrix," J. Mech. Phys. Solids, **49**(1), pp. 69–90.
[287] Ren, Z.-Y., and Zheng, Q.-S., 2002, "A Quantitative Study of Minimum Sizes of Representative Volume Elements of Cubic Polycrystals-Numerical Experiments," J. Mech. Phys. Solids, **50**(4), pp. 881–893.
[288] Ren, Z.-Y., and Zheng, Q.-S., 2004, "Effects of Grain Sizes, Shapes, and Distribution on Minimum Sizes of Representative Volume Elements of Cubic Polycrystals," Mech. Mater., **36**(12), pp. 1217–1229.
[289] Moussaddy, H., Therriault, D., and Lévesque, M., 2013, "Assessment of Existing and Introduction of a New and Robust Efficient Definition of the Representative Volume Element," Int. J. Solids Struct., **50**(24), pp. 3817–3828.
[290] Chow, T. S., 1980, "The Effect of Particle Shape on the Mechanical Properties of Filled Polymers," J. Mater. Sci., **15**(8), pp. 1873–1888.
[291] Lee, B. J., and Mear, M. E., 1991, "Effect of Inclusion Shape on the Stiffness of Nonlinear Two-Phase Composites," J. Mech. Phys. Solids, **39**(5), pp. 627–649.
[292] Llorca, J., Needleman, A., and Suresh, S., 1991, "An Analysis of the Effects of Matrix Void Growth on Deformation and Ductility in Metal-Ceramic Composites," Acta Metall. Mater., **39**(10), pp. 2317–2335.
[293] Wang, Y. M., and Weng, G. J., 1992, "The Influence of Inclusion Shape on the Overall Viscoelastic Behavior of Composites," ASME J. Appl. Mech., **59**(3), pp. 510–518.
[294] Böhm, H. J., Rammerstorfer, F. G., Fischer, F. D., and Siegmund, T., 1994, "Microscale Arrangement Effects on the Thermomechanical Behavior of Advanced Two-Phase Materials," J. Eng. Mater. Technol., **116**(3), pp. 268–273.
[295] Monette, L., Anderson, M. P., and Grest, G. S., 1994, "Effect of Volume Fraction and Morphology of Reinforcing Phases in Composites," J. Appl. Phys., **75**, pp. 1155–1170.
[296] Ju, J. W., and Chen, T. M., 1994, "Micromechanics and Effective Moduli of Elastic Composites Containing Randomly Dispersed Ellipsoidal Inhomogeneities," Acta Mech., **103**(1), pp. 103–121.
[297] Ponte Castañeda, P., and Willis, J. R., 1995, "The Effect of Spatial Distribution on the Effective Behavior of Composite Materials and Cracked Media," J. Mech. Phys. Solids, **43**(12), pp. 1919–1951.
[298] Shen, Y.-L., Finot, M., Needleman, A., and Suresh, S., 1994, "Effective Elastic Response of Two-Phase Composites," Acta Metall. Mater., **42**, pp. 77–97.
[299] Ghosh, S., Nowak, Z., and Lee, K., 1997, "Quantitative Characterization and Modeling of Composite Microstructures by Voronoi Cells," Acta Mater., **45**(1), pp. 2215–2234.
[300] Deve, H. E., 1999, "Effect of Fiber Spatial Arrangement on the Transverse Strength of Titanium Matrix Composites," Metall. Mater. Trans. A, **30**(9), pp. 2513–2522.
[301] Ohno, N., Wu, X., and Matsuda, T., 2000, "Homogenized Properties of Elastic-Viscoplastic Composites With Periodic Internal Structures," Int. J. Mech. Sci., **42**(8), pp. 1519–1536.
[302] Segurado, J., González, C., and Llorca, J., 2003, "A Numerical Investigation of the Effect of Particle Clustering on the Mechanical Properties of Composites," Acta Mater., **51**(8), pp. 2355–2369.
[303] Stora, E., He, Q.-C., and Bary, B., 2006, "Influence of Inclusion Shapes on the Effective Linear Elastic Properties of Hardened Cement Pastes," Cem. Concr. Res., **36**(7), pp. 1330–1344.
[304] Terada, K., Watanabe, I., and Akiyama, M., 2006, "Effects of Shape and Size of Crystal Grains on the Strengths of Polycrystalline Metals," Int. J. Multiscale Comput. Eng., **4**(4), pp. 445–460.
[305] Romanova, V. A., Balokhonov, R. R., and Schmauder, S., 2009, "The Influence of the Reinforcing Particle Shape and Interface Strength on the Fracture Behavior of a Metal Matrix Composite," Acta Mater., **57**(1), pp. 97–107.
[306] Ayyar, A., Crawford, G. A., Williams, J. J., and Chawla, N., 2008, "Numerical Simulation of the Effect of Particle Spatial Distribution and Strength on Tensile Behavior of Particle Reinforced Composites," Comput. Mater. Sci., **44**(2), pp. 496–506.
[307] Marcos-Gómez, D., Ching-Lloyd, J., Elizalde, M. R., Clegg, W. J., and Molina-Aldareguia, J. M., 2010, "Predicting the Thermal Conductivity of Composite Materials With Imperfect Interfaces," Compos. Sci. Technol., **70**(16), pp. 2276–2283.
[308] Williams, J. J., Segurado, J., Llorca, J., and Chawla, N., 2012, "Three Dimensional (3D) Microstructure-Based Modeling of Interfacial Decohesion in Particle Reinforced Metal Matrix Composites," Mater. Sci. Eng.: A, **557**(16), pp. 113–118.
[309] Mikdam, A., Makradi, A., Koutsawa, Y., and Belouettar, S., 2013, "Microstructure Effect on the Mechanical Properties of Heterogeneous Composite Materials," Composites: Part B, **44**(1), pp. 714–721.
[310] Mortazavi, B., Bardon, J., and Ahzi, S., 2013, "Interphase Effect on the Elastic and Thermal Conductivity Response of Polymer Nanocomposite Materials: 3D Finite Element Study," Comput. Mater. Sci., **69**, pp. 100–106.
[311] Savvas, D., Stefanou, G., Papadrakakis, M., and Deodatis, G., 2014, "Homogenization of Random Heterogeneous Media With Inclusions of Arbitrary Shape Modeled by XFEM," Comput. Mech., **54**(5), pp. 1221–1235.
[312] Altendorf, H., Jeulin, D., and Willot, F., 2014, "Influence of the Fiber Geometry on the Macroscopic Elastic and Thermal Properties," Int. J. Solids Struct., **51**(23–24), pp. 3807–3822.
[313] El Moumen, A., Kanit, T., Imad, A., and El Minor, H., 2015, "Effect of Reinforcement Shape on Physical Properties and Representative Volume Element of Particles-Reinforced Composites: Statistical and Numerical Approaches," Mech. Mater., **83**, pp. 1–16.
[314] El Moumen, A., Kanit, T., Imad, A., and El Minor, H., 2015, "Computational Thermal Conductivity in Porous Materials Using Homogenization Techniques: Numerical and Statistical Approaches," Comput. Mater. Sci., **97**, pp. 148–158.
[315] Brockenbrough, J. R., Suresh, S., and Wienecke, H. A., 1991, "Deformation of Metal-Matrix Composites With Continuous Fibers: Geometrical Effects of Fiber Distribution and Shape," Acta Metall. Mater., **39**(5), pp. 735–752.
[316] Kouznetsova, V. G., Brekelmans, W. A. M., and Baaijens, F. P. T., 2001, "An Approach to Micro–Macro Modeling of Heterogeneous Materials," Comput. Mech., **27**(1), pp. 37–48.
[317] Trias, D., Costa, J., Mayugo, J. A., and Hurtado, J. E., 2006, "Random Models Versus Periodic Models for Fibre Reinforced Composites," Comput. Mater. Sci., **38**(2), pp. 316–324.
[318] Segurado, J., and Llorca, J., 2006, "Computational Micromechanics of Composites: The Effect of Particle Spatial Distribution," Mech. Mater., **38**(8–10), pp. 873–883.
[319] Kari, S., Berger, H., Rodriguez-Ramos, R., and Gabbert, U., 2007, "Computational Evaluation of Effective Material Properties of Composites Reinforced by Randomly Distributed Spherical Particles," Compos. Struct., **77**(2), pp. 223–231.
[320] Tan, H., Huang, Y., Liu, C., Ravichandran, G., Inglis, H. M., and Geubelle, P. H., 2007, "The Uniaxial Tension of Particulate Composite Materials With Nonlinear Interface Debonding," Int. J. Solids Struct., **44**(6), pp. 1809–1822.
[321] Chawla, N., Sidhu, R. S., and Ganesh, V. V., 2006, "Three-Dimensional Visualization and Microstructure-Based Modeling of Deformation in Particle-Reinforced Composites," Acta Mater., **54**(6), pp. 1541–1548.
[322] Li, Y., Waas, A. M., and Arruda, E. M., 2011, "A Closed-Form, Hierarchical, Multi-Interphase Model for Composites—Derivation, Verification and Application to Nanocomposites," J. Mech. Phys. Solids, **59**(1), pp. 43–63.
[323] Mortazavi, B., Baniassadi, M., Bardon, J., and Ahzi, S., 2013, "Modeling of Two-Phase Random Composite Materials by Finite Element, Mori-Tanaka and Strong Contrast Methods," Composites Part B, **45**(1), pp. 1117–1125.
[324] Kochmann, D. M., and Venturini, G. N., 2013, "Homogenized Mechanical Properties of Auxetic Composite Materials in Finite-Strain Elasticity," Smart Mater. Struct., **22**(8), p. 084004.
[325] Kulkarni, M. G., Geubelle, P. H., and Matouš, K., 2009, "Multi-Scale Modeling of Heterogeneous Adhesives: Effect of Particle Decohesion," Mech. Mater., **41**(5), pp. 573–583.
[326] Matouš, K., Kulkarni, M. G., and Geubelle, P. H., 2008, "Multiscale Cohesive Failure Modeling of Heterogeneous Adhesives," J. Mech. Phys. Solids, **56**(4), pp. 1511–1533.
[327] McBride, A., Mergheim, J., Javili, A., Steinmann, P., and Bargmann, S., 2012, "Micro-to-Macro Transitions for Heterogeneous Material Layers Accounting for In-Plane Stretch," J. Mech. Phys. Solids, **60**(6), pp. 1221–1239.
[328] Ghosh, S., and Moorthy, S., 1995, "Elastic-Plastic Analysis of Arbitrary Heterogeneous Materials With the Voronoi Cell Finite Element Method," Comput. Methods Appl. Mech. Eng., **121**(1–4), pp. 373–409.
[329] Ghosh, S., Lee, K., and Moorthy, S., 1995, "Multiple Scale Analysis of Heterogeneous Elastic Structures Using Homogenization Theory and Voronoi Cell Finite Element Method," Int. J. Solids Struct., **32**(1), pp. 27–62.
[330] Moorthy, S., and Ghosh, S., 1996, "A Model for Analysis of Arbitrary Composite and Porous Microstructures With Voronoi Cell Finite Elements," Int. J. Numer. Methods Eng., **39**(14), pp. 2363–2398.
[331] Moulinec, H., and Suquet, P., 1998, "A Numerical Method for Computing the Overall Response of Nonlinear Composites With Complex Microstructure," Comput. Methods Appl. Mech. Eng., **157**(1–2), pp. 69–94.
[332] Lebensohn, R. A., 2001, "N-site modeling of a 3D Viscoplastic Polycrystal Using Fast Fourier Transform," Acta Mater., **49**(14), pp. 2723–2737.
[333] Vinogradov, V., and Milton, G. W., "An Accelerated FFT Algorithm for Thermoelastic and Non-Linear Composites," Int. J. Numer. Methods Eng., **76**(11), pp. 1678–1695.
[334] Lee, S.-B., Lebensohn, R. A., and Rollett, A. D., 2011, "Modeling the Viscoplastic Micromechanical Response of Two-Phase Materials Using Fast Fourier Transforms," Int. J. Plast., **27**(5), pp. 707–727.
[335] Escoda, J., Willot, F., Jeulin, D., Sanahuja, J., and Toulemonde, C., 2011, "Estimation of Local Stresses and Elastic Properties of a Mortar Sample by FFT Computation of Fields on a 3D Image," Cem. Concr. Res., **41**(5), pp. 542–556.
[336] Moulinec, H., and Silva, F., 2014, "Comparison of Three Accelerated FFT-Based Schemes for Computing the Mechanical Response of Composite Materials," Int. J. Numer. Methods Eng., **97**(13), pp. 960–985.
[337] Spahn, J., Andrä, H., Kabel, M., and Müller, R., 2014, "A Multiscale Approach for Modeling Progressive Damage of Composite Materials Using Fast Fourier Transforms," Comput. Methods Appl. Mech. Eng., **268**, pp. 871–883.

[338] Kabel, M., Merkert, D., and Schneider, M., 2015, "Use of Composite Voxels in FFT-Based Homogenization," Comput. Methods Appl. Mech. Eng., **294**, pp. 168–188.
[339] Michel, J. C., Moulinec, H., and Suquet, P., 1999, "Effective Properties of Composite Materials With Periodic Microstructure: A Computational Approach," Comput. Methods Appl. Mech. Eng., **172**(1–4), pp. 109–143.
[340] Monchiet, V., and Bonnet, G., 2012, "A Polarization Based FFT Iterative Scheme for Computing the Effective Properties of Elastic Composites With Arbitrary Contrast," Int. J. Numer. Methods Eng., **89**(11), pp. 1419–1436.
[341] Michel, J. C., Moulinec, H., and Suquet, P., 2000, "A Computational Method Based on Augmented Lagrangians and Fast Fourier Transforms for Composites With High Contrast," Comput. Model. Eng. Sci., **1**, pp. 79–88.
[342] Michel, J. C., Moulinec, H., and Suquet, P., 2001, "A Computational Scheme for Linear and Non-Linear Composites With Arbitrary Phase Contrast," Int. J. Numer. Methods Eng., **52**(1–2), pp. 139–160.
[343] Brisard, S., and Dormieux, L., 2010, "FFT-Based Methods for the Mechanics of Composites: A General Variational Framework," Comput. Mater. Sci., **49**(3), pp. 663–671.
[344] Willot, F., Abdallah, B., and Pellegrini, Y.-P., 2014, "Fourier-Based Schemes With Modified Green Operator for Computing the Electrical Response of Heterogeneous Media With Accurate Local Fields," Int. J. Numer. Methods Eng., **98**(7), pp. 518–533.
[345] Miehe, C., and Dettmar, J., 2004, "A Framework for Micro–Macro Transitions in Periodic Particle Aggregates of Granular Materials," Comput. Methods Appl. Mech. Eng., **193**(3–5), pp. 225–256.
[346] Nguyen, T. K., Combe, G., Caillerie, D., and Desrues, J., 2014, "FEM x DEM Modelling of Cohesive Granular Materials: Numerical Homogenisation and Multi-Scale Simulations," Acta Geophys., **62**, pp. 1109–1126.
[347] Guo, N., and Zhao, J., 2014, "A Coupled FEM/DEM Approach for Hierarchical Multiscale Modelling of Granular Media," Int. J. Numer. Methods Eng., **99**(11), pp. 789–818.
[348] Kamiński, M., 1999, "Boundary Element Method Homogenization of the Periodic Linear Elastic Fiber Composites," Eng. Anal. Boundary Elem., **23**(10), pp. 815–823.
[349] Okada, H., Fukui, Y., and Kumazawa, N., 2001, "Homogenization Method for Heterogeneous Material Based on Boundary Element Method," Comput. Struct., **79**(20–21), pp. 1987–2007.
[350] Procházka, P., 2001, "Homogenization of Linear and of Debonding Composites Using the BEM," Eng. Anal. Boundary Elem., **25**(9), pp. 753–769.
[351] Renard, J., and Marmonier, M. F., 1987, "Etude de l'initiation de l'endommagement dans la Matrice d'un matériau Composite par une Méthode d'homogénisation," Aerosp. Sci. Technol., **6**, pp. 37–51.
[352] Takano, N., Ohnishi, Y., Zako, M., and Nishiyabu, K., 2000, "The Formulation of Homogenization Method Applied to Large Deformation Problem for Composite Materials," Int. J. Solids Struct., **37**(44), pp. 6517–6535.
[353] Feyel, F., and Chaboche, J.-L., 2000, "FE^2 Multiscale Approach for Modelling the Elastoviscoplastic Behaviour of Long Fibre SiC/Ti Composite Materials," Comput. Methods Appl. Mech. Eng., **183**(3–4), pp. 309–330.
[354] Feyel, F., 2003, "A Multilevel Finite Element Method (FE^2) to Describe the Response of Highly Non-Linear Structures Using Generalized Continua," Comput. Methods Appl. Mech. Eng., **192**(28–30), pp. 3233–3244.
[355] Terada, K., and Kikuchi, N., 2001, "A Class of General Algorithms for Multi-Scale Analyses of Heterogeneous Media," Comput. Methods Appl. Mech. Eng., **190**(40–41), pp. 5427–5464.
[356] Miehe, C., Schröder, J., and Schotte, J., 1999, "Computational Homogenization Analysis in Finite Plasticity Simulation of Texture Development in Polycrystalline Materials," Comput. Methods Appl. Mech. Eng., **171**(3–4), pp. 387–418.
[357] Miehe, C., and Koch, A., 2002, "Computational Micro-To-Macro Transitions of Discretized Microstructures Undergoing Small Strains," Arch. Appl. Mech., **72**(4), pp. 300–317.
[358] Miehe, C., Schröder, J., and Bayreuther, C., 2002, "On the Homogenization Analysis of Composite Materials Based on Discretized Fluctuations on the Micro-Structure," Acta Mech., **155**(1), pp. 1–16.
[359] Smit, R. J. M., Brekelmans, W. A. M., and Meijer, H. E. H., 1998, "Prediction of the Mechanical Behavior of Nonlinear Heterogeneous Systems by Multi-Level Finite Element Modeling," Comput. Methods Appl. Mech. Eng., **155**(1–2), pp. 181–192.
[360] Segurado, J., and Llorca, J., 2002, "A Numerical Approximation to the Elastic Properties of Sphere-Reinforced Composites," J. Mech. Phys. Solids, **50**(10), pp. 2107–2121.
[361] Terada, K., Saiki, I., Matsui, K., and Yamakawa, Y., 2003, "Two-Scale Kinematics and Linearization for Simultaneous Two-Scale Analysis of Periodic Heterogeneous Solids at Finite Strain," Comput. Methods Appl. Mech. Eng., **192**(31–32), pp. 3531–3563.
[362] Klinge, S., and Hackl, K., 2012, "Application of the Multiscale FEM to the Modeling of Nonlinear Composites With a Random Microstructure," Int. J. Multiscale Comput. Eng., **10**(3), pp. 213–227.
[363] Schröder, J., 2014, "A Numerical Two-Scale Homogenization Scheme: The FE^2-Method," *Plasticity and Beyond* (CISM Int. Centre for Mechanical Sciences), Vol. 550, J. Schröder, and K. Hackl, eds., Springer Vienna, Berlin, pp. 1–64.
[364] Moës, N., Cloirec, M., Cartraud, P., and Remacle, J.-F., 2003, "A Computational Approach to Handle Complex Microstructure Geometries," Comput. Methods Appl. Mech. Eng., **192**(28–30), pp. 3163–3177.
[365] Bouhala, L., Koutsawa, Y., Makradi, A., and Belouettar, S., 2014, "An Advanced Numerical Method for Predicting Effective Elastic Properties of Heterogeneous Composite Materials," Compos. Struct., **117**, pp. 114–123.
[366] Feyel, F., 1998, "Application du Calcul Parallèle aux Modèles à Grand Nombre De Variables Internes," Ph.D. thesis, Ecole des Mines de Paris, Paris, France.
[367] Feyel, F., 1999, "Multiscale FE^2 oviscoplastic Analysis of Composite Structures," Comput. Mater. Sci., **16**(1–4), pp. 344–354.
[368] Unger, J. F., 2013, "An FE^2-X^1 approach for Multiscale Localization Phenomena," J. Mech. Phys. Solids, **61**(4), pp. 928–948.
[369] Mosby, M., and Matouš, K., 2015, "Hierarchically Parallel Coupled Finite Strain Multiscale Solver for Modeling Heterogeneous Layers," Int. J. Numer. Methods Eng., **102**(3–4), pp. 748–765.
[370] Šolinc, U., and Korelc, J., 2015, "A Simple Way to Improved Formulation of FE^2 Analysis," Comput. Mech., **56**(5), pp. 905–915.
[371] Matsui, K., Terada, K., and Yuge, K., 2004, "Two-Scale Finite Element Analysis of Heterogeneous Solids With Periodic Microstructures," Comput. Struct., **82**(7–8), pp. 593–606.
[372] Somer, D. D., de Souza Neto, E. A., Dettmer, W. G., and Perić, D., 2009, "A Sub-Stepping Scheme for Multi-Scale Analysis of Solids," Comput. Methods Appl. Mech. Eng., **198**(9–12), pp. 1006–1016.
[373] Abdulle, A., and Bai, Y., 2012, "Reduced Basis Finite Element Heterogeneous Multiscale Method for High-Order Discretizations of Elliptic Homogenization Problems," J. Comput. Phys., **231**(21), pp. 7014–7036.
[374] Yadegari, S., Turteltaub, S., and Suiker, A. S. J., 2015, "Generalized Grain Cluster Method for Multiscale Response of Multiphase Materials," Comput. Mech., **56**(2), pp. 193–219.
[375] Otero, F., Martinez, X., Oller, S., and Salomón, O., 2015, "An Efficient Multi-Scale Method for Non-Linear Analysis of Composite Structures," Compos. Struct., **131**, pp. 707–719.
[376] Zohdi, T. I., Oden, J. T., and Rodin, G. J., 1996, "Hierarchical Modeling of Heterogeneous Bodies," Comput. Methods Appl. Mech. Eng., **138**(1–4), pp. 273–298.
[377] Zohdi, T. I., and Wriggers, P., 1999, "A Domain Decomposition Method for Bodies With Heterogeneous Microstructure Based on Material Regularization," Int. J. Solids Struct., **36**(17), pp. 2507–2525.
[378] Kulkarni, M. G., Matouš, K., and Geubelle, P. H., 2010, "Coupled Multi-Scale Cohesive Modeling of Failure in Heterogeneous Adhesives," Int. J. Numer. Methods Eng., **84**(8), pp. 916–946.
[379] Temizer, İ., and Wriggers, P., 2007, "An Adaptive Method for Homogenization in Orthotropic Nonlinear Elasticity," Comput. Methods Appl. Mech. Eng., **196**(35–36), pp. 3409–3423.
[380] Yvonnet, J., Gonzalez, D., and He, Q.-C., 2009, "Numerically Explicit Potentials for the Homogenization of Nonlinear Elastic Heterogeneous Materials," Comput. Methods Appl. Mech. Eng., **198**(33–36), pp. 2723–2737.
[381] Tran, A. B., Yvonnet, J., He, Q.-C., Toulemonde, C., and Sanahuja, J., 2011, "A Simple Computational Homogenization Method for Structures Made of Linear Heterogeneous Viscoelastic Materials," Comput. Methods Appl. Mech. Eng., **200**(45–46), pp. 2956–2970.
[382] Yvonnet, J., Monteiro, E., and He, Q.-C., 2013, "Computational Homogenization Method and Reduced Database Model for Hyperelastic Heterogeneous Structures," Int. J. Multiscale Comput. Eng., **11**, pp. 201–225.
[383] Le, B. A., Yvonnet, J., and He, Q.-C., 2015, "Computational Homogenization of Nonlinear Elastic Materials Using Neural Networks," Int. J. Numer. Methods Eng., **104**(12), pp. 1061–1084.
[384] Dvorak, G. J., and Benveniste, Y., 1992, "On Transformation Strains and Uniform Fields in Multiphase Elastic Media," Proc. R. Soc. London A, **437**(1900), pp. 291–310.
[385] Michel, J. C., and Suquet, P., 2003, "Nonuniform Transformation Field Analysis," Int. J. Solids Struct., **40**(5), pp. 6937–6955.
[386] Oskay, C., and Fish, J., 2007, "Eigendeformation-Based Reduced Order Homogenization for Failure Analysis of Heterogeneous Materials," Comput. Methods Appl. Mech. Eng., **196**(7), pp. 1216–1243.
[387] Sepe, V., Marfia, S., and Sacco, E., 2013, "A Nonuniform TFA Homogenization Technique Based on Piecewise Interpolation Functions of the Inelastic Field," Int. J. Solids Struct., **50**(5), pp. 725–742.
[388] Fritzen, F., and Leuschner, M., 2013, "Reduced Basis Hybrid Computational Homogenization Based on a Mixed Incremental Formulation," Comput. Methods Appl. Mech. Eng., **260**, pp. 143–154.
[389] Fritzen, F., and Böhlke, T., 2013, "Reduced Basis Homogenization of Viscoelastic Composites," Compos. Sci. Technol., **76**, pp. 84–91.
[390] Fritzen, F., Marfia, S., and Sepe, V., 2015, "Reduced Order Modeling in Nonlinear Homogenization: A Comparative Study," Comput. Struct., **157**, pp. 114–131.
[391] Yvonnet, J., and He, Q.-C., 2007, "The Reduced Model Multiscale Method (R3M) for the Non-Linear Homogenization of Hyperelastic Media at Finite Strains," J. Comput. Phys., **223**(1), pp. 341–368.
[392] Yvonnet, J., Zahrouni, H., and Potier-Ferry, M., 2007, "A Model Reduction Method for the Post-Buckling Analysis of Cellular Microstructures," Comput. Methods Appl. Mech. Eng., **197**(1–4), pp. 265–280.
[393] Chinesta, F., Ammar, A., Lemarchand, F., Beauchene, P., and Boust, F., "Alleviating Mesh Constraints: Model Reduction, Parallel Time Integration and High Resolution Homogenization," Comput. Methods Appl. Mech. Eng., **197**(5), pp. 400–413.
[394] Lamari, H., Ammar, A., Cartraud, P., Legrain, G., Chinesta, F., and Jacquemin, F., 2010, "Routes for Efficient Computational Homogenization of

Nonlinear Materials Using the Proper Generalized Decompositions," Arch. Comput. Methods Eng., **17**(4), pp. 373–391.
[395] Néron, D., and Ladevèze, P., 2010, "Proper Generalized Decomposition for Multiscale and Multiphysics Problems," Arch. Comput. Methods Eng., **17**(4), pp. 351–372.
[396] Ladevèze, P., Passieux, J.-C., and Néron, D., 2010, "The LATIN Multiscale Computational Method and the Proper Generalized Decomposition," Comput. Methods Appl. Mech. Eng., **199**(21–22), pp. 1287–1296.
[397] Hernández, J. A., Oliver, J., Huespe, A. E., Caicedo, M. A., and Cante, J. C., 2014, "High-Performance Model Reduction Techniques in Computational Multiscale Homogenization," Comput. Methods Appl. Mech. Eng., **276**, pp. 149–189.
[398] Francfort, G. A., 1983, "Homogenization and Linear Thermoelasticity," SIAM J. Math. Anal., **14**(4), pp. 696–708.
[399] Turteltaub, S., and Suiker, A. S. J., 2006, "A Multiscale Thermomechanical Model for Cubic to Tetragonal Martensitic Phase Transformations," Int. J. Solids Struct., **43**(14–15), pp. 4509–4545.
[400] Özdemir, I., Brekelmans, W. A. M., and Geers, M. G. D., 2008, "FE^2 Computational Homogenization for the Thermo-Mechanical Analysis of Heterogeneous Solids," Comput. Methods Appl. Mech. Eng., **198**(3–4), pp. 602–613.
[401] Terada, K., Kurumatani, M., Ushida, T., and Kikuchi, N., 2010, "A Method of Two-Scale Thermo-Mechanical Analysis for Porous Solids With Micro-Scale Heat Transfer," Comput. Mech., **46**(2), pp. 269–285.
[402] Temizer, İ., and Wriggers, P., 2011, "Homogenization in Finite Thermoelasticity," J. Mech. Phys. Solids, **59**(2), pp. 344–372.
[403] Mandadapu, K. K., Sengupta, A., and Papadopoulos, P., 2012, "A Homogenization Method for Thermomechanical Continua Using Extensive Physical Quantities," Proc. R. Soc. London A, **468**(2142), pp. 1696–1715.
[404] Sengupta, A., Papadopoulos, P., and Taylor, R. L., 2012, "A Multiscale Finite Element Method for Modeling Fully Coupled Thermomechanical Problems in Solids," Int. J. Numer. Methods Eng., **91**(13), pp. 1386–1405.
[405] Blanco, P. J., and Giusti, S. M., 2014, "Thermomechanical Multiscale Constitutive Modeling: Accounting for Microstructural Thermal Effects," J. Elasticity, **115**(1), pp. 27–46.
[406] Javili, A., Chatzigeorgiou, G., and Steinmann, P., 2013, "Computational Homogenization in Magneto-Mechanics," Int. J. Solids Struct., **50**(25–26), pp. 4197–4216.
[407] Spieler, C., Kästner, M., Goldmann, J., Brummund, J., and Ulbricht, V., 2013, "XFEM Modeling and Homogenization of Magnetoactive Composites," Acta Mech., **224**(11), pp. 2453–2469.
[408] Chatzigeorgiou, G., Javili, A., and Steinmann, P., 2014, "Unified Magnetomechanical Homogenization Framework With Application to Magnetorheological Elastomers," Math. Mech. Solids, **19**(2), pp. 193–211.
[409] Miehe, C., Vallicotti, D., and Teichtmeister, S., 2015, "Homogenization and Multiscale Stability Analysis in Finite Magneto-Electro-Elasticity," GAMM Mitt., **38**(2), pp. 313–343.
[410] Pettermann, H. E., and Suresh, S., 2000, "A Comprehensive Unit Cell Model: A Study of Coupled Effects in Piezoelectric 1-3 Composites," Int. J. Solids Struct., **37**(39), pp. 5447–5464.
[411] Schröder, J., 2009, "Derivation of the Localization and Homogenization Conditions for Electro-Mechanically Coupled Problems," Comput. Mater. Sci., **46**(3), pp. 595–599.
[412] Schröder, J., and Keip, M.-A., 2010, "A Framework for the Two-Scale Homogenization of Electro-Mechanically Coupled Boundary Value Problems," *Computer Methods in Mechanics* (Advanced Structured Materials), Vol. 1, M. Kuczma, and K. Wilmanski, eds., Springer, Berlin, Heidelberg, pp. 311–329.
[413] Zäh, D., and Miehe, C., 2013, "Computational Homogenization in Dissipative Electro-Mechanics of Functional Materials," Comput. Methods Appl. Mech. Eng., **267**, pp. 487–510.
[414] Keip, M.-A., Steinmann, P., and Schröder, J., 2014, "Two-Scale Computational Homogenization of Electro-Elasticity at Finite Strains," Comput. Methods Appl. Mech. Eng., **278**, pp. 62–79.
[415] Miehe, C., Vallicotti, D., and Teichtmeister, S., 2016, "Homogenization and Multiscale Stability Analysis in Finite Magneto-Electro-Elasticity. Application to Soft Matter EE, ME and MEE Composites," Comput. Methods Appl. Mech. Eng., **300**, pp. 294–346.
[416] Chatzigeorgiou, G., Javili, A., and Steinmann, P., 2015, "Interface Properties Influence the Effective Dielectric Constant of Composites," Philos. Mag., **95**(28–30), pp. 3402–3412.
[417] Frey, J., Chambon, R., and Dascalu, C., 2013, "A Two-Scale Poromechanical Model for Cohesive Rocks," Acta Geotech., **8**(2), pp. 107–124.
[418] van den Eijnden, B., Collin, F., Bésuelle, P., and Chambon, R., 2015, "A FE^2 Model for Hydro-Mechanical Coupling," *Bifurcation and Degradation of Geomaterials in the New Millennium* (Springer Series in Geomechanics and Geoengineering), K. T. Chau, and J. Zhao, eds., Springer International Publishing, pp. 53–59.
[419] Terada, K., Ito, T., and Kikuchi, N., 1998, "Characterization of the Mechanical Behaviors of Solid-Fluid Mixture by the Homogenization Method," Comput. Methods Appl. Mech. Eng., **153**(3–4), pp. 223–257.
[420] Sandström, C., Larsson, F., Runesson, K., and Johansson, H., 2013, "A Two-Scale Finite Element Formulation of Stokes Flow in Porous Media," Comput. Methods Appl. Mech. Eng., **261–262**, pp. 96–104.
[421] Lee, K., Moorthy, S., and Ghosh, S., 1999, "Multiple Scale Computational Model for Damage in Composite Materials," Comput. Methods Appl. Mech. Eng., **172**(1–4), pp. 175–201.
[422] Oskay, C., and Fish, J., 2004, "Multiscale Modeling of Fatigue for Ductile Materials," Int. J. Multiscale Comput. Eng., **2**, pp. 1–25.
[423] Fish, J., and Oskay, C., 2005, "A Nonlocal Multiscale Fatigue Model," Mech. Adv. Mater. Struct., **12**(6), pp. 485–500.
[424] Wriggers, P., and Moftah, S. O., 2006, "Mesoscale Models for Concrete: Homogenisation and Damage Behaviour," Finite Elem. Anal. Des., **42**(7), pp. 623–636.
[425] González, C., and Llorca, J., 2006, "Multiscale Modeling of Fracture in Fiber-Reinforced Composites," Acta Mater., **54**(16), pp. 4171–4181.
[426] Guidault, P. A., Allix, O., Champaney, L., and Navarro, J. P., 2007, "A Two-Scale Approach With Homogenization for the Computation of Cracked Structures," Comput. Struct., **85**(17–18), pp. 1360–1371.
[427] Loehnert, S., and Belytschko, T., 2007, "A Multiscale Projection Method for Macro/Microcrack Simulations," Int. J. Numer. Methods Eng., **71**(12), pp. 1466–1482.
[428] Massart, T. J., Peerlings, R. H. J., and Geers, M. G. D., 2007, "An Enhanced Multi-Scale Approach for Masonry Wall Computations With Localization of Damage," Int. J. Numer. Methods Eng., **69**(5), pp. 1022–1059.
[429] Dascalu, C., Bilbie, G., and Agiasofitou, E. K., 2008, "Damage and Size Effects in Elastic Solids: A Homogenization Approach," Int. J. Solids Struct., **45**(2), pp. 409–430.
[430] Belytschko, T., Loehnert, S., and Song, J.-H., 2008, "Multiscale Aggregating Discontinuities: A Method for Circumventing Loss of Material Stability," Int. J. Numer. Methods Eng., **73**(6), pp. 869–894.
[431] Hain, M., and Wriggers, P., 2008, "Computational Homogenization of Micro-Structural Damage Due to Frost in Hardened Cement Paste," Finite Elem. Anal. Des., **44**(5), pp. 233–244.
[432] Song, J.-H., and Belytschko, T., 2009, "Multiscale Aggregating Discontinuities Method for Micro–Macro Failure of Composites," Composites Part B, **40**(6), pp. 417–426.
[433] Souza, F. V., and Allen, D. H., 2010, "Multiscale Modeling of Impact on Heterogeneous Viscoelastic Solids Containing Evolving Microcracks," Int. J. Numer. Methods Eng., **82**, pp. 464–504.
[434] Mergheim, J., 2009, "A Variational Multiscale Method to Model Crack Propagation at Finite Strains," Int. J. Numer. Methods Eng., **80**(3), pp. 269–289.
[435] Verhoosel, C. V., Remmers, J. J. C., Guti, Mérrez, A., and de Borst, R., 2010, "Computational Homogenization for Adhesive and Cohesive Failure in Quasi-Brittle Solids," Int. J. Numer. Methods Eng., **83**(8–9), pp. 1155–1179.
[436] Kaczmarczyk, L., Pearce, C. J., Bićanić, N., and de Souza Neto, E., 2010, "Numerical Multiscale Solution Strategy for Fracturing Heterogeneous Materials," Comput. Methods Appl. Mech. Eng., **199**(17–20), pp. 1100–1113.
[437] Cid Alfaro, M. V., Suiker, A. S. J., Verhoosel, C. V., and de Borst, R., 2010, "Numerical Homogenization of Cracking Processes in Thin Fibre-Epoxy Layers," Eur. J. Mech.—A/Solids, **29**(2), pp. 119–131.
[438] Mercatoris, B. C. N., and Massart, T. J., 2011, "A Coupled Two-Scale Computational Scheme for the Failure of Periodic Quasi-Brittle Thin Planar Shells and Its Application to Masonry," Int. J. Numer. Methods Eng., **85**(9), pp. 1177–1206.
[439] Nguyen, V. P., Lloberas-Valls, O., Stroeven, M., and Sluys, L. J., 2011, "Homogenization-Based Multiscale Crack Modeling: From Micro-Diffusive Damage to Macro-Cracks," Comput. Methods Appl. Mech. Eng., **200**(9–12), pp. 1220–1236.
[440] Unger, J. F., and Eckardt, S., 2011, "Multiscale Modeling of Concrete," Arch. Comput. Methods Eng., **18**, pp. 341–393.
[441] Coenen, E. W. C., Kouznetsova, V. G., Bosco, E., and Geers, M. G. D., 2012, "A Multi-Scale Approach to Bridge Microscale Damage and Macroscale Failure: A Nested Computational Homogenization-Localization Framework," Int. J. Fract., **178**(1), pp. 157–178.
[442] Nguyen, V. P., Stroeven, M., and Sluys, L. J., 2012, "Multiscale Failure Modeling of Concrete: Micromechanical Modeling, Discontinuous Homogenization and Parallel Computations," Comput. Methods Appl. Mech. Eng., **201–204**, pp. 139–156.
[443] Greco, F., Leonetti, L., and Lonetti, P., 2013, "A Two-Scale Failure Analysis of Composite Materials in Presence of Fiber/Matrix Crack Initiation and Propagation," Compos. Struct., **95**, pp. 582–597.
[444] Toro, S., Sánchez, P. J., Huespe, A. E., Giusti, S. M., Blanco, P. J., and Feijóo, R. A., 2014, "A Two-Scale Failure Model for Heterogeneous Materials: Numerical Implementation Based on the Finite Element Method," Int. J. Numer. Methods Eng., **97**(5), pp. 313–351.
[445] Talebi, H., Silani, M., Bordas, S. P. A., Kerfriden, P., and Rabczuk, T., 2014, "A Computational Library for Multiscale Modeling of Material Failure," Comput. Mech., **53**(5), pp. 1047–1071.
[446] Bosco, E., Kouznetsova, V. G., and Geers, M. G. D., 2015, "Multi-Scale Computational Homogenization-Localization for Propagating Discontinuities Using X-FEM," Int. J. Numer. Methods Eng., **102**(3–4), pp. 496–527.
[447] Geymonat, G., Müller, S., and Triantafyllidis, N., 1993, "Homogenization of Nonlinearly Elastic Materials, Microscopic Bifurcation and Macroscopic Loss of Rank-One Convexity," Arch. Ration. Mech. Anal., **122**(3), pp. 231–290.
[448] Miehe, C., Schröder, J., and Becker, M., 2002, "Computational Homogenization Analysis in Finite Elasticity: Material and Structural Instabilities on the Micro- and Macro-Scales of Periodic Composites and Their Interaction," Comput. Methods Appl. Mech. Eng., **191**(44), pp. 4971–5005.
[449] Triantafyllidis, N., Nestorović, M. D., and Schraad, M. W., 2005, "Failure Surfaces for Finitely Strained Two-Phase Periodic Solids Under General In-Plane Loading," ASME J. Appl. Mech., **73**(3), pp. 505–515.

[450] Michel, J. C., Lopez-Pamies, O., Ponte Castañeda, P., and Triantafyllidis, N., 2007, "Microscopic and Macroscopic Instabilities in Finitely Strained Porous Elastomers," J. Mech. Phys. Solids, **55**(5), pp. 900–938.
[451] Nezamabadi, S., Yvonnet, J., Zahrouni, H., and Potier-Ferry, M., 2009, "A Multilevel Computational Strategy for Handling Microscopic and Macroscopic Instabilities," Comput. Methods Appl. Mech. Eng., **198**(27–29), pp. 2099–2110.
[452] Martinez, X., and Oller, S., 2009,"Numerical Simulation of Matrix Reinforced Composite Materials Subjected to Compression Loads," Arch. Comput. Methods Eng., **16**, pp. 357–397.
[453] Belytschko, T., and Song, J.-H., 2010, "Coarse-Graining of Multiscale Crack Propagation," Int. J. Numer. Methods Eng., **81**, pp. 537–563.
[454] Nguyen, V.-D., and Noels, L., 2014, "Computational Homogenization of Cellular Materials," Int. J. Solids Struct., **51**(11–12), pp. 2183–2203.
[455] Fritzen, F., and Kochmann, D. M., 2014, "Material Instability-Induced Extreme Damping in Composites: A Computational Study," Int. J. Solids Struct., **51**(23–24), pp. 4101–4112.
[456] Cong, Y., Nezamabadi, S., Zahrouni, H., and Yvonnet, J., 2015, "Multiscale Computational Homogenization of Heterogeneous Shells at Small Strains With Extensions to Finite Displacements and Buckling," Int. J. Numer. Methods Eng., **104**(4), pp. 235–259.
[457] Swan, C. C., 1994, "Techniques for Stress- and Strain-Controlled Homogenization of Inelastic Periodic Composites," Comput. Methods Appl. Mech. Eng., **117**(3–4), pp. 249–267.
[458] Temizer, İ., and Wriggers, P., 2008, "On a Mass Conservation Criterion in Micro-To-Macro Transitions," ASME J. Appl. Mech., **75**(5), p. 054503.
[459] Grytz, R., and Meschke, G., 2008, "Consistent Micro–Macro Transitions at Large Objective Strains in Curvilinear Convective Coordinates," Int. J. Numer. Methods Eng., **73**(6), pp. 805–824.
[460] van Dijk, N. P., 2016, "Formulation and Implementation of Stress-Driven and/or Strain-Driven Computational Homogenization for Finite Strain," Int. J. Numer. Methods Eng., **107**(12), pp. 1009–1028.
[461] Pindera, M.-J., Khatam, H., Drago, A. S., and Yogesh, B., 2009, "Micromechanics of Spatially Uniform Heterogeneous Media: A Critical Review and Emerging Approaches," Composites Part B, **40**(5), pp. 349–378.
[462] Miehe, C., 2003, "Computational Micro-To-Macro Transitions for Discretized Micro-Structures of Heterogeneous Materials at Finite Strains Based on the Minimization of Averaged Incremental Energy," Comput. Methods Appl. Mech. Eng., **192**(5–6), pp. 559–591.
[463] Temizer, İ., and Wriggers, P., 2008, "On the Computation of the Macroscopic Tangent for Multiscale Volumetric Homogenization Problems," Comput. Methods Appl. Mech. Eng., **198**(3–4), pp. 495–510.
[464] Yuan, Z., and Fish, J., 2008, "Toward Realization of Computational Homogenization in Practice," Int. J. Numer. Methods Eng., **73**(3), pp. 361–380.
[465] Nguyen, V.-D., Béchet, E., Geuzaine, C., and Noels, L., 2012, "Imposing Periodic Boundary Condition on Arbitrary Meshes by Polynomial Interpolation," Comput. Mater. Sci., **55**, pp. 390–406.
[466] Felippa, C. A., and Park, K. C., 2002, "The Construction of Free-Free Flexibility Matrices for Multilevel Structural Analysis," Comput. Methods Appl. Mech. Eng., **191**(19–20), pp. 2139–2168.
[467] Fish, J., and Fan, R., 2008, "Mathematical Homogenization of Nonperiodic Heterogeneous Media Subjected to Large Deformation Transient Loading," Int. J. Numer. Methods Eng., **76**(7), pp. 1044–1064.
[468] Wang, Z. M., Kwan, A. K. H., and Chan, H. C., 1999, "Mesoscopic Study of Concrete I: Generation of Random Aggregate Structure and Finite Element Mesh," Comput. Struct., **70**(5), pp. 533–544.
[469] Torquato, S., 2002, *Random Heterogeneous Materials: Microstructure and Macroscopic Properties*, Springer-Verlag, New York.
[470] Böhm, H. J., Eckschlager, A., and Han, W., 2002, "Multi-Inclusion Unit Cell Models for Metal Matrix Composites With Randomly Oriented Discontinuous Reinforcements," Comput. Mater. Sci., **25**(1–2), pp. 42–53.
[471] Cailletaud, G., Forest, S., Jeulin, D., Feyel, F., Galliet, I., Mounoury, V., and Quilici, S., 2003, "Some Elements of Microstructural Mechanics," Comput. Mater. Sci., **27**(3), pp. 351–374.
[472] Mishnaevsky, L. L., Jr., 2004, "Three-Dimensional Numerical Testing of Microstructures of Particle Reinforced Composites," Acta Mater., **52**(14), pp. 4177–4188.
[473] Häfner, S., Eckardt, S., Luther, T., and Könke, C., 2006, "Mesoscale Modeling of Concrete: Geometry and Numerics," Comput. Struct., **84**(7), pp. 450–461.
[474] Musienko, A., Tatschl, A., Schmidegg, K., Kolednik, O., Pippan, R., and Cailletaud, G., 2007, "Three-Dimensional Finite Element Simulation of a Polycrystalline Copper Specimen," Acta Mater., **55**(12), pp. 4121–4136.
[475] Galli, M., Botsis, J., and Janczak-Rusch, J., 2008, "An Elastoplastic Three-Dimensional Homogenization Model for Particle Reinforced Composites," Comput. Mater. Sci., **41**(3), pp. 312–321.
[476] Lee, K. M., and Park, J. H., 2008, "A Numerical Model for Elastic Modulus of Concrete Considering Interfacial Transition Zone," Cem. Concr. Res., **38**(3), pp. 396–402.
[477] Reid, A. C. E., Langer, S. A., Lua, R. C., Coffman, V. R., Haan, S., and García, R. E., 2008, "Image-Based Finite Element Mesh Construction for Material Microstructures," Comput. Mater. Sci., **43**(4), pp. 989–999.
[478] Yu, Y., Cui, J., and Han, F., 2008, "An Effective Computer Generation Method for the Composites With Random Distribution of Large Numbers of Heterogeneous Grains," Compos. Sci. Technol., **68**(12), pp. 2543–2550.
[479] He, H., 2010, "Computational Modelling of Particle Packing in Concrete," Ph.D. thesis, TU Delft, Delft University of Technology, Delft, Netherlands.
[480] Fritzen, F., 2011, "Microstructural Modeling and Computational Homogenization of the Physically Linear and Nonlinear Constitutive Behavior of Micro-Heterogeneous Materials," Ph.D. thesis, Karlsruher Institut für Technologie, Karlsruhe, Germany.
[481] Sonon, B., Francois, B., and Massart, T. J., 2012, "A Unified Level Set Based Methodology for Fast Generation of Complex Microstructural Multi-Phase RVEs," Comput. Methods Appl. Mech. Eng., **223–224**, pp. 103–122.
[482] Öhman, M., Larsson, F., and Runesson, K., 2013, "Computational Homogenization of Liquid-Phase Sintering With Seamless Transition From Macroscopic Compressibility to Incompressibility," Comput. Methods Appl. Mech. Eng., **266**, pp. 219–228.